공학박사 학위논문

Stress and Strain Analysis of Thin Film Interconnects in Next-Generation Electronic Devices Using Finite Element Method

유한요소해석법을 이용한 차세대 전자 소자용 박막 배선 재료의 응력 및 변형 분석에 관한 연구

2023년 2월

서울대학교 대학원

재료공학부

이 종 성

유한요소해석법을 이용한 차세대 전자 소자용 박막 배선 재료의 응력 및 변형 분석에 관한 연구

STRESS AND STRAIN ANALYSIS OF THIN FILM INTERCONNECTS IN NEXT-GENERATION ELECTRONIC DEVICES USING FINITE ELEMENT METHOD

지도 교수: 최 인 석, 이 명 규

이 논문을 공학박사 학위논문으로 제출함

2023년 2월

서울대학교 대학원

재료공학부

이 종 성

이 종 성의 공학박사 학위논문을 인준함

2023년 1월

위 원 장 _____ 유 웅 렬 _____ (인)

부위원장 _____ 최 인 석 _____ (인)

위 원 _____ 이 명 규 _____ (인)

위 원 _____ 김 병 준 _____ (인)

위 원 _____ 김 선 철 _____ (인)

ABSTRACT

Stress and Strain Analysis of Thin Film Interconnects in Next-Generation Electronic Devices Using Finite Element Method

Jong-Sung Lee

Department of Materials Science and Engineering

The Graduate School

Seoul National University

Along with the fourth industrial revolution, the importance of electronic devices that process digital information have been increased. As electronic devices have been developed, innovative technologies for miniaturization and diversification of interconnects are emerging rapidly. Miniaturization of interconnects for connecting sub-10 nm transistors, and diversification of interconnects which can be mechanically deformed for wearable, are progressed. However, with the recent development of interconnects, many problems have arisen due to mechanical stress and strain generated in thin films such as high residual stress generated during deposition, increased interfaces between heterogeneous materials, and human body motions.

In this thesis, the stress and strain problems occurring in thin film interconnects are predicted and solved by using finite element analysis. To solve the mechanical

problems of thin film interconnects in which stress and strain occur combined, the analysis was conducted for two stress-dominant and strain-dominant cases.

For the stress-dominant cases of thin film interconnects, a stress prediction model for tungsten thin film based on a thin film growth model was proposed. Tungsten has been commonly used for fine interconnects due to its good gap-filling characteristics in 3D molds, such as trench patterns. However, tungsten shows high deposition stress. To reduce tungsten's deposition stress, the shape of the nuclei can be controlled, which is an effective way to suppress the mechanical deformation caused by the formation of a grain boundary between free surfaces during the coalescence stage. As a result, the wider the elliptical nucleus was, the lower the film stress, and mold bending between line patterns was also reduced.

For the strain-dominant cases of thin film interconnects, a stress-free zone in the twisting of flexible electronics was founded by strain analysis. The stress-free zone such as the neutral plane of bending has been widely investigated. However, unlike bending deformation, few studies have been conducted on twisting deformations such as wrist and neck rotation of the human body. To develop highly reliable twisting electronics, two twisting modes, fixed and free twisting, were proposed, which are determined by the boundary condition of the surface. For fixed twisting, the patterns at the center show higher stability, but for free twisting, the patterns at the edge exhibit superior mechanical reliability.

As the thin film interconnects span a nanometer scale and visible scale, mechanical problems occur as stress and strain combined phenomena. To solve these combined problems, simulation models and solutions were presented by different simplified approaches to each case where stress and strain were dominant using the

finite element method. Each approach in two cases, the stress in metal and the strain in flexible interconnects, can provide guidelines for combined mechanical issues for reliable thin film interconnects in future electronic devices.

Keywords: Interconnects, Packaging, Stress, Strain, Finite element method, Flexible electronics

Student Number: 2017-27024

Table of Contents

Chapter 3. Stress Analysis of Tungsten Film and Interconnects Due to Coalescence in Trench Mold

Chapter 4. Strain Analysis of Twisting Modes in Wearable Devices

Chapter 5. Conclusion and Future Work

LIST OF TABLES

LIST OF FIGURES

Figure 3.2 Limits of copper interconnects. (a) Schematic of reduced cross-sectional area due to barrier layer. (b) Electrical resistance depending on the thickness of film, copper with TaN barrier system shows a high increase in electrical resistance under 10 nm.

Figure 3.3 Refractory metal for barrier-less interconnects. (a) Activation energy of self-diffusion depending on melting point of metals. Atomic migration is inversely proportional the melting points. (b) Schematic of barrier-less interconnects.

Figure 3.4 (a) Schematic of the stress evolution stage in the trench filling process that forms a line pattern with a high aspect ratio. Intergranular coalescence occurs only in the sidewall of the mold, and interfilm coalescence is caused by interaction between the free surfaces of both films. (b) Schematic of cross-sectional illustration of mold bending due to film stress on the trench mold, which vertically separates the line pattern. (c) Schematic plot of mold bending caused by coalescence versus thickness.

Figure 3.5 Schematic of the coalescence stress depending on nuclei shape. The wide elliptical shape is less zipped, resulting in lower coalescence stress.

Figure 3.6 (a) Schematic of the model used to calculate film stress in intergranular coalescence caused by contact between metal nuclei, depending on the ratio of width-to-height (r/t_i) of nuclei. (b) Schematic of the trench mold used to calculate mold bending due to interfilm coalescence during the trench filling process.

Figure 3.7 (a) The flow chart of the simulation procedure of intergranular coalescence (blue box) and interfilm coalescence (red box), respectively. (b) Schematic image of the simulation model of intergranular coalescence between tungsten islands during film growth and (c) the simulation model for interfilm coalescence occurring in the center of the trench mold to form a line pattern. Both models were deformed by surface traction to calculate film stress and mold bending.

Figure 3.8 The lowest state calculation by the sum of increased strain energy and decreased zipping energy.

Figure 3.9 Strain energy (red) and zipping energy (blue) depending on the nucleus shape of the initial intergranular coalescence, and the lowest state of the total energy. When the value of r/t_i ratio is 5, negative energy state of total energy was not calculated.

Figure 3.10 FEM simulation results of the intergranular coalescence stage. (a) Normalized zipping distance (z_0) and (b) normalized average stress when zipping occurs at the initial contact between nuclei depending on the r/t_i of the nuclei

Figure 3.11 FEM simulation results of normalized average stress depending on r/t_i during film growth after contact between nuclei.

Figure 3.12 Finite element simulation result of stress evolution during growth after forming a continuous film. The graphs in the figure represent the stresses for different r/t_i values, where the initial nuclei have r/t_i values of 1.5 (black), 2 (red), and 4 (blue).

Figure 3.13 Simulation results for mold bending by the pattern defects of two cases, the results of the mold bending of an Si mold due to film stress and interfilm coalescence. An asymmetric structure was used to calculate mold bending due to patterning error or other defects: (a) 10 nm depth difference and (b) 1.5 nm width difference.

Figure 3.14 Simulation results for mold bending with the pattern defects of both 10 nm depth difference and 1.5 nm width difference.

Figure 3.15 The graph of Cross-sectional area change in interconnects inside the trench according to mold bending: Symmetric is the case of no pattern defect, and asymmetric is when both 10 nm depth difference and 1.5 nm width difference exist.

Figure 3.16 FEM simulation results of initial zipping depending on the r/t_i of the tungsten (black), molybdenum (blue), and ruthenium (red) nuclei: (a) normalized zipping distance and (b) normalized average stress.

CHAPTER 1

Introduction

1.1 Development trend of future electronic devices

As the importance of the internet of things (IoT) and digital data processing technologies increases with the fourth industrial revolution, the necessity of innovative performance improvements and diversification of functionality in electronic devices is emerging [1-3]. Since the pandemic caused by the coronavirus that spread around the world began in 2019, the importance of online networking and coworking has emerged, and digital transformation has occurred in the virtual universe constructed in the digital space, recently called the 'metaverse'. As shown in Fig. 1.1, the market and demand for electronic technology has also significantly increased in terms of both hardware and software to process the enormous digital data traffic [4-6].

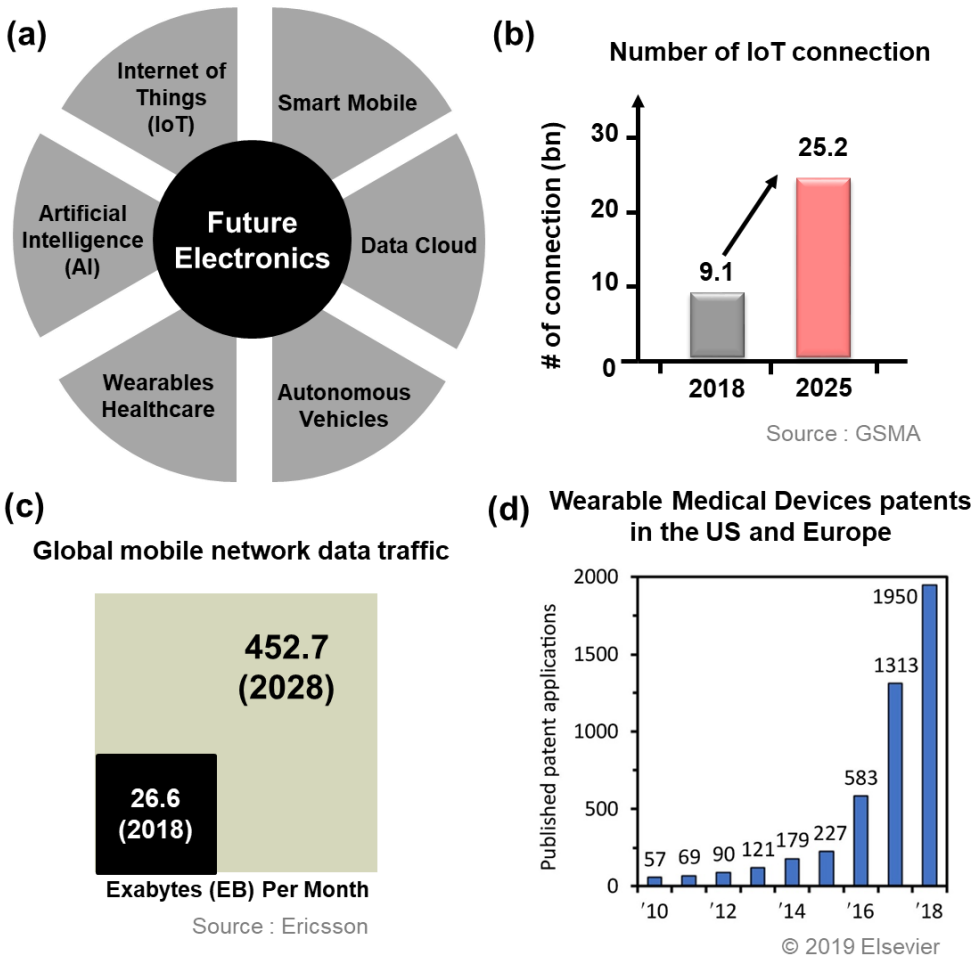

Figure 1.1 Emerging electronic devices and digital data market. (a) Future application of electronics undergirded by digital transformation. (b) Forecast of the potential IoT connections in 2025. (c) Trend of global data traffic growth in mobile applications by 2028. (d) Published patents of wearable medical devices by year in the US and European patent offices [2-5].

From the point of view of the hardware industry, the development of electronic devices is proceeding in two directions: miniaturization and diversification. Miniaturization means that each independent element is shrunk and occupies a smaller space to improve the integrity and performance. As shown in Fig. 1.2, shrinkage of the node size according to Moore's Law is in progress. To compute, process, store, and exchange large amounts of information, the development of integration technologies is essential for faster response and higher efficiency [7-11]. Typically, the technology node as an index of the degree of integration and miniaturization means the gate length of a field-effect transistor (FET) or the half pitch of the metal or the gate. The shrinkage of the node size improves the performance of transistors and electronic devices for the following reasons. First, the operation efficiency is improved with the lower source-gate voltage in short channels. Second, the operation time becomes faster due to a reduction in the signal transmission distance. Lastly, more transistors and memory can be integrated on a wafer [12].

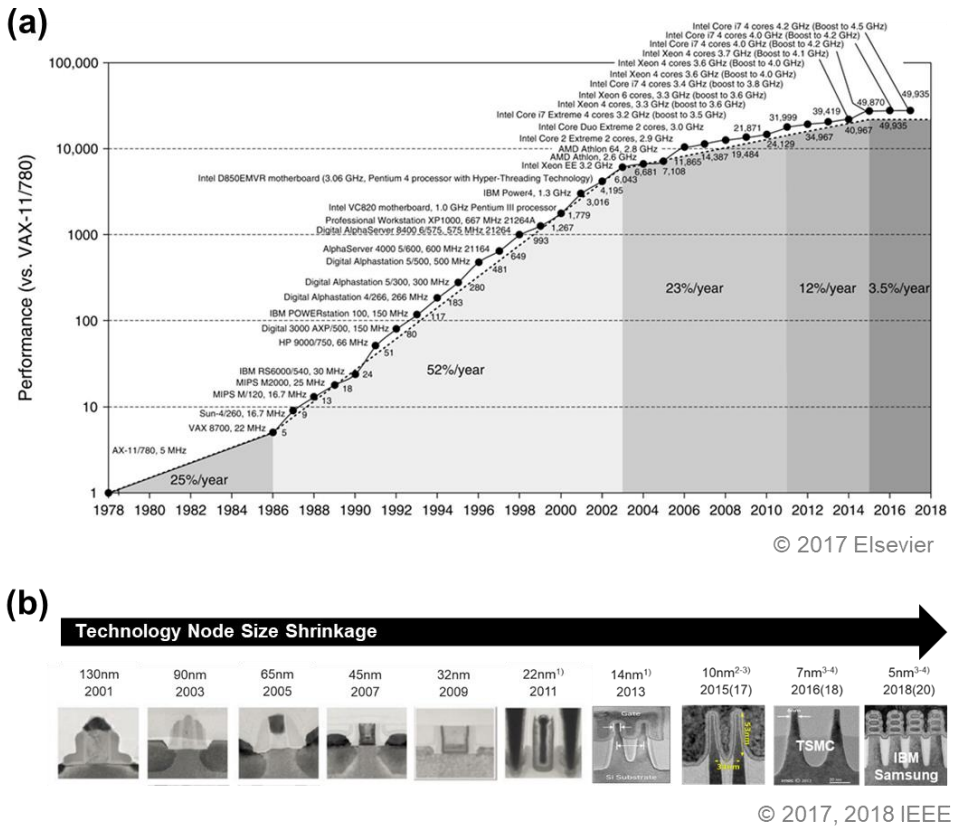

Figure 1.2 (a) Technology development that followed the trend of Moore's Law scaling and plateauing of the computing performance. (b) Cross-sectional image of a transistor according to shrinkage of the technology node size [7-11].

Diversification means the expansion of the form factor to pioneer new applications of electronic devices, as shown in Fig. 1.3. To improve the adaptability of electronics to human life, such as wearables, hardware development is being conducted to realize flexible, stretchable, and conformable device types that deviate from the conventional electronics with rigid packaging. The mechanical deformability of a device platform accelerates the expansion of the electronic application range on the human surface. The wearability and adhesion of electronic devices are improved, and a stable interface between the body and the sensors is maintained to measure various human body signals, such as temperature, strain, and heart rate. Various unit devices, such as biosensors, motion trackers, and haptic feedback devices, are integrated into thin and stretchable platforms, such as rubbery polymers, to be more closely connected to humans, who have soft and curved surfaces for which access by rigid devices is restricted [13], [14].

Recent electronics technology shows a very large gap in the performance and function compared to the devices of 10 years ago that seemed impossible to overcome, in which the technology of transistors with a several nanometer node size was developed that was considered impossible to commercialize. Commercial processors and memories with an enormous number of these transistors are producing very large amounts of data every minute, making human life more prosperous. The development of the performance and functionality of these electronic devices is very important to change the paradigm of modern society to a hyperconnected society [15].

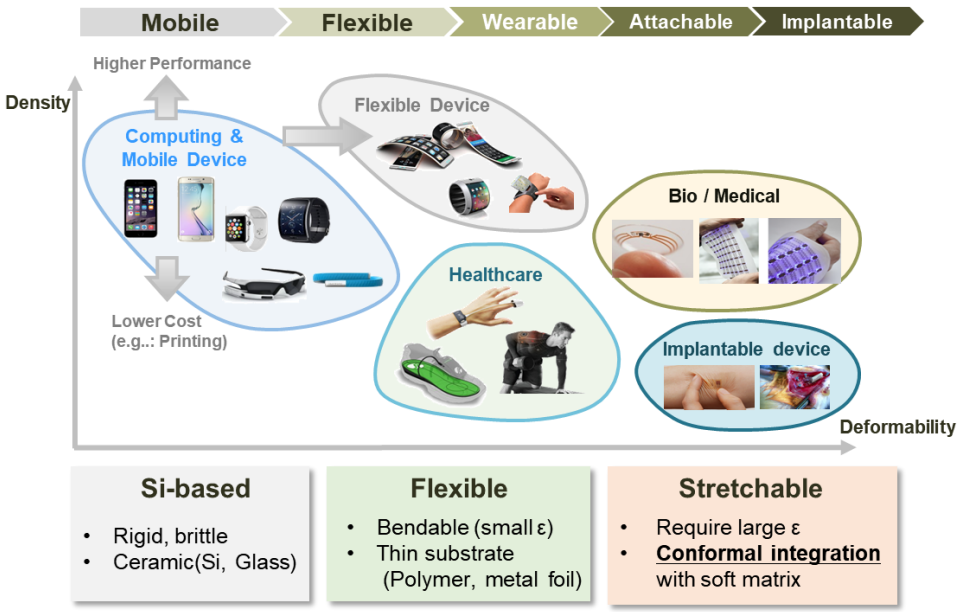

Figure 1.3 Diversification of electronic devices: From rigid devices to flexible and stretchable platforms with deformable form factors [13], [14].

1.2 Interconnects: Connecting the nanoscale and macroscale

With the development of electronic devices, the importance of interconnects that electrically connect each electronic element is also increasing. Interconnection systems range from transistors of a several nanometers scale to products of visible scale. As shown in Fig. 1.4, interconnects at the M0 and M1 levels connect each electrical part of a transistor with a scale of several nanometers [16], [17], and interconnects at the package level connect the bumps or wires of a chip to the board with a scale of several micrometers [18]. Furthermore, electronic units such as various batteries, sensors, and controllers are connected to processors to supply digital signals and electrical power in the 2D printed circuit board (PCB) by several millimeter-scale interconnects [19]. As more elements are integrated, more interconnections are required, and the scale window of interconnects, such as the width and pitch, is very wide, unlike other individual electronic elements.

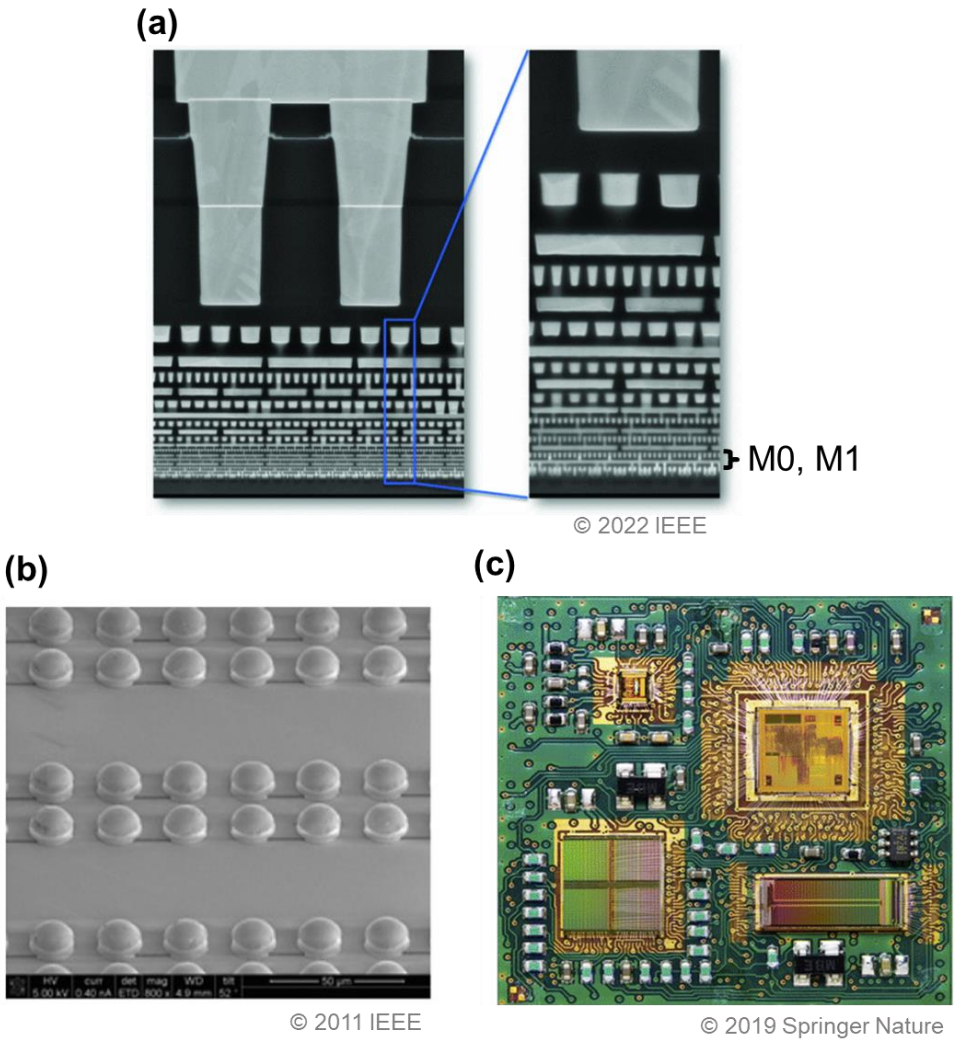

Figure 1.4 Interconnection systems in electronic devices depending on the scale window. (a) Metal interconnect (Mx) layer for local interconnects. (b) Solder microbumps for chip and board interconnection. (c) Chip and passive component integration in a PCB for device operation [17-19].

These interconnects must meet various performance metrics depending on the scale window, but the most important performance metric is good signal transmission. The performance of interconnects is commonly evaluated by the RC delay, where R is the electrical resistance of interconnects and C is the capacitance of the dielectric and insulator. With the miniaturization of electronic elements, the cross-section and pitch of interconnects are decreased, and then, the electrical resistance and capacitance of the interconnection system increase, as shown in Fig. 1.5, which interrupts the electric current [20]. The von Neumann bottleneck means that the process of exchanging information between the processor and memory is the determining step of the operation speed [21]. Electrical signal delay in interconnects is a critical issue in the high-speed operation of electronic devices. Therefore, the direction of interconnection technology is to lower the electrical resistance.

Therefore, the recent developments in interconnects are focused on heterogeneous integration, which can achieve the shortest distance through a vertical interconnection system and selective high bandwidth interconnection. For example, an interposer and a bridge for an electrical shortcut between the CPU and memory [22], high bandwidth memory (HBM) connected vertically by through silicon vias (TSVs) [23], and a redistribution layer (RDL) for expansion of the bonding area between the chip and board [24] have been developed, as shown in Fig. 1.6. Most conductors are metallic materials such as copper, which have the advantages of excellent conductivity and processability.

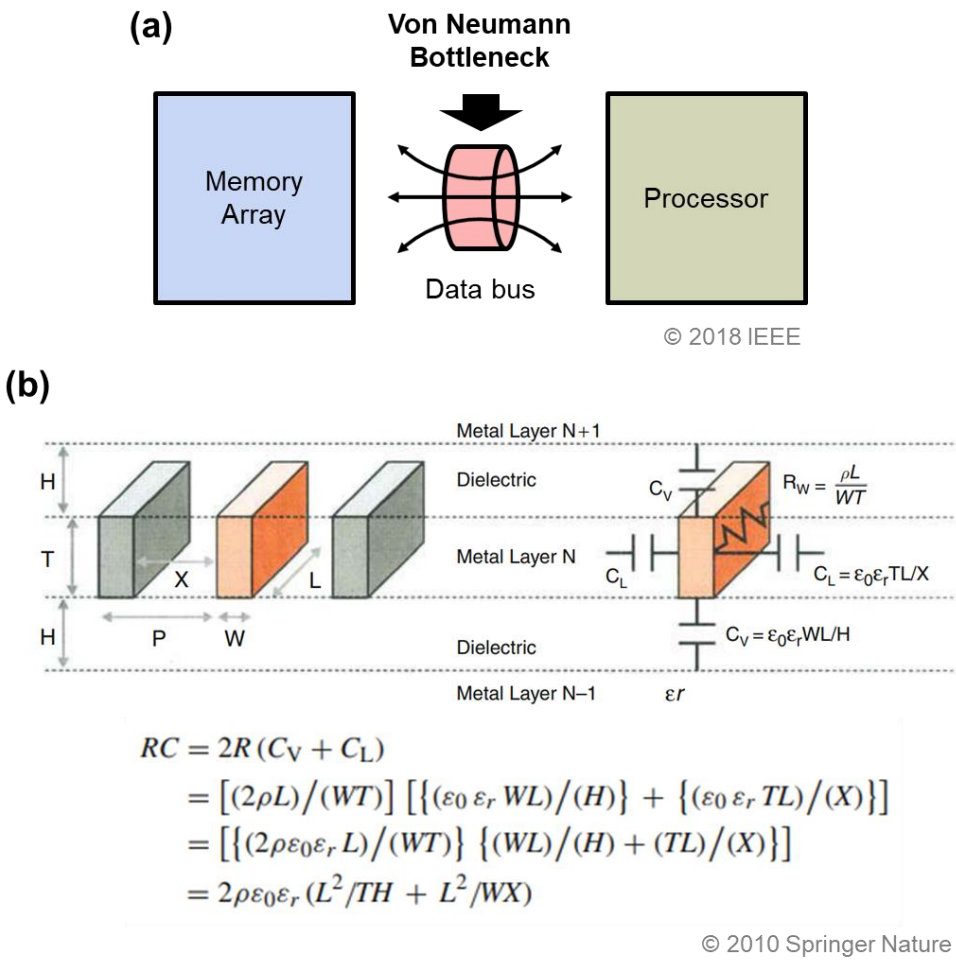

Figure 1.5 Performance evaluation of interconnects. (a) Schematic of the von Neumann bottleneck, which is the determining step of the computing speed due to the speed limit of the data bus. (b) Schematic of the electrical components in interconnects. The electrical resistance of interconnects R and the capacitance C are configured by the insulators around the interconnects [20], [21].

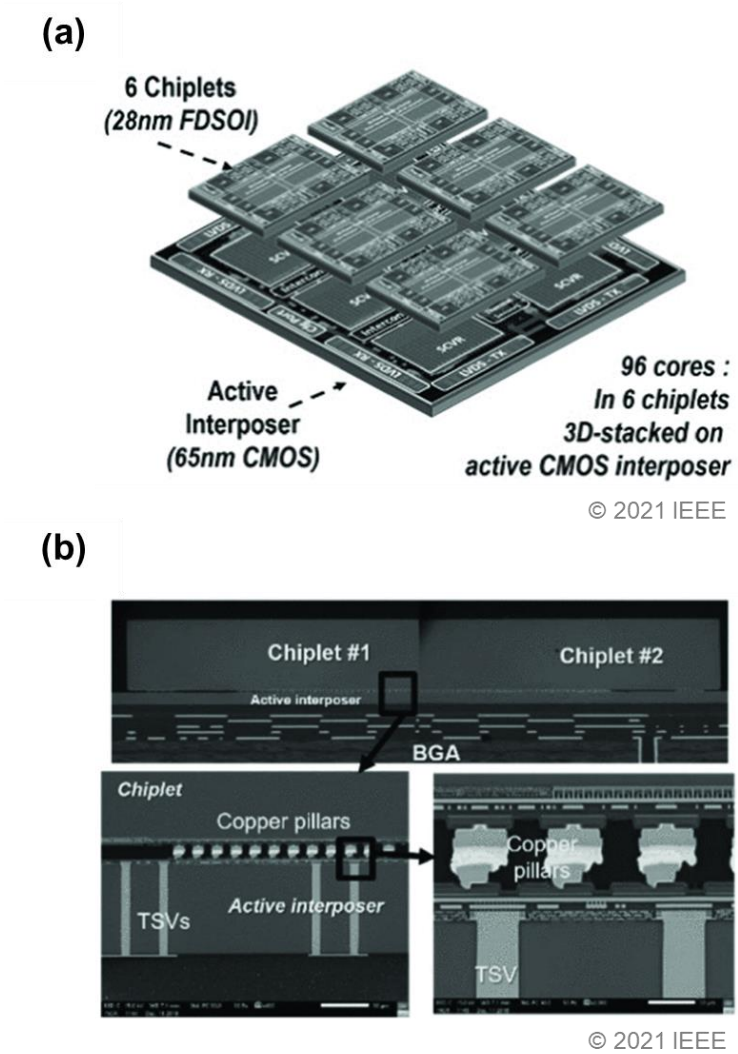

Figure 1.6 Trends of recent interconnect technologies for effective interconnection with the shortest vertical path and selective integration such as heterogeneous integration: (a) Schematic of chiplet integration by an interposer, and (b) cross-sectional SEM image [22].

In a different direction from the manufacturing industry, deformable interconnection platforms for wearable devices are being developed from soft materials and deformable structures. Electronic elements such as transistors are very small, so they are not affected by mechanical deformation occurring at the macroscale, or they are isolated from stress on stiff islands. However, interconnects should be deformable while remaining conductive.

The soft materials are inherently deformable conductors such as metallic nanowires and conductive gels based on conductive materials [25], [26]. In the case of the structural form, a curved structure such as a serpentine pattern for in-plane bending, an out-of-plane pattern such as buckling obtained by releasing a prestretched substrate, or a perforated pattern such as a kirigami structure that employs out-of-plane bending deformation is utilized, which delocalizes stress and achieves the same displacement with less deformation of the material itself [27], [28]. In addition, in the case of a specific motion such as bending and twisting deformation, the neutral axis where the stress is zero is investigated to place the elements vulnerable to deformation. Many studies have proposed controlling the stress and strain of conductors through various structures to make interconnects robust.

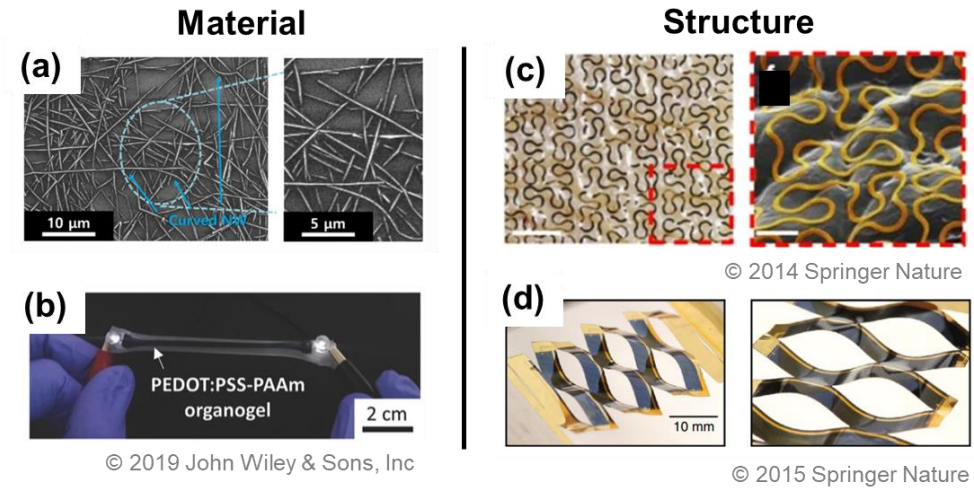

Figure 1.7 Soft interconnection platform: Material and structural perspective. (a) Silver nanowires embedded in a stretchable resin. (b) PEDOT:PSS conductive organogel. (c) Serpentine-patterned gold interconnects on skin. (d) Kirigami-inspired solar cell [25-28].

1.3 Emerging mechanical problems in interconnects

Recently, the importance of mechanical issues of interconnects has emerged with node shrinkage. Previous research on and development of interconnects was aimed more at the electrical properties. Due to the advantages in terms of the electrical properties, improvement of the performance of electronic device through shrinkage of the node size has been regarded as an immutable truth. However, mechanical problems that have not appeared in the past have arisen with scaling down to sizes of a few nanometers with atomic-scale spacing [16]. Differences in the mechanical properties between bulk metals and thin films, especially in the process of film deposition, with increasing interface and decreasing mechanical stiffness and dimensional margin of the process, make interconnects vulnerable to mechanical failure. Stress-induced failure, such as atomic migration and pattern distortion, occurs due to residual stress in the metal film, as shown in Fig. 1.8 [29], [30].

Another issue is mechanical distortion of the system, such as warpage due to the difference in the thermal expansion coefficients. As the number of process steps increases, mechanical stress accumulates due to thermal cycling during multilayer deposition and causes curvature of the wafer or substrate [31]. Furthermore, mechanical issues are expanding with the use of deformable platforms that are exposed to repeated mechanical deformation, such as folding for multiple forms of use, compared to the devices that passively resist deformation [32].

YEAR OF PRODUCTION	2021	2022	2025	2028	2031	2034
	G51M30	G48M24	G45M20	G42M16	G40M16/T2	G38M16/T4
Logic industry "Node Range" Labeling (nm)	"5"	"3"	"2.1"	"1.5"	"1.0 eq"	"0.7 eq"
IDM-Foundry node labeling	i7-f5	i5-f3	i3-f2.1	i2.1-f1.5	i1.5e-f1.0e	i1.0e-f0.7e
Logic device structure options	FinFET	finFET LGAA	LGAA	LGAA	LGAA-3D	LGAA-3D
Platform device for logic	finFET	finFET	LGAA	LGAA	LGAA-3D	LGAA-3D
	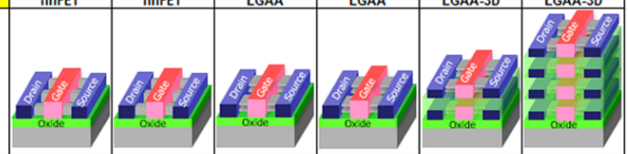					
LOGIC DEVICE GROUND RULES						
Mx pitch (nm)	36	32	24	20	16	16
M1 pitch (nm)	34	32	23	21	20	19
M0 pitch (nm)	30	24	20	16	16	16
Gate pitch (nm)	51	48	45	42	40	38
Lg: Gate Length - HP (nm)	18	16	14	12	12	12
Lg: Gate Length - HD (nm)	20	18	14	12	12	12
Channel overlap ratio - two-sided	0.20	0.20	0.20	0.20	0.20	0.20
Spacer width (nm)	7	6	5	4	4	4
Contact CD (nm) - finFET, LGAA	19	20	21	22	20	18
Contact CD (nm) - VGAA						
Device architecture key ground rules						
FinFET pitch (nm)	28.0	24.0				
FinFET Fin width (nm)	6.0	5.0				
FinFET Fin height (nm)	50	64				
Footprint drive efficiency - finFET	3.79	5.54				
Lateral GAA lateral pitch (nm)			22.0	20.0	20.0	20.0
Lateral GAA vertical pitch (nm)			18.0	16.0	14.0	14.0
Lateral GAA (nanosheet) thickness (nm)			7.0	6.0	5.0	5.0
Number of vertically stacked nanosheets			3	3	4	4
LGAA width (nm) - HP			30	25	20	15
LGAA width (nm) - HD			15	11	6	6
LGAA width (nm) - SRAM			7	6	6	6
LGAA total height (nm)			53	48	57	57
Footprint drive efficiency - lateral GAA - HP			4.93	4.77	5.88	5.52
Device effective width (nm) - HP	106.0	133.0	222.0	186.0	200.0	160.0
Device effective width (nm) - HD	106.0	133.0	132.0	102.0	88.0	88.0
Device lateral pitch (nm)	28	24	22	20	20	20
Device height (nm)	50.0	64.0	53.0	48.0	57.0	57.0
Device width (nm) - HP	6	5	30	25	20	15
Device width (nm) - HD	6	5	15	11	6	6
Device width (nm) - SRAM	6	5	7	6	6	6

Table 1.1 Forecast of the ground rules for miniaturization of logic devices such as the metal interconnect (M0, M1, and Mx) pitch [16].

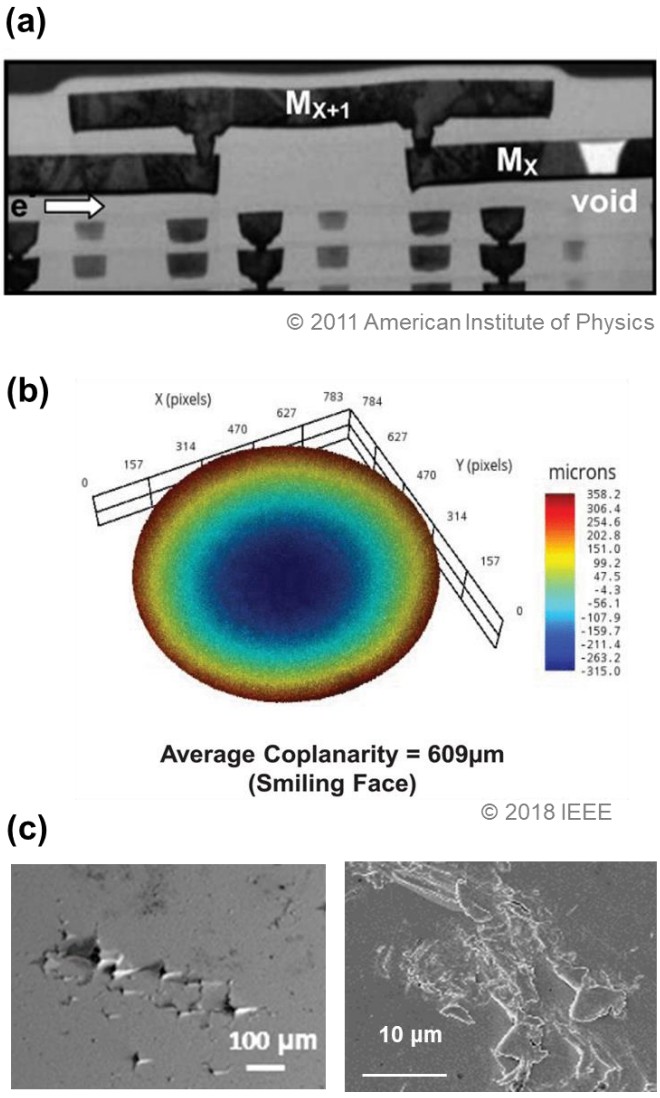

Figure 1.8 Stress-induced failure depending on the scale window: (a) atomic migration, (b) warpage of the wafer, and (c) fracture and delamination as well as fatigue of the copper film [29], [31].

In summary, in the case of fine interconnects close to the front-end-of-line (FEOL), film stress affecting the film quality is important, and in the case of interconnects in the back-end-of-line (BEOL) and packaging, mechanical deformation on the visible scale is important due to the accumulation of stress and mechanical motion. Therefore, the mechanical problem of interconnects requires a comprehensive understanding of the stress occurring in the microscopic area and the strain that systematically occurs in the macroscopic area to solve the mechanical problems.

1.4 Thesis objectives

The main objective of this thesis is to contribute to solving the mechanical problems of thin film interconnects from the perspectives of both stress in nanometer-thick metal films and strain during flexible motion on a visible scale. Both the stress-dominant case and strain-dominant case were calculated by a numerical finite element method (FEM) solver to predict mechanical deformation. For modeling the stress-dominant case of thin film interconnects, a new stress calculation model of tungsten was proposed, which is a refractory metal that is immobile at the operation temperature and a candidate to replace copper, which requires a barrier. Additionally, the stress generation stage due to the film interaction in a vertical structure such as a trench mold was modeled. Mold bending, which affects the interconnect pattern due to an increase in the interface per volume and a decrease in the mechanical stiffness, was calculated. Furthermore, to predict the strain-dominant case of thin film interconnects, the strain distribution in twisting deformation that occurs when boundary conditions change depending on the surface the device is attached to such as the human body was analyzed. A new perspective on the strain distribution in twisting motion was presented and proven by thin film interconnects on a flexible substrate. In summary, this thesis provides inspiration and intuition to solve the mechanical problem of thin film interconnects in which stress and strain are mixed from the microscale to macroscale.

1.5 Organization of the thesis

This thesis consists of a total of 5 chapters, including the introduction of the thesis. In chapter 2, the theoretical background of thin film technologies and mechanics required for modeling mechanical issues is explained. In chapter 3, a new stress calculation model is proposed based on the film growth mechanisms of tungsten, and the film stress during the deposition process is calculated. The bending of the vertical mold due to the film stress evolution and film interaction is also calculated. In chapter 4, a new mode of twisting deformation is proposed for wearable applications. The reliability of the interconnects depending on the mode and position is tested. The transition of the stress-free zone depending on the boundary conditions of the surface is proposed. Lastly, in chapter 5, the results of the thesis are briefly summarized, and future work for stress and strain analysis of future interconnects is proposed.

CHAPTER 2

Theoretical Background

2.1 Finite element method (FEM)

The finite element method (FEM) was developed to numerically solve various engineering problems, which are often expressed as governing equations consisting of partial differential equations (PDEs). The PDEs can be solved based on prescribed initial and boundary conditions, called the boundary value problem (BVP). The FEM calculates the solution of the BVP by discretizing the continuum domain with small elements instead of directly solving the PDEs. In the procedure of FE formulation, the PDEs are reformulated into the integral form, which reduces the degree of smoothness of the solutions. Therefore, the governing equations based on the partial

differential equations are restated in integral form, which are called the strong form and weak form.

For elastic models, the FEM solver calculates stress and strain values that satisfy the following two conditions. First, every element satisfies the governing equations and boundary conditions. Second, the sum of the work potential caused by force and displacement and the potential due to the internal strain energy are minimized in each element. The governing equations that determine the internal mechanical deformation are given in Eq. 1 and 2, and the weak forms for numerical calculation are given in Eq. 3 and 4, respectively [33].

$$\frac{\partial \sigma_x}{\partial x} + \frac{\partial \sigma_{xy}}{\partial y} + f_x = \rho \frac{\partial^2 u}{\partial t^2}$$

(Eq. 1)

$$\frac{\partial \sigma_{xy}}{\partial x} + \frac{\partial \sigma_y}{\partial y} + f_y = \rho \frac{\partial^2 v}{\partial t^2}$$

(Eq. 2)

$$0 = h_e \int_{\Omega_e} \left[\frac{\partial w_1}{\partial x} \sigma_x + \frac{\partial w_1}{\partial y} \sigma_{xy} - w_1 f_x + \rho w_1 \ddot{u} \right] dxdy - h_e \int_{\Gamma_e} w_1 \left[\sigma_x n_x + \sigma_{xy} n_y \right] ds$$

(Eq. 3)

$$0 = h_e \int_{\Omega_e} \left[\frac{\partial w_2}{\partial x} \sigma_{xy} + \frac{\partial w_2}{\partial y} \sigma_y - w_2 f_y + \rho w_2 \ddot{v} \right] dxdy - h_e \int_{\Gamma_e} w_2 \left[\sigma_{xy} n_x + \sigma_y n_y \right] ds$$

(Eq. 4)

In the equation, f is the body force, u and v are the displacements along the x and y directions, h_e is the thickness of the element, Ω_e is the entire domain of the element, w is the weight function, Γ_e is the closed boundary of the element, and n is the normal vector of the boundary surface.

A static model assumes that the time variable does not affect the result of the simulation ($\ddot{u}, \ddot{v} = 0$). Therefore, in the case of static analysis, the calculation requires less computing power and resources, but this assumption can lead to an error in the results. In the case of the interconnection system, the effect of time is very small, and the static assumption can be sufficiently applied to systems such as metals, silicon, and polyimide at low temperatures.

In the case of electronic devices made by film deposition on planar wafers, pattern resolution on the wafers is very important for high yield. However, with the development of technology and the increase in integration, the pattern profile in the thickness direction is becoming deeper and more complex, causing stress and strain in the normal direction of the plane, as shown in the side view in Fig. 2.1. The mechanical deformation in the cross-sectional area is important; thus, model elements based on the assumption of plane strain conditions are appropriate to predict mechanical issues that occur in the normal direction, such as warpage and leaning.

On the other hand, in the case of wearables, patch-type devices are common, which are constructed with a unit device on a flexible substrate for attachment to the human body. Since the units are arranged two-dimensionally on the surface, the in-plane strain distribution on the surface is the most important for the reliability of the

system. Therefore, the stress and strain distributions, shown in the top view in Fig. 2.1, are analyzed through general assumptions of plane stress (in very thin cases) or 3D stress conditions.

The surface traction is a vector representing the stress conditions occurring in the normal direction of the surface, i.e., the force per unit area. The surface traction boundary is useful for expressing the attractive force or compressive stress in the normal direction occurring on the surface due to surface properties. For example, the surface traction boundary is used to express the internal stress due to surface tension that occurs in materials that have strong interatomic bonding energy, such as water and a metal. Internal pressure due to surface tension occurs in the normal direction of the external surface. Furthermore, in the case of the exertion of another external force caused by various surface characteristics, the direction of the external force can be determined by coordinate transformation of the traction vector.

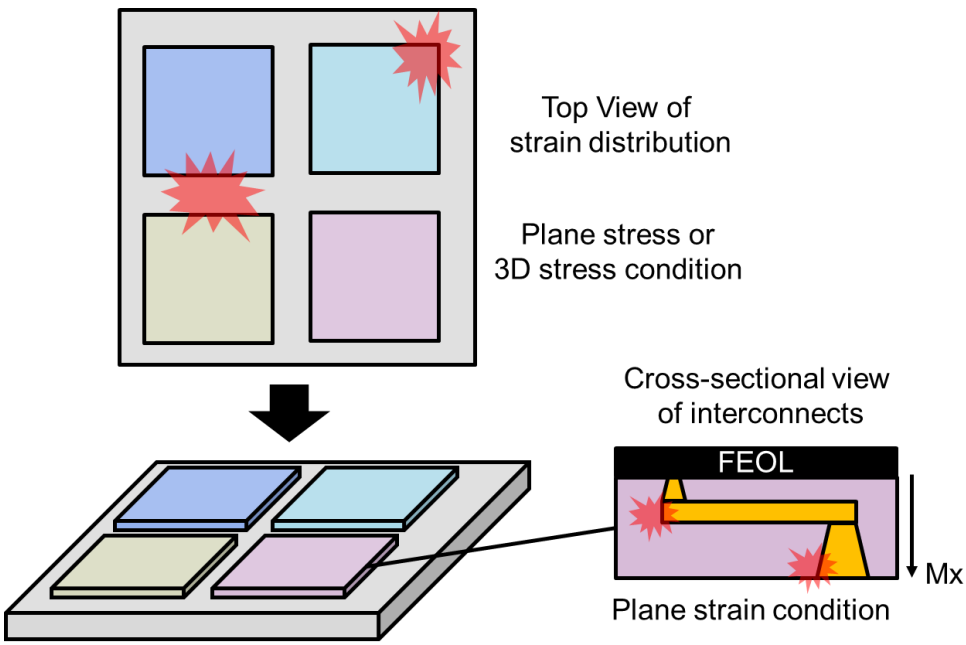

Figure 2.1 Schematic of element type stress and deformation calculation according to the interconnect case. Plane stress or 3D stress conditions are used to analyze the strain distribution on the top surface. Plane strain conditions are used to analyze the cross-sectional stress and strain.

2.2 Stress in metal films

2.2.1 Deposition technology of metal films

Thin film interconnects and dielectrics are alternately stacked through repetitive processes from the local interconnect layer to the global interconnect layer. To form as many individual lines as possible in a small space with good film quality, deposition and lithography technology has been developed in vacuum processes. Thin films are deposited through physical vapor deposition (PVD), chemical vapor deposition (CVD), atomic layer deposition (ALD), and electroplating for copper, in which the conducting material is vaporized or electrolyzed to transfer the material and form a thin film on the substrate.

PVD is the most common deposition technology because a uniform thin film can be easily formed on a large area by evaporation or sputtering, in which the target is physically separated from and the material is transferred to the surface. However, the linearity of the vapor flux is high, and it is easy to form nonuniform thin films due to structural factors such as shielding and overhang. As shown in Fig. 2.2, the microstructure of a PVD film was investigated by a structure zone model [34], in which the microstructure is modeled depending on the pressure of the inert gas and the process temperature compared to the melting point during metal sputtering. The higher the processing temperature is, the better the film, with fewer defects and larger grains obtained.

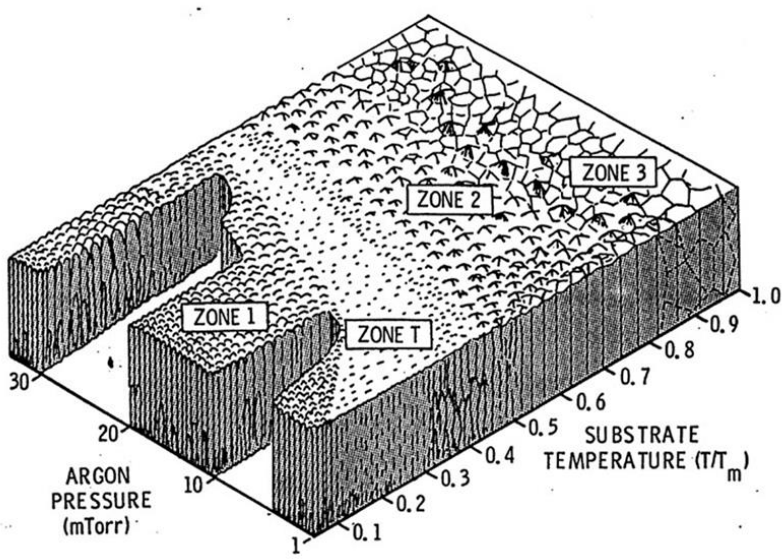

Figure 2.2 PVD structure zone model, which shows the microstructure of the film depending on the argon pressure and substrate temperature [34].

On the other hand, CVD is a deposition technology in which a thin film is formed by reaction between a precursor gas and a reactant gas on the surface using heat or plasma. CVD has the advantage of step coverage, where the thickness of the film is uniform regardless of a complex structure, such as a deep trench or hole, because the reaction of gaseous materials occurs only on the surface of the substrate. However, a high process temperature or a plasma is required since the chemical reaction should occur on the surface, microdefects remain due to the gas appearing after the reaction, and the precursor gas of the conductor is limited. On the surface, nucleus islands are generated at nucleation sites such as on linear surfaces, and films often grow in a columnar manner [35].

ALD is a deposition technology in which atomic layer formation is repeated on a surface layer by layer, and it is possible to control the film quality and thickness very precisely. However, ALD has a very low deposition rate due to the process of repeating gas injection and purging [36].

Copper can also be deposited inside a mold through a damascene process, which uses electroplating to fill the inside of the pattern without any gaps. The dual damascene process is commonly utilized to fabricate a via and a line at the same time for high reliability interconnects using copper. However, mechanical damage accumulates on interconnects and dielectrics when overdeposited copper is removed by the chemical mechanical polishing (CMP) process [37].

2.2.2 Mechanism of metal film formation

There are three primary modes of the film growth mechanism: the Volmer–Weber (VW) growth mode, Frank–van der Merwe (FM) growth mode, and Stranski–Krastanov (SK) growth mode, as shown in Fig. 2.3 [38]. The growth mode is determined by the surface energies and interface energy of the film and substrate. In the VW growth mode, known as island growth, nucleus islands are individually formed on the substrate when the surface energy of the film is larger than the surface energy of the substrate. After the formation of the islands, nucleus growth proceeds, and the islands expand their volumes and coalesce into a continuous thin film.

In the FM growth mode, known as layer-by-layer growth or two-dimensional growth, a continuous film layer is repeatedly formed when the interface energy between the film and substrate is lower than the surface energies of the film and substrate. The formation of a complete monolayer occurs before another layer starts to grow.

In the SK growth mode, known as layer-plus-island growth, islands are subsequently formed on the surface of the layer after the formation of the first layer or a few layers on the surface of the substrate when layer formation competes with island formation. Due to structural misfit between the film and substrate, nucleation occurs after coating of the film material on the substrate.

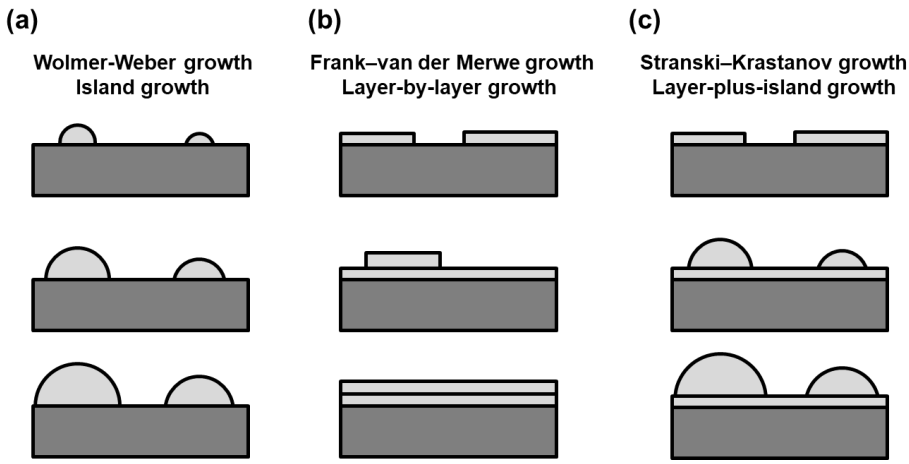

Figure 2.3 Film growth modes: (a) VW growth mode, (b) FM growth mode, and (c) SK growth mode [38].

For thin film interconnects based on metallic materials, the atomic bonding energy of the metal is very high compared to that of the substrate such as a ceramic or a polymer, and the VW growth mode is dominant regardless of the deposition method. Most metals have a relatively high surface energy (several J/m^2), so surface tension and dewetting of metal nuclei occur on the substrate and dielectric. Therefore, because the metal film grows in the VW growth mode, film stress occurs differently depending on the stage of nucleation, coalescence, or thickening.

2.2.3 Stress evolution in a metal film in VW growth mode

Metal film growth proceeds in three stages of 1) nucleation, 2) coalescence, and 3) thickening according to the VW growth mode, all of which are due to the high interatomic bonding energy of metals, which shows a strong correlation with the material properties, such as the melting point or Young's modulus. As shown in Fig. 2.4, the stress evolution of copper, which is a common metal for producing interconnects with good conductivity, was measured by piezo cantilever beam bending [39]. The stress stage depends on the film stage of the VW growth mode. Initially, compressive stress was generated in island nucleation. Then, tensile stress was generated due to impingement and coalescence. Finally, compressive stress was generated during thickening of the film.

In the initial nucleation stage of a metal island, the surface tension increases due to the high surface-area-to-volume ratio of metal islands. As shown in Fig. 2.5, the metal atoms on the island surface are attracted inward, resulting in compressive stress inside to counter the inward force of the surface atoms. Metallic nuclei are formed in a very compressed state, and bending into a convex form occurs for thin and low-stiffness substrates [41].

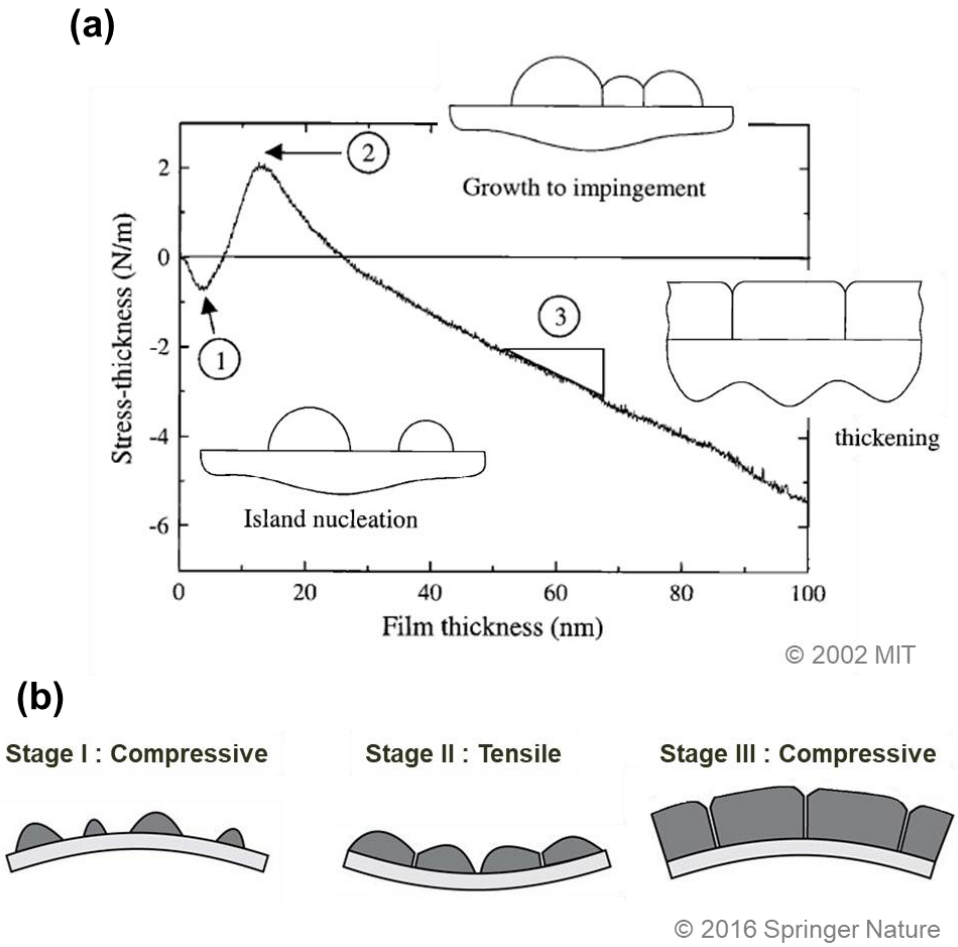

Figure 2.4 (a) Stress evolution stages of metal film deposition in VW growth mode. (b) Bent shape of the substrate due to stress evolution [39], [40].

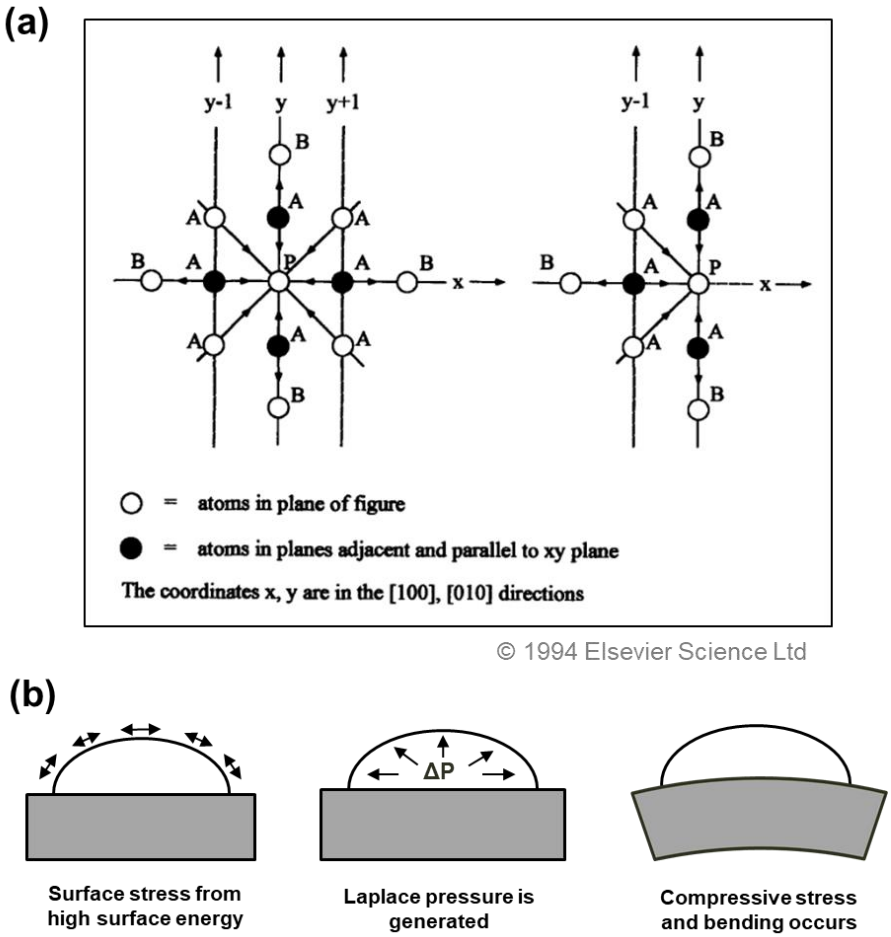

Figure 2.5 Compressive stress of a metal nucleus island due to surface stress. (a) Comparison of atomic interactions between the metal structure and surface. (b) Schematic of compressive stress and substrate bending due to surface stress [41].

Compressive stress occurs at the level where independent nuclei exist, and the stress can be calculated by the ratio of the change in the surface area to the change in the volume, as shown in Eq. 5.

$$f = \gamma + \frac{\partial \gamma}{\partial \varepsilon}, \qquad \Delta P = f\frac{dA}{dV}$$

(Eq. 5)

In the equation, f is the surface tension, γ is the surface energy, P is the internal pressure, A is the surface area of the nucleus, and V is the volume of the nucleus.

After metal islands are nucleated and grow enough to cover the substrate, the islands start contacting each other, and coalescence occurs that reduces the free surface energy by deforming mechanically, called 'zipping'. The driving force is the energy reduction in which surface energy is converted into grain boundary interface energy, and the counter force is the strain energy induced by the deformation of nuclei. A large tensile stress occurs due to the deformation of the nucleus, which occurs during the initial continuous film formation process of the nucleus, as shown in Fig. 2.6 [42].

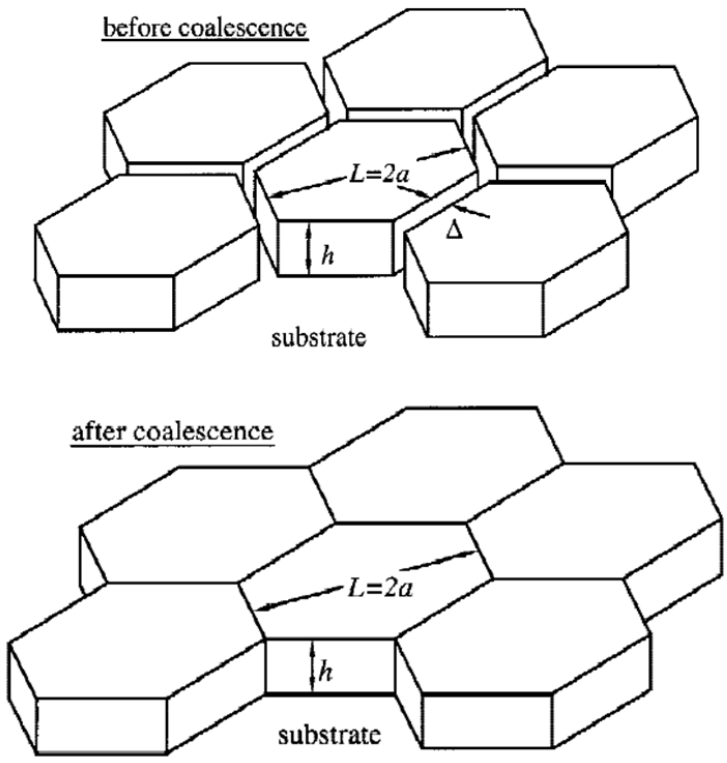

Figure 2.6 Coalescence of islands to form a continuous film to reduce the free surface energy [42].

After the coalescence is complete, compressive stress occurs through diffusion-driven relaxation. Tensile stress due to coalescence is relaxed through ad-atom diffusion to the strained region in the grain boundaries, as shown in Fig. 2.7. Ad-atoms diffuse into the grain boundaries along the film surface similar to Coble creep, which occurs through the diffusion of atoms in a material along grain boundaries, and the stress relaxation rate $\dot{\sigma}$ can be calculated by Eq. 6 [43].

$$\dot{\sigma} = -\frac{C_0}{h^3}\sigma \exp\left(-\frac{Q}{kT}\right)$$

(Eq. 6)

where C_0 is a material-dependent constant, h is the film thickness, Q is the activation energy for diffusion, k is Boltzmann's constant, and T is the temperature.

Since this relaxation occurs due to the migration of ad-atoms supplied by vapor flux, the relaxation rate is greatly affected by the mobility of ad-atoms, and in the case of materials with low mobility, stress is not relieved, and tensile stress remains. Therefore, because the diffusion rate is a dominant factor in this relaxation, different relaxations occur during thin film growth depending on the melting point of the metal and the deposition temperature.

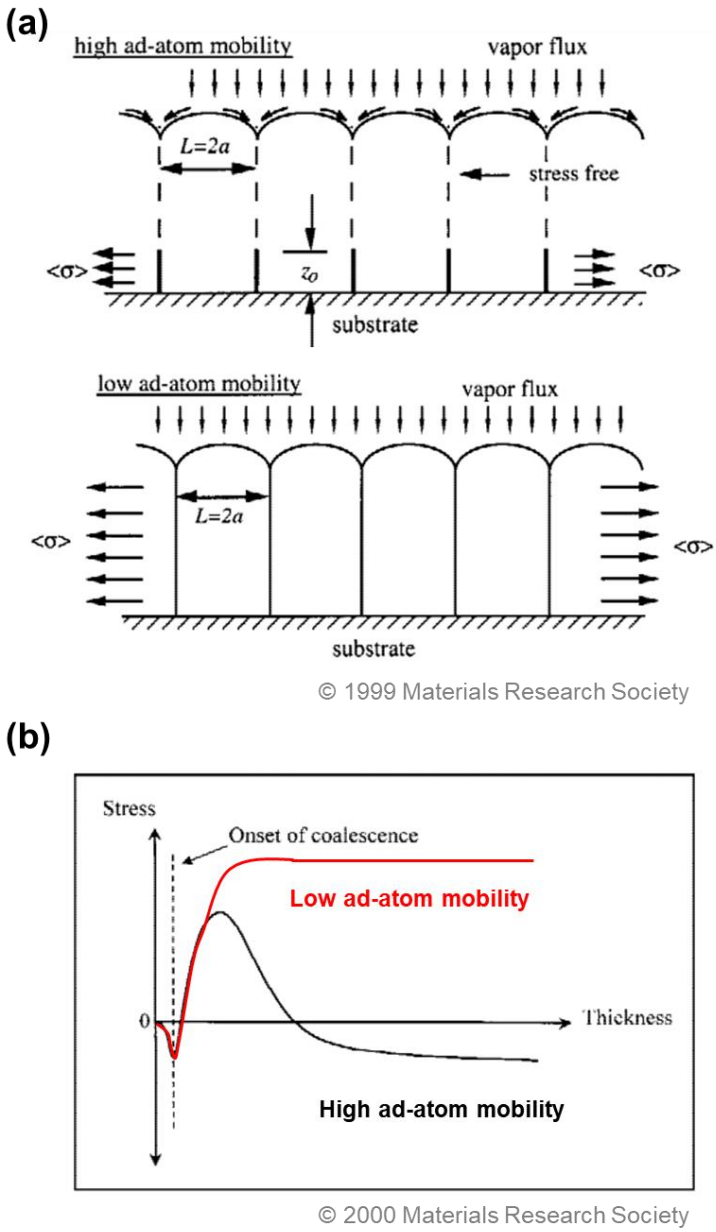

Figure 2.7 (a) Stress relaxation due to ad-atom diffusion on the surface. (b) Stress-thickness curve depending on the ad-atom mobility, which affects the relaxation rate [42-44].

2.3 Calculation of the tensile stress due to coalescence

2.3.1 Nix-Clemens model (W. D. Nix, 1999 [42])

The Nix-Clemens model is an analytical equation for calculating stress by grain, considering an array of 2D cross-sectional metal nuclei with an elliptical shape. The analytical equation of film stress is based on the energy balance between grain boundary formation and the energy release rate of grain boundary opening at cusps along the grain boundaries. In the coalescence process, the surfaces of the islands spontaneously stick together because the grain boundary energy is less than the energies of the two free surfaces. Since the islands have a rounded top surface, the extension of the islands forms sharp, crack-like features on the surface of the film, as shown in Fig. 2.8 [45].

To calculate the stress, approximation of the shape of the strained island surface as a cycloid is used to describe the energetics of the crack-like cusps. The stress intensity factor K at the crack-like cusps depends on the average stress ⟨σ⟩ in the island, and the Griffith energy release rate G of crack opening can be calculated by Eq. 7.

$$K = -\frac{1}{1+v}\langle\sigma\rangle\sqrt{a}\,,$$

$$G = (1-v^2)\frac{K}{E} = \frac{(1-v)}{(1+v)}\frac{\langle\sigma\rangle^2 a}{E}$$

(Eq. 7)

In the equation, v is Poisson's ratio, ⟨σ⟩ is the average stress, a is the nucleus width, and E is Young's modulus.

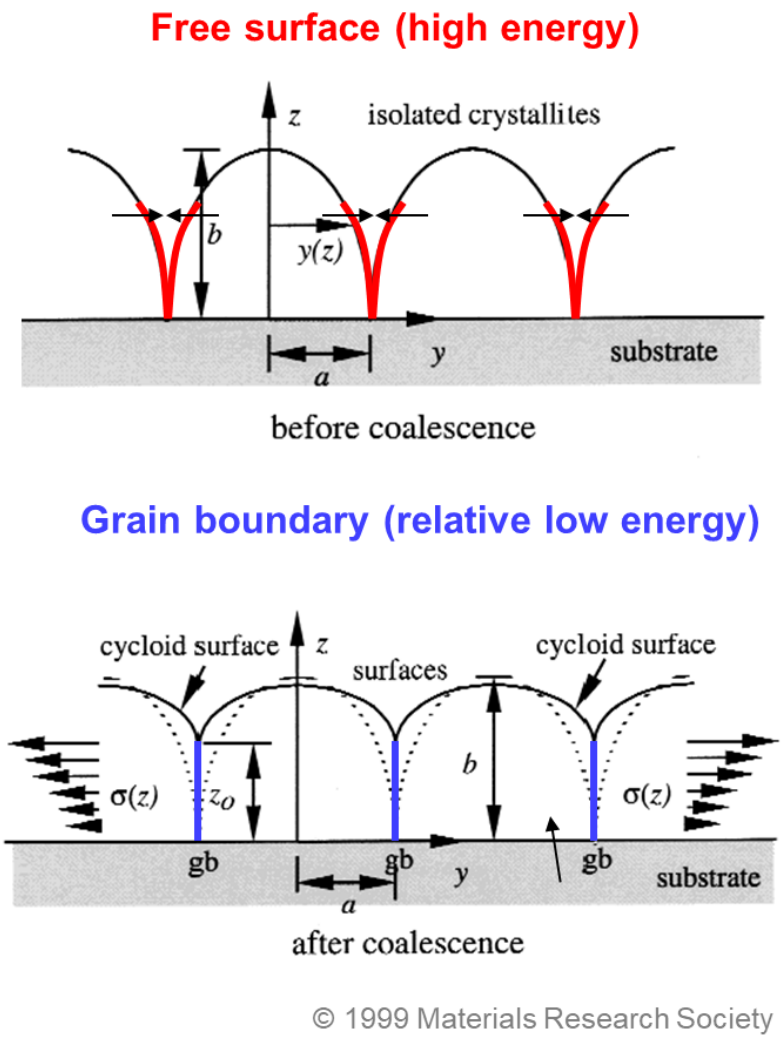

Figure 2.8 Schematic of the Nix-Clemens model for tensile stress calculation during coalescence [42].

The coalescence shows elastic displacement and stress of nucleus islands during the formation of a continuous film. The sharp cusps at the grain boundaries act as cracks, and the crack extension force for plane strain competes with grain boundary formation, where the surfaces of islands coalesce into an interface with low energy. The crack extension stops when the energy increase of new free surfaces at the grain boundaries is equal to the Griffith value, and the average stress in the metal island can be calculated by Eq. 8.

$$G = \frac{(1-v)}{(1+v)}\frac{\langle\sigma\rangle^2 a}{E} = \left(2\gamma_s - \gamma_{gb}\right),$$

$$\langle\sigma\rangle = \frac{(1+v)}{(1-v)}E\frac{\left(2\gamma_s - \gamma_{gb}\right)}{a}$$

(Eq. 8)

In the equation, γ_s is the surface energy, and γ_{gb} is the grain boundary energy.

Based on the above formulas, the length of the interface z_0, called the zipping distance, can be calculated, which is the grain boundary height determining how much zipping and film stress occurs for the specific shape of islands and average stress. The zipping distance z_0 is also calculated by the average tensile strain of the elliptical islands in Eq. 9 and 10.

$$\varepsilon(z) = 1 - \sqrt{1 - \left(\frac{z}{b}\right)^2},$$

$$\langle\varepsilon\rangle = \frac{1}{z_0}\int_0^{z_0} \varepsilon(z)dz,$$

$$\langle\sigma\rangle = \frac{E}{1 - v^2},$$

$$\langle\varepsilon\rangle = \frac{E}{1 - v^2}\left\{1 - \frac{1}{2}\sqrt{1 - \left(\frac{z_0}{b}\right)^2} - \frac{b}{2z_0}\arcsin\left(\frac{z_0}{b}\right)\right\},$$

$$\langle\varepsilon\rangle \approx \frac{E}{6(1 - v^2)}\left(\frac{z_0}{b}\right)^2$$

(Eq. 9)

$$\frac{z_0}{b} = \sqrt[4]{\frac{36(1 - v)(1 + v)^3\left(2\gamma_s - \gamma_{gb}\right)}{Ea}}$$

(Eq. 10)

In the equation, z_0 is the zipping distance, and b is the nucleus height.

The film stress calculated by Eq. 8 is an overestimation of the actual stress generated during film growth because of the assumption that all islands contact each other at the same time, with the consequence that no shear stress is developed on the islands. No sliding of the crystallites occurs at the interface of the islands and substrate. A more realistic stress can be calculated by considering that islands with different shapes and sizes coalesce at different times.

2.3.2 FEM calculation (S. C. Seel, 2000 [43])

The previous Nix–Clemens model of coalescence of metal films provides an intuition of the tensile stress that is generated during the VW growth mode, which is calculated by a simple analytical equation. However, the model predicts higher tensile stress than the realistic stress measured in experiments. By performing FEM calculations, coalescence can be represented in a straightforward manner, and more accurate stress compared with experimental results can be predicted.

Half of a hemisphere island was modeled by a two-dimensional element under plane strain conditions and pinned on the substrate interface, as shown in Fig. 2.9 (a). The plane strain condition implies that island deformation is similar to two infinitely long cylinders deforming. Therefore, there is no strain normal to the cross-section, and the stress–strain relation of the plane strain condition model in elastic deformation is given in Eq. 11 [33].

$$\varepsilon_x = \frac{\partial u}{\partial x}, \qquad \varepsilon_y = \frac{\partial v}{\partial y}, \qquad 2\varepsilon_{xy} = \frac{\partial u}{\partial y} + \frac{\partial v}{\partial x},$$

$$\varepsilon_{xz} = 0, \qquad \varepsilon_{yz} = 0, \qquad \varepsilon_z = 0,$$

$$\begin{bmatrix} \sigma_x \\ \sigma_y \\ \sigma_{xy} \end{bmatrix} = \frac{E}{(1+\nu)(1-2\nu)} \begin{bmatrix} 1-\nu & \nu & 0 \\ \nu & 1-\nu & 0 \\ 0 & 0 & \frac{1-2\nu}{2} \end{bmatrix} \begin{pmatrix} \varepsilon_x \\ \varepsilon_y \\ 2\varepsilon_{xy} \end{pmatrix}$$

(Eq. 11)

As shown in Fig. 2.9 (a), a series of displacements were applied along the surface to the zipping distance z_0 to mimic the zipping. Due to the deformation of the island, the strain energy of the island in the FEM model increases, and the sum of the reduced surface energy and increased interfacial energy decreases. The sum of these two energies was calculated as a function of the zipping distance, and the lowest energy state was found for a given island radius. As shown in Fig. 2.9 (b), the average stress of a silver island was calculated depending on the radius, and then, the entire film stress was calculated by accumulating the stress of each island with different radii according to the island coverage on the substrate, as shown in Fig. 2.9 (c).

However, this FEM model is only suitable for predicting the stress of high adatom mobility metals such as silver. The zipping of the surface and mechanical deformation occur only in the initial contact between the islands, and diffusion-driven relaxation occurs during deposition; thus, the tensile stress is relieved as deposition proceeds. Therefore, this model cannot be applied to predict the stress of metal films when the deposition temperature is low or a refractory metal with a high melting point is deposited.

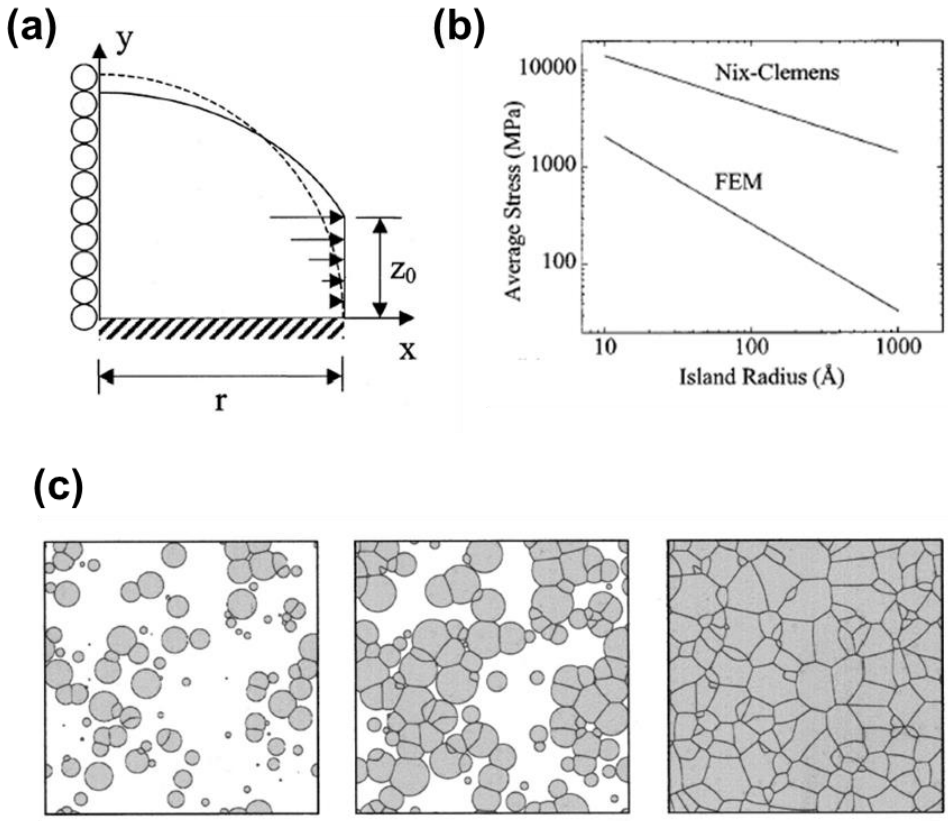

Figure 2.9 FEM model for calculation of the coalescence stress. (a) Schematic of the boundary conditions of the nucleus model. A displacement is applied on the surface to mimic coalescence. (b) Average stress of the Nix-Clemens model and FEM simulation depending on the island radius. (c) Change in the film coverage of metal islands in the simulation model during island growth by deposition [43].

2.4 Stress-free zone of mechanical deformation

2.4.1 Neutral axis in bending deformation

The neutral axis is the location where no longitudinal stress, either compressive or tensile stress, exists due to cancellation of the stress field through compensation. As shown in Fig. 2.10 (a), bending deformation occurs in a plate with bending radius R, and the dotted line that passes through the centroidal depth of the beam is the neutral axis. The upper part of the beam above the neutral axis is under tensile stress, whereas the lower part of the beam is under compressive stress in this simple bending deformation. In the homogeneous plate in Fig. 2.10 (a), these tensile and compressive stresses are cancelled out at the geometric center of the plate, called the neutral axis.

The bending strain and stress occurring in the elastic plate along the thickness direction, which is the y-axis, are calculated by Eq. 12 and 13, respectively.

$$\varepsilon_y = \frac{\Delta l}{l_0} = \frac{\pi(R+y) - \pi R}{\pi R} = \frac{y}{2R},$$

(Eq. 12)

$$\sigma_x = E\varepsilon_y = \frac{Ey}{2R}$$

(Eq. 13)

where R is the bending radius of the deformation and y is the displacement from the neutral axis.

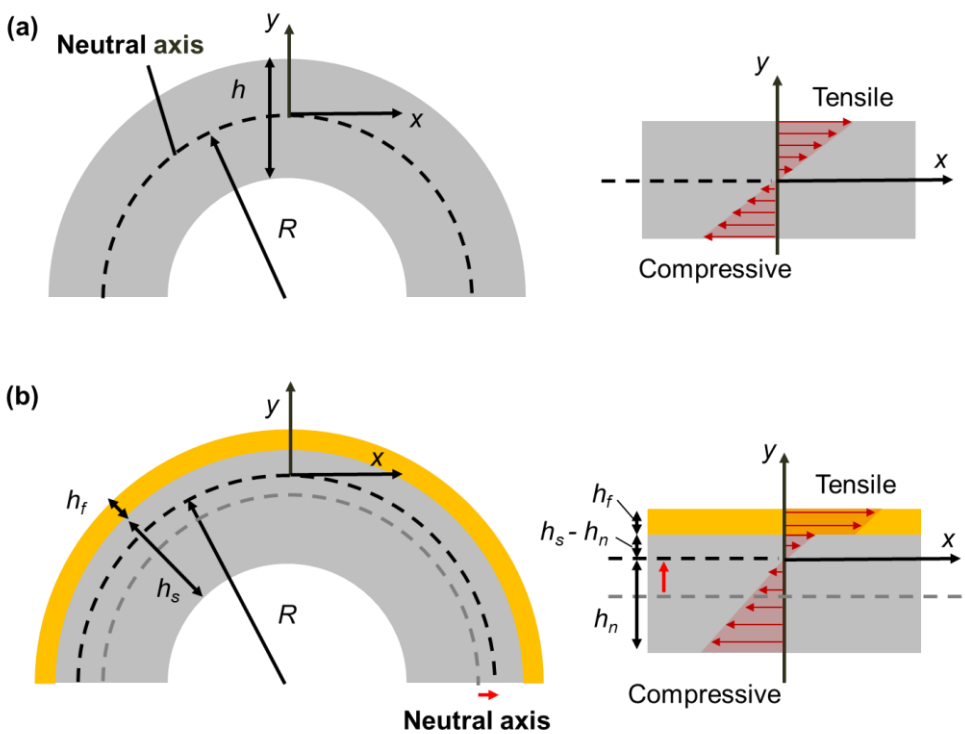

Figure 2.10 Schematic of bending deformation and stress profile in the cross-section of (a) a homogeneous plate and (b) a bilayer plate with a metal film (h_f) and a polymer substrate (h_s) with a new neutral axis from the bottom (h_n).

However, in the case of heterogeneous films, such as interconnects of metal films on polymer substrates, the stress profile changes due to the mechanical stiffness of each film. As shown in Fig. 2.10 (b), the stress profile of a bilayer with a metal film and a polymer is different from that of the homogeneous plate, and the neutral axis shifts to the rigid metal film. To satisfy the balance of forces in bending, the sum of the bending stresses along the x-axis is zero, which can be expressed as Eq. 14, when both the film and the substrate are elastic.

$$\int_{-h_b}^{h_s-h_n} \sigma_{x,s} dy + \int_{h_s-h_n}^{h_s-h_n+h_f} \sigma_{x,f} dy = 0,$$

$$\frac{E_s}{2R}\int_{-h_b}^{h_s-h_n} y dy + \frac{E_f}{2R}\int_{h_s-h_n}^{h_s-h_n+h_f} y dy = 0$$

(Eq. 14)

where h_f is the film thickness, h_s is the substrate thickness, h_n is the height of the substrate below the neutral axis, $\sigma_{x,s}$ is the stress in the substrate, $\sigma_{x,f}$ is the stress in the film, E_s is the Young's modulus of the substrate, and E_f is the Young's modulus of the film.

Finally, the shift of the neutral axis according to the Young’s moduli of the film and substrate can be calculated as in Eq. 15.

$$h_b = \frac{1}{2}\frac{E_s {h_s}^2 + E_f {h_f}^2}{E_s h_s + E_f h_f}$$

(Eq. 15)

In the case of bending deformation, the position of the neutral axis can be shifted by controlling the mechanical properties and thickness of the laminated film, as shown in Fig. 2.11. To improve the mechanical reliability of conducting films, many studies of the neutral axis are being conducted to protect mechanically weak films by positioning them on the neutral axis [46].

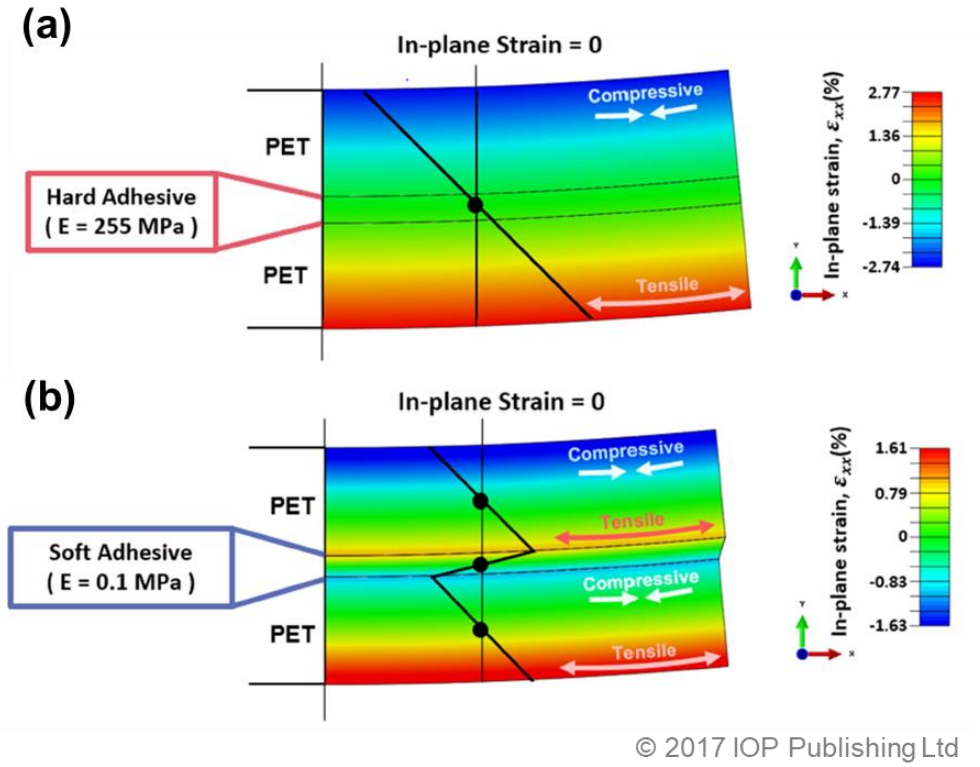

Figure 2.11 In-plane strain distributions in the thickness direction under bending and the location of the neutral planes. (a) Hard adhesive layer case showing a symmetric strain distribution. (b) Multiple neutral planes were generated by the soft adhesive layer, which is easily shear deformed and separates the two films [46].

2.4.2 Stress-free zone in twisting deformation

Twisting deformation causes biaxial and multicomponent stresses in the thin film and substrate, which is the deformation mode that can occur in body motion or in the user environment. In the past, studies on twisting deformation have focused on torsional deformation, which is represented by the shear strain generation caused by torque in structural materials, as shown in Fig. 2.12 (a).

The shear stress of a circular rod under torsional deformation is proportional to the distance from the rotation axis, ρ, and rotation angle, θ, and inversely proportional to the length of the rod. Therefore, the shear stress, γ, can be calculated by Eq. 16, and the stress-free zone where no stress occurs is on the rotation axis at any angle.

$$\gamma = \frac{\theta\rho}{L}$$

(Eq. 16)

where θ is the rotation angle, ρ is the distance from the rotation axis, and L is the length of the rod.

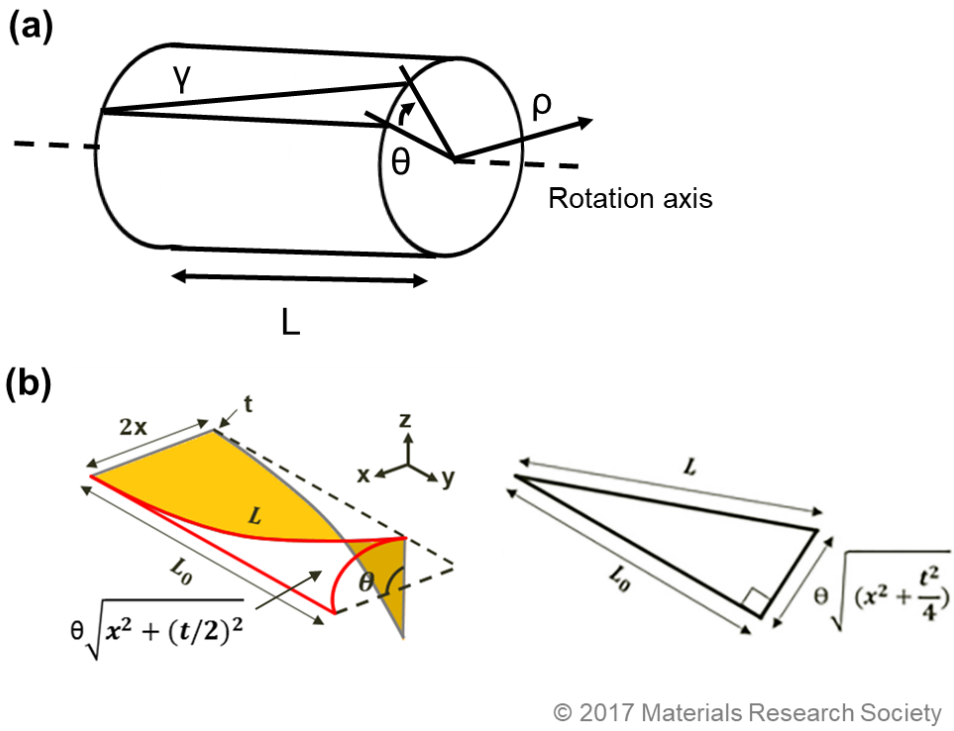

Figure. 2.12 Schematic of twisting deformation modes: (a) Torsional deformation with perfect shear. (b) Twisting deformation of a plate substrate in a thin film system [47].

However, in the case of a thin and wide plate type of substrate for integrating wearable devices, not only shear stress but also normal stress occurs when the plate is twisted, as in rotational joints such as the wrist or neck. The twisting deformation in the plate-shaped substrate, as shown in Fig. 2.12 (b), causes tensile stress on the edge of the substrate, which can be calculated by Eq. 17 when the thickness of the substrate t is very small [47].

$$\varepsilon_{tensile} = \frac{L - L_0}{L_0} = \frac{\sqrt{{L_0}^2 + \Theta^2\left(x^2 + \frac{t^2}{4}\right)} - L_0}{L_0},$$

$$\varepsilon_{tensile} \approx \sqrt{1 + \left(\frac{\Theta x}{L_0}\right)^2} - 1 \ (\because \ t \ll x)$$

(Eq. 17)

where θ is the rotation angle, x is the distance from the rotation axis, L_0 is the length of the substrate, and t is the thickness of the substrate.

This tensile stress greatly increases with the distance x from the rotation axis. Therefore, even when twisting occurs in this plate-type substrate, placing a device on the rotation axis is advantageous for mechanical reliability.

CHAPTER 3

Stress Analysis of Tungsten Film and Interconnects Due to Coalescence in Trench Mold

(Published, *IEEE Access*, 2022 [48])

3.1 Introduction

As the shrinkage of electronic devices progresses, the dimension of metal interconnects also decreases, and the pattern of interconnects becomes more precise [16]. Therefore, the deposition technology to fabricate fine-pitch metal patterns has become very important. Thin film is deposited inside a deep trench mold to form

interconnections with a large cross-sectional area in a limited space. Among the conducting metals, tungsten shows good gap-filling characteristics due to its high step coverage obtained through chemical vapor deposition. Tungsten is commonly used as an interconnection metal for vertical patterns due to its advantage of being able to fill the inside of a deep trench mold with a narrow width and pitch. Thus, it has been used to fill the inside of a deep mold and make vertical structures with high aspect ratios, such as via and plug structures as shown in Fig. 3.1 [49], [50].

In addition, as the pitch of interconnects decreases, the cross-sectional area reduction due to the barrier of copper interconnects is becoming a problem. Among metals, copper easily diffuses into other materials such as dielectric and causes failures such as time dependent dielectric breakdown (TDDB). Therefore, a barrier layer at least 3 nm such as TaN is required, and electrical resistance increases rapidly with scale down in M1 interconnects as shown in Fig 3.2 [51]. On the other hand, refractory metals such as tungsten have high cohesive energy between atoms and the activation energy required for self-diffusion as shown in Fig. 3.3 [52]. The refractory metals are resistant to diffusion-induced failure due to atomic migration, and do not require a barrier layer. Therefore, the refractory metals such as tungsten, ruthenium, and molybdenum have advantages in miniaturization, and are emerged as next-generation materials for M1 level interconnects with fine pitch.

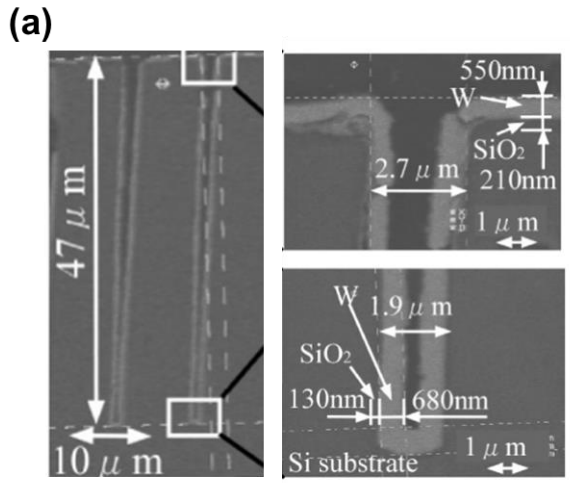

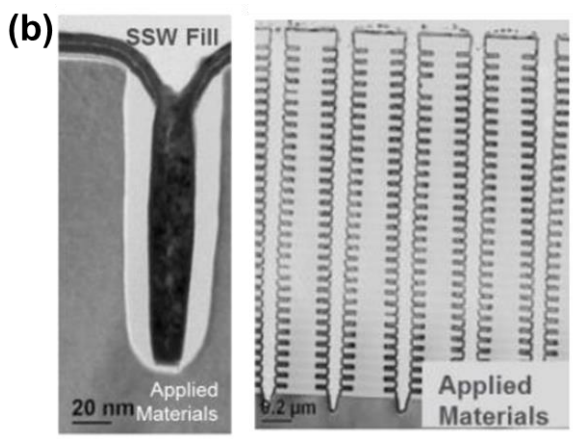

Figure 3.1 Deep trench pattern filled by tungsten deposition (a) Single trench filling. (b) Multiple pattern filling [49], [50].

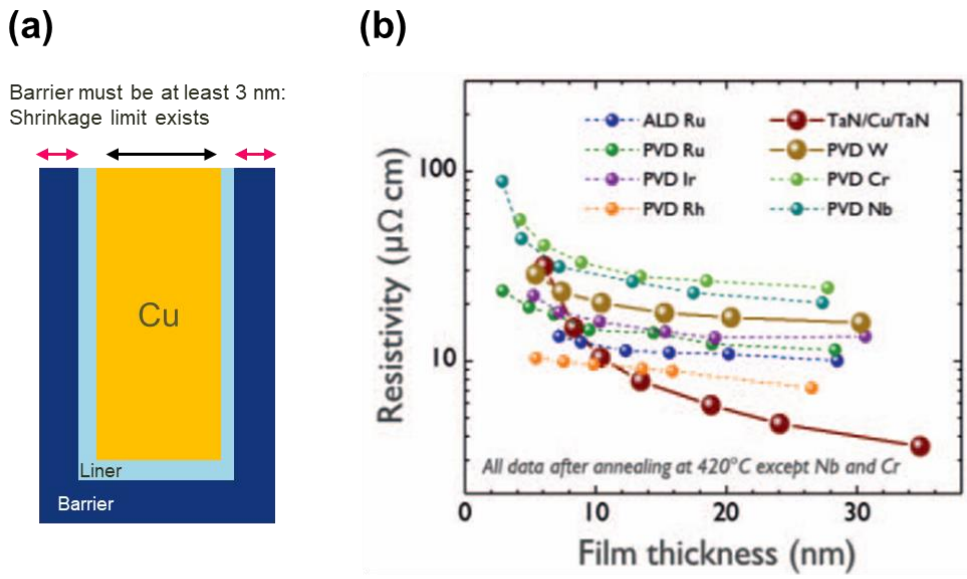

Figure 3.2 Limits of copper interconnects. (a) Schematic of reduced cross-sectional area due to barrier layer. (b) Electrical resistance depending on the thickness of film, copper with TaN barrier system shows a high increase in electrical resistance under 10 nm [51].

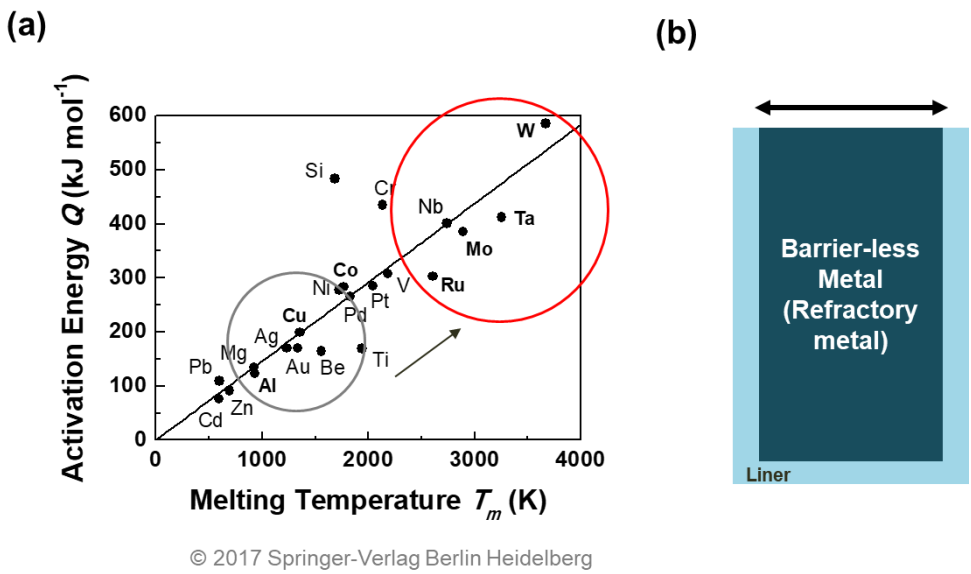

Figure 3.3 Refractory metal for barrier-less interconnects. (a) Activation energy of self-diffusion depending on melting point of metals. Atomic migration is inversely proportional the melting points. (b) Schematic of barrier-less interconnects [52].

However, when tungsten is used to fill a vertical trench mold with a high aspect ratio and narrow pitch, pattern distortion occurs by deposition stress in the metal thin films such as the bending of the mold [53], [54]. Fig. 3.4 is a schematic and diagram showing the stage of stress evolution and the bending of the vertical trench mold when filling the trench and fabricating a line pattern with metal. The main source of tensile stress in trench mold bending is twofold. First, the intergranular coalescence and corresponding stress are attributed to the deformation of the trench mold as the metal nuclei on the wall coalesce into a continuous thin film. Second, when the films on both walls are sufficiently grown and contact to each other at the center of the trench, the interfilm coalescence occurs through the grain boundary formation between the films, which reduces the top surface of the film.

In the case of the deep trench structure for the line pattern, deposition stress causes the bending of the vertical mold, which separates the line patterns in Fig. 3.4 (b). The vertical mold is bent, as shown in the plot schematic of Fig. 3.4 (c), during the coalescence stage. Interfilm coalescence causes larger mold bending than intergranular coalescence because the area of the grain boundary formed between films is much wider than that of intergranular coalescence. Deposition stress and mold bending lead to mechanical failure, such as the leaning and poor gap filling caused by the bending of the vertical trench mold [54], [55].

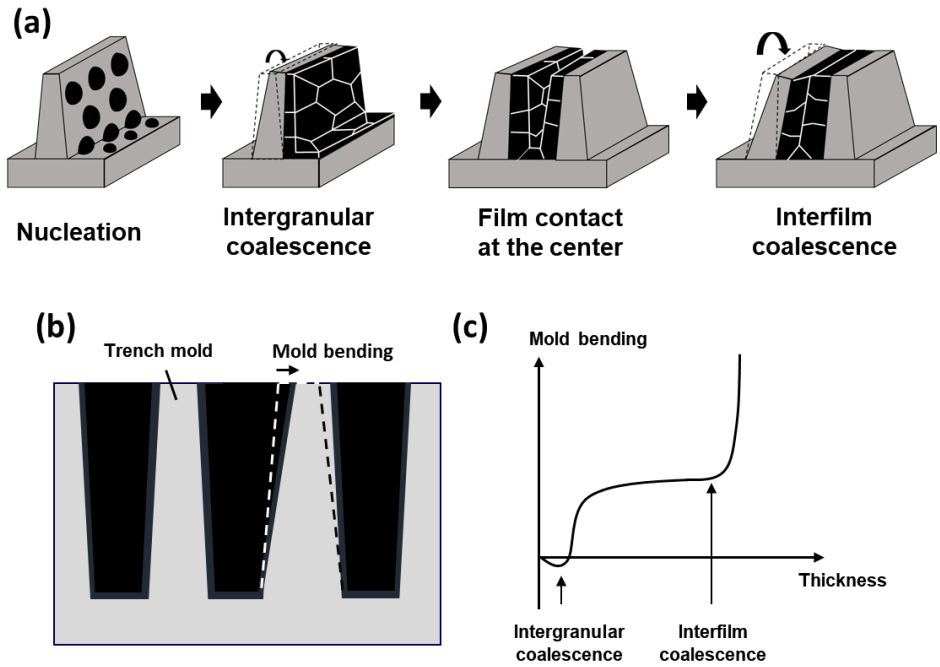

Figure 3.4 (a) Schematic of the stress evolution stage in the trench filling process that forms a line pattern with a high aspect ratio. Intergranular coalescence occurs only in the sidewall of the mold, and interfilm coalescence is caused by interaction between the free surfaces of both films. (b) Schematic of cross-sectional illustration of mold bending due to film stress on the trench mold, which vertically separates the line pattern. (c) Schematic plot of mold bending caused by coalescence versus thickness.

The main source of tensile stress during metal film deposition is the mechanical deformation of metal nuclei due to coalescence, which is called the zipping phenomenon [42], [43], [56]. The nucleus islands with rounded shape deform to reduce the free surface with high energy, while they also form grain boundaries with relatively low energy when the islands contact each other. Tensile stress from coalescence has been estimated by analytical solutions [42] or numerical methods, such as the finite element method (FEM) [43], [57] in chapter 2. Those models calculated the deposition stress of high ad-atom mobility metals such as aluminum, silver, and copper, which show low stress due to diffusion-driven relaxation under low temperature deposition [44], [58], [59].

However, previous zipping models of high ad-atom mobility metals are not suitable for calculating the stress of refractory metals such as tungsten, molybdenum, and ruthenium. Refractory metals show higher deposition stress because of their low ad-atom mobility and high surface energy. Mechanical deformation due to zipping is continuous even after the film is formed, and diffusion-driven relaxation does not occur under the low temperature of deposition process [58], [60]. Therefore, stress control in the early stage, such as the nucleation stage, is more important to reduce the deposition stress than in the case of high ad-atom mobility metals.

Our study proposes a method for calculating deposition stress considering the continuous stress evolution in intergranular coalescence and additional stress evolution of a 3D structure due to interfilm coalescence. Furthermore, controlling initial shape of the tungsten nuclei was proposed to suppress zipping deformation

and reduce the stress of the tungsten film in the intergranular coalescence stage as shown in Fig. 3.5.

The coalescence phenomenon was simulated, and stress was analyzed by using finite element (FE) simulation. The stress depending on the nuclei shape was calculated during the growth of the tungsten film. Based on calculated stress, the mold bending of the vertical mold was also calculated by a 2D cross-sectional model of a deep trench. In addition, the mold bending resulting from interfilm coalescence between the films on the walls in the middle of the trench was analyzed.

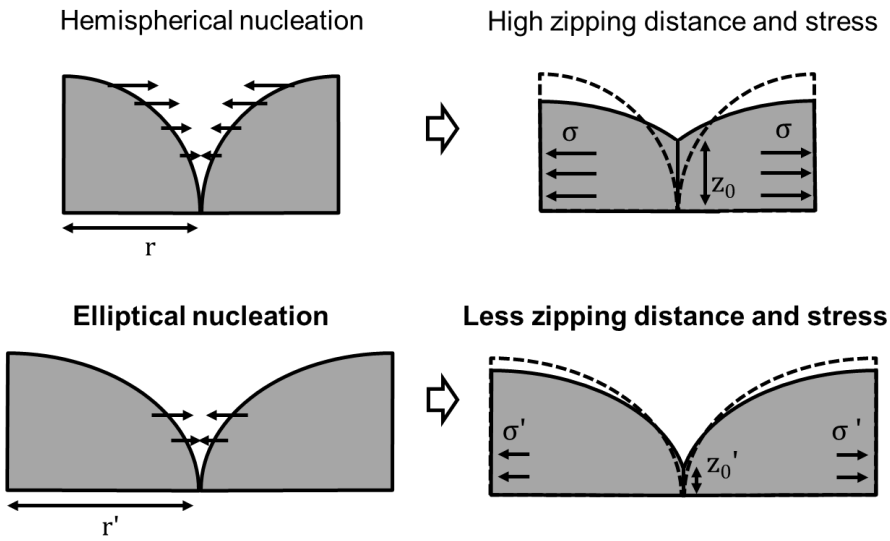

Figure 3.5 Schematic of the coalescence stress depending on nuclei shape. The wide elliptical shape is less zipped, resulting in lower coalescence stress.

3.2 Simulation details and procedure

FEM simulation was conducted using a static implicit solver, ABAQUS Standard (Dassault System, France), which has advantages for structural analysis with solid–solid contacts under nonlinear deformation. All simulations were performed in 2D models with plane strain elements, CPE4 element type in ABAQUS, which is a 2D-type element that is used in cross-sections in thick structures and is assumed to have zero strain in the thickness direction [33]. The material properties of tungsten and Si mold were assumed to exhibit linear isotropic elasticity with a Young's modulus and Poisson's ratio in Table 3.1 [61], [62]. For intergranular coalescence simulations for tungsten, surface energy and grain boundary energy of tungsten is in the table 3.1 [63]. In addition, intergranular coalescence simulations for molybdenum and ruthenium, which have the same growth mechanism as tungsten, were performed. The stress depending on the nuclei shape was calculated by applying the mechanical properties of molybdenum and ruthenium in Table 3.1 [63-66].

	Elastic modulus (GPa)	Poisson's ratio	Surface energy (J/m^2)	Grain boundary energy (J/m^2)
W	300	0.28	2.83	1.08
Mo	324	0.29	2.05	0.61
Ru	414	0.25	3.08	1.12
Si mold	127	0.278	-	-

Table. 3.1 The mechanical properties of metals and Si mold [61-66].

To calculate two major stress generation stage analysis models, intergranular coalescence and interfilm coalescence, and the nuclei and film in mold models shown in Fig. 3.6 (a) and (b) were used, respectively. The height of the tungsten nucleus is t_i = 30 Å, and the radius of the width, r, is 15 Å ~ 240 Å, as shown in Fig. 3.6 (a). The ratio of width-to-height (r/t_i) indicates the degree to which the nucleus is laterally formed. For the Si mold models to calculate interfilm coalescence, the two cases of mold pattern defects with depth and width differences from the ideal pattern are presented to calculate mold bending from the asymmetric bending moment in Fig. 3.6 (b).

The stress calculation proceeded in the order of the flow chart of Fig. 3.7. Stress calculation was conducted by an elastic model under static conditions, the boundary condition between the nucleus and the mold at the bottom of the mold was pinned, and an x-axis symmetric boundary condition was given to both sides of the model for periodic planes. Then, the zipping analysis was performed by applying the boundary condition of the force that the metal surfaces feature traction toward each other. The strain energy and zipping distance, z_0 were calculated by applying a surface traction from 0 to 20 GPa on the surface of the nucleus, depending on the value of r/t_i.

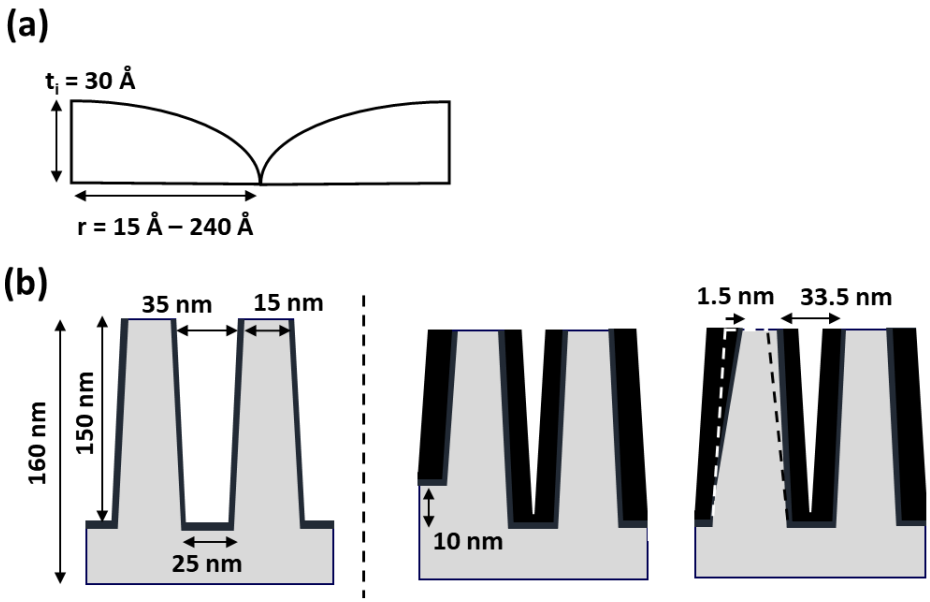

Figure 3.6 (a) Schematic of the model used to calculate film stress in intergranular coalescence caused by contact between metal nuclei, depending on the ratio of width-to-height (r/t_i) of nuclei. (b) Schematic of the trench mold used to calculate mold bending due to interfilm coalescence during the trench filling process.

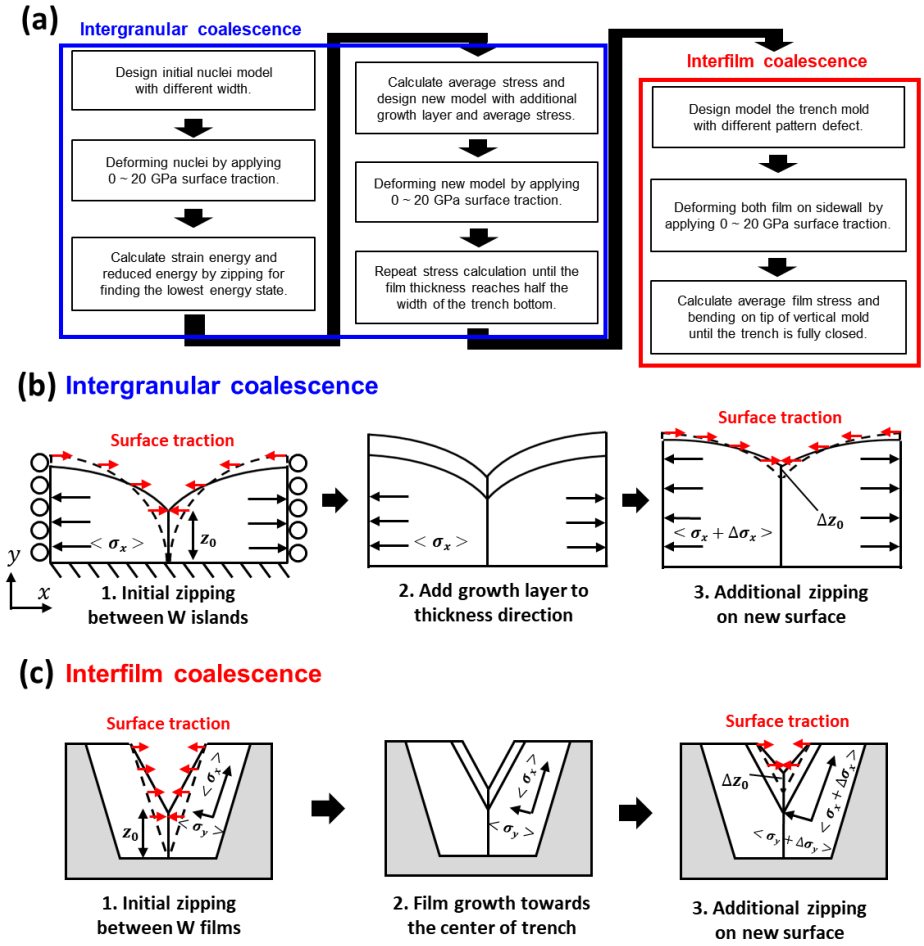

Figure 3.7 (a) The flow chart of the simulation procedure of intergranular coalescence (blue box) and interfilm coalescence (red box), respectively. (b) Schematic image of the simulation model of intergranular coalescence between tungsten islands during film growth and (c) the simulation model for interfilm coalescence occurring in the center of the trench mold to form a line pattern. Both models were deformed by surface traction to calculate film stress and mold bending.

The energy change from zipping was calculated Eq. 18, which considers decreasing free surface energy and increasing grain boundary energy due to the zipping process [42]:

$$\Delta E_{total} = \Delta E_{strain} + z_0(\gamma_{gb} - 2\gamma_s)$$
$$= \Delta E_{strain} + \Delta E_{zipping}$$

(Eq 18)

where γ_{gb} is the grain boundary energy and γ_s is the surface energy of tungsten in Table 3.1 [63]. By balancing the strain energy and reduced energy by zipping, the average stress could be calculated from the state with the lowest energy as shown in Fig 3.8.

For zipping and stress analysis during film growth, a stress-free growth layer with a thickness of 2.24 Å was added by calculating the interplanar distance of the tungsten (110) plane, and surface traction was applied to the new surface. Then, the average stress in the film was calculated through the same zipping analysis. By calculating the average stress through incremental growth, which was repeated until the target thickness just before contact at the center of the trench, the stress evolution during film growth was obtained. The schematic procedure for the calculation of stress during film growth is shown in Fig. 3.7 (b). The initial value of the film stress is negative (compressive stress) due to the surface tension [44], [67] in chapter 2:

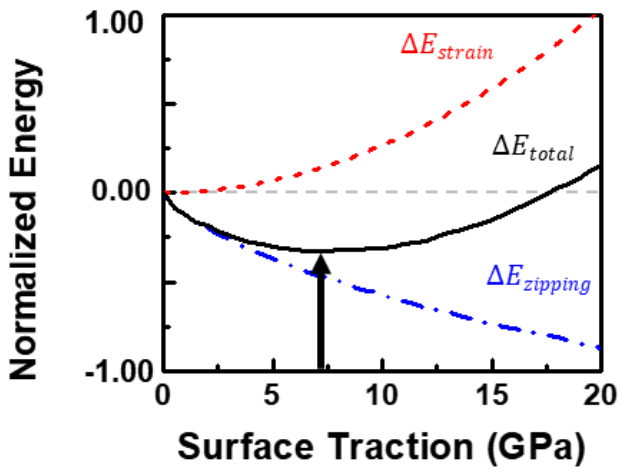

Figure 3.8 The lowest state calculation by the sum of increased strain energy and decreased zipping energy.

The zipping between the tops of the films was also analyzed, and the average stress in the horizontal and vertical directions inside the film was calculated, as shown Fig. 3.7 (c). Surface traction was applied to the surface of the film, and strain energies due to deformation and z_0, which formed as a grain boundary, were calculated. The average stress was also calculated at the state when the balance between the strain energy and the energy reduced by grain boundary formation was lowest. To quantify the bending of the trench mold due to geometrical defects, mold bending was defined in this study by measuring the displacement of the tip of the vertical mold between the trenches during the growth of the tungsten film on each wall until the pattern was closed.

3.3 FEM simulation result of tungsten stress

3.3.1 Nuclei shape dependence on intragranular coalescence

The result of calculating strain energy and zipping energy depending on surface traction to calculate the intergranular coalescence of each r/t_i model is shown in Fig. 3.9. The strain energy increased, and the absolute value of zipping energy decreased as the value of r/t_i increases, which corresponds to the increased principal axis of the elliptical shape of the nuclei along the horizontal direction. This is because the energy required for deformation increases due to the expended volume, but the increase in the surface-to-volume is small, resulting in a narrow grain boundary. The change in each of these energies is leads to reduced stress in the nuclei by the suppressed zipping. When the r/ti ratio increases above 5, zipping becomes negligible.

Fig. 3.10 (a) and (b) illustrate the FEM simulation results of the normalized zipping distance and the normalized average nuclei stress, which show the nuclei shape effect on intergranular coalescence at initial contact. Note that the first and second contributions correspond to a counter force of the zipping phenomenon and a driving force of the zipping phenomenon, respectively. Therefore, zipping is suppressed as the nuclei converge to an ellipse with a wider shape, and the shape factor with the value of r/ti above 5 can be regarded as the critical ratio.

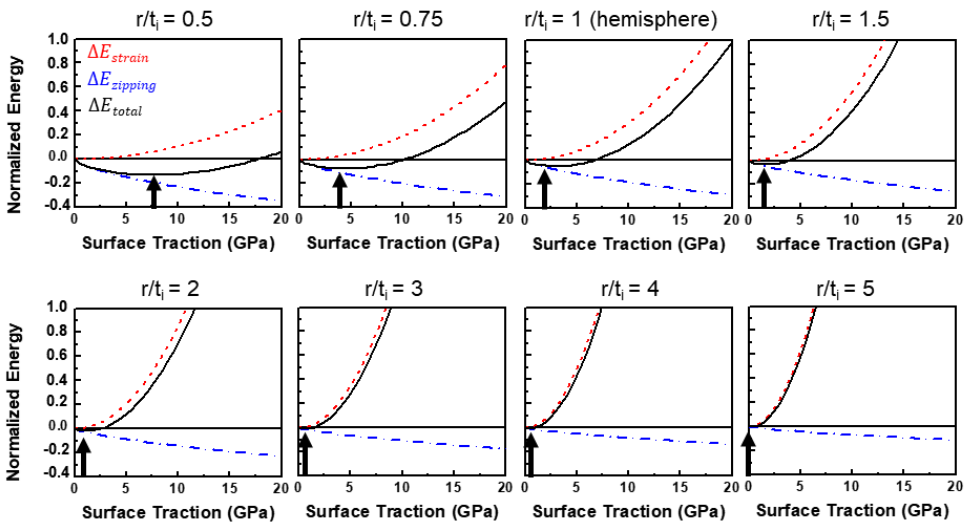

Figure 3.9 Strain energy (red) and zipping energy (blue) depending on the nucleus shape of the initial intergranular coalescence, and the lowest state of the total energy. When the value of r/t_i ratio is 5, negative energy state of total energy was not calculated.

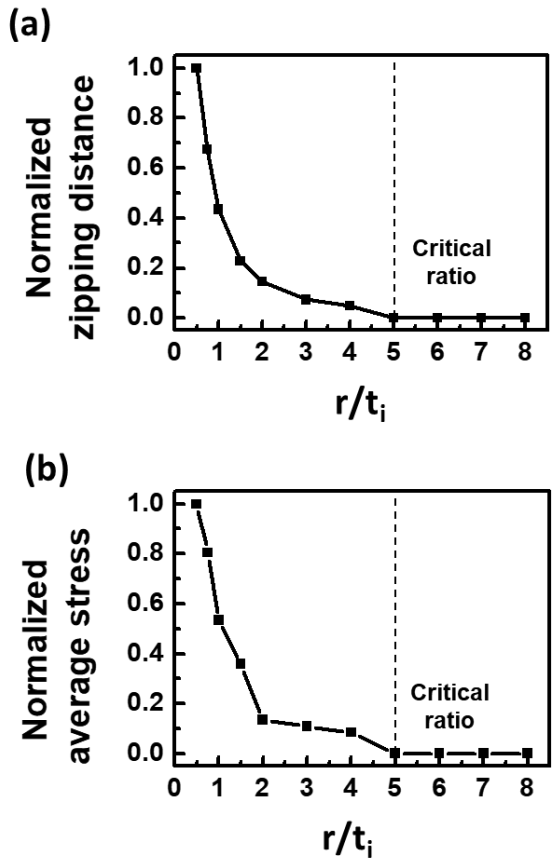

Figure 3.10 FEM simulation results of the intergranular coalescence stage. (a) Normalized zipping distance (z_0) and (b) normalized average stress when zipping occurs at the initial contact between nuclei depending on the r/t_i of the nuclei

Fig. 3.11 is a simulation result of the normalized average stress in the early growth stage depending on the value of r/t_i. Low compressive stress is generated by the surface tension of tungsten at first, and then tensile stress begins to increase rapidly through zipping after nuclei contact. Even during thickening, a large stress is continuously generated because a low r/t_i shape is advantageous for grain boundary formation through zipping deformation. However, in the case of a higher r/t_i than the critical ratio, the initial compressive stress is not compensated for and affects the distortion of the substrate or mold. It is necessary to optimize the initial deposition conditions to balance the compressive stress due to the surface tension and the tensile stress due to zipping.

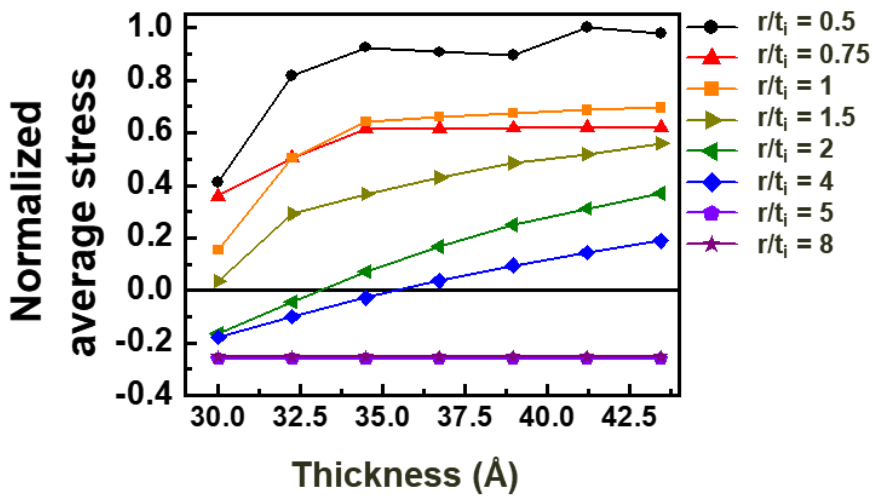

Figure 3.11 FEM simulation results of normalized average stress depending on r/t_i during film growth after contact between nuclei.

Fig. 3.12 shows the simulated normalized average stress during growth as the film thickness increases. The graphs in the figure represent the stress evolution after forming continuous films with different r/t_i values of 1.5, 2, and 4. As the thickness of the tungsten film increased, the zipping continued to generate tensile stress in the film, and the stress decreased as the r/t_i value increased. Among the three curves in Fig. 3.12, the tensile stress in the case of r/t_i value is 4 decreased at a thickness of 6 nm, where zipping during thickening stopped when the thin film formed a flattened shape. This simulation result indicates that the stress can be relaxed by suppressing the zipping or by controlling the shape of the elliptical nucleus with a high r/t_i ratio.

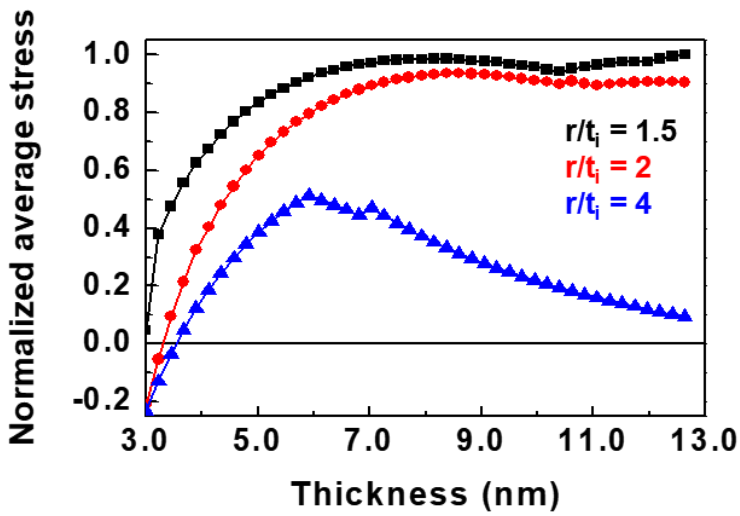

Figure 3.12 Finite element simulation result of stress evolution during growth after forming a continuous film. The graphs in the figure represent the stresses for different r/t_i values, where the initial nuclei have r/t_i values of 1.5 (black), 2 (red), and 4 (blue).

3.3.2 Trench mold bending due to film stress and interaction

Mold bending simulation was conducted to find out how the stress of tungsten film affects the vertical mold in a three-dimensional structure such as a trench. Fig. 3.13 (a) and (b) show the mold bending normalized by maximum bending after pattern closure caused by the differences in depth (case 1) and width (case 2) from the ideal mold geometry, respectively. Since the simulation model was assumed by an isotropic body, an asymmetric behavior such as bending cannot be calculated in a completely symmetric structure. Therefore, a defect in dimension that may occur in the actual process was considered in our simulation.

The two figures show that the distortion of the vertical mold represents either a gradual in Fig. 3.13 (a) or constant in Fig. 3.13 (b) increase before the tungsten film begins coalescence at the center of the trench mold where film thickness of approximately 12.5 nm. In both cases 1 and 2, the mold bending resulting from the interfilm coalescence is larger than that resulting from the intergranular coalescence. This can be explained by the fact that a larger free surface can be reduced by mold bending through interfilm coalescence.

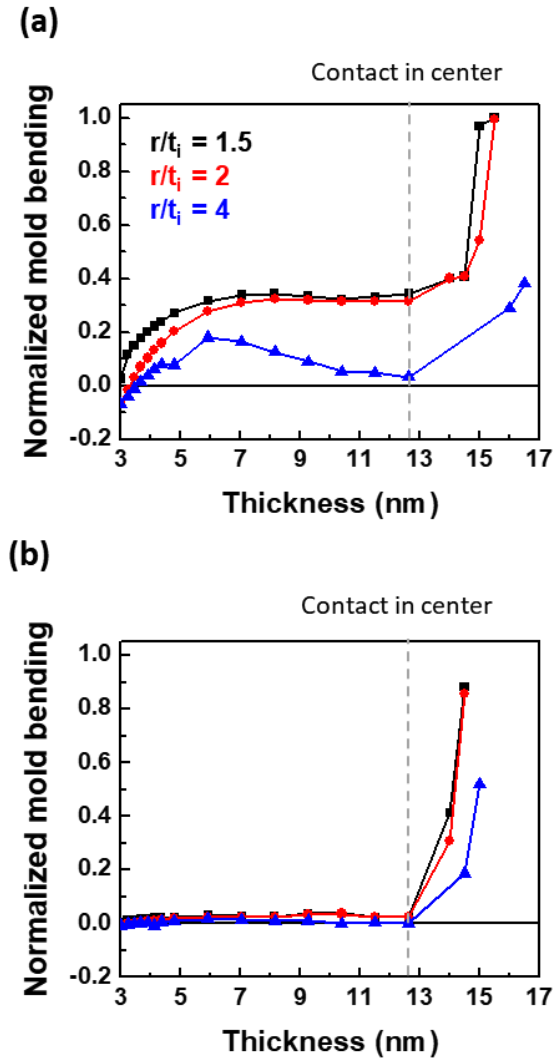

Figure 3.13 Simulation results for mold bending by the pattern defects of two cases, the results of the mold bending of an Si mold due to film stress and interfilm coalescence. An asymmetric structure was used to calculate mold bending due to patterning error or other defects: (a) 10 nm depth difference and (b) 1.5 nm width difference.

In the stage of intergranular coalescence, a different trend of mold bending was observed for the two defect patterns. When the mold has a depth difference (case 1), the mold is continuously bent as the film stress increases, while the bending of the mold with a width difference is nearly independent of the film growth. The main factor in mold bending by intergranular coalescence is the difference in the bending moment produced by the thin film stress on both walls of the mold. When there is a difference in depth in the trench mold, the areas of tungsten film covering the mold walls are different, which results in the difference in depth. Therefore, this unbalanced film growth with equivalently asymmetric stress distribution on each wall causes additional bending.

On the other hand, when two thin films contact the center of the trench by zipping, abrupt changes in the model bending occur for the case of mold width difference in Fig. 3.13 (b). When the mold is already bent, it is easier to form an additional interface, which appears to induce more mold bending.

To compare the defect effect of mold bending, the case with two asymmetry was also simulated in Fig. 3.14, which shows the mold bending assuming both depth and width difference exist. In this case, the mold bending by the depth difference becomes more dominant during film growth on the wall, but the bending by the width difference increases after the films contact the center of the mold. The each pattern defect affects mold bending independently by acting on different asymmetric behavior.

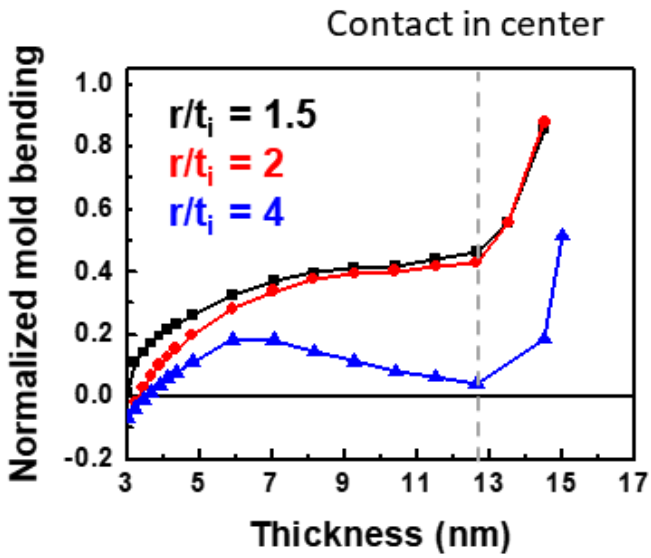

Figure 3.14 Simulation results for mold bending with the pattern defects of both 10 nm depth difference and 1.5 nm width difference.

In addition, the cross-sectional area of the metal interconnects was calculated to determine the electrical resistance in Fig. 3.15. The pattern defect with a depth difference of 10 nm and a width difference of 1.5 nm decreases the cross-sectional area of the metal line compared to a symmetric trench without a pattern defect. If there is no stress on the film and no bending of the mold, the cross-sectional area is reduced by 2.53% compared to a symmetric trench without stress. However, in the case of r/t_i value is 4, where the stress is lowest, the cross-sectional area decreases by 5.26%, and in the case of r/t_i value is 1.5, where the stress occurs the most, the cross-sectional area decreases by 6.83%. Furthermore, considering the early closing of the upper part due to overhang, the film stress affects lower cross-sectional area of trench and causes more conductivity decrease.

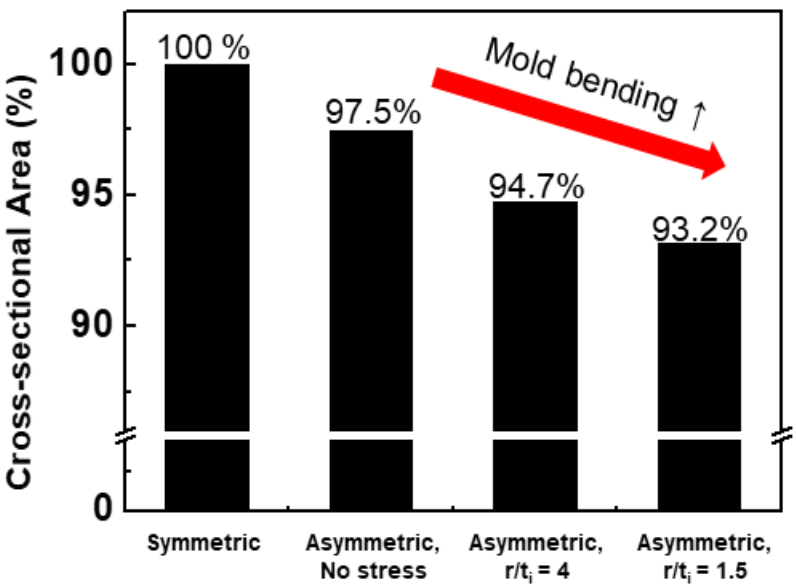

Figure 3.15 The graph of Cross-sectional area change in interconnects inside the trench according to mold bending: Symmetric is the case of no pattern defect, and asymmetric is when both 10 nm depth difference and 1.5 nm width difference exist.

3.4 Other metals case: Ruthenium and molybdenum

To provide guidelines for stress conditions when selecting metals for barrier-less metal, the simulation was conducted on initial zipping on molybdenum and ruthenium, which have the same mechanism of stress evolution as tungsten. Fig. 3.16 (a) and (b) shows the normalized zipping distance and the normalized average nuclei stress of tungsten, molybdenum, and ruthenium using our simulation method. Molybdenum has a similar Young's modulus to tungsten and lower surface energy and grain boundary than tungsten. Ruthenium has a higher Young's modulus, surface energy, and grain boundary due to hexagonal closed packed crystal structure than tungsten with body centered cubic crystal structure.

Both molybdenum and ruthenium showed the same trend of zipping distance and average stress as tungsten, and the coalescence decreased as the nucleus became wider. However, molybdenum showed a lower zipping distance and stress because the driving force of zipping decreased in molybdenum film. When the grain boundary formed due to zipping, the energy reduction of molybdenum film was smaller than that of tungsten because of its lower energy reduced by grain boundary formation. On the other hand, the driving force of zipping is higher in the ruthenium case, and the zipping distance and stress increased. Furthermore, the critical ratio of r/t_i where zipping does not occur increased from 5 to 6, confirming that wider nuclei are needed to prevent coalescence and stress in ruthenium.

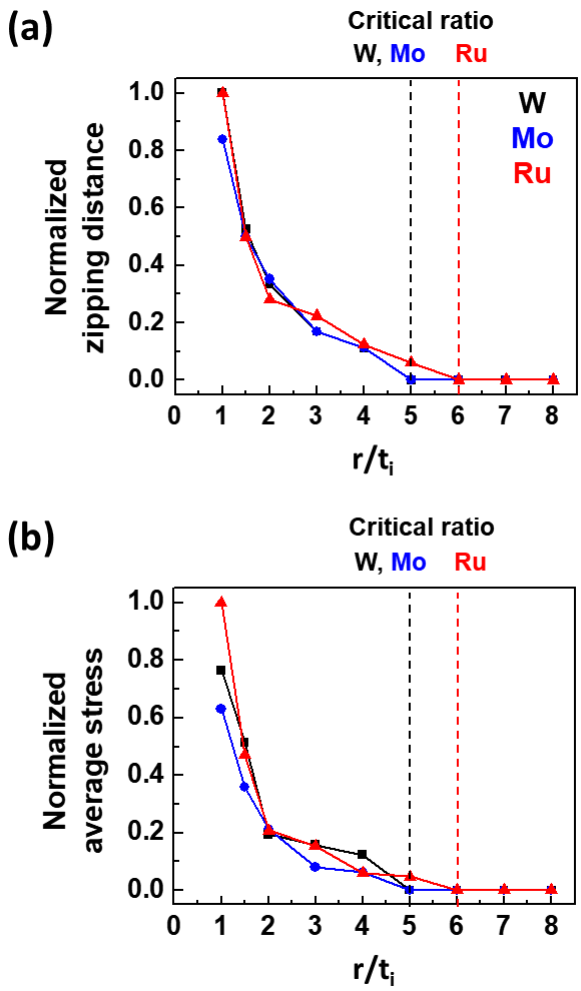

Figure 3.16 FEM simulation results of initial zipping depending on the r/t_i of the tungsten (black), molybdenum (blue), and ruthenium (red) nuclei: (a) normalized zipping distance and (b) normalized average stress.

Our stress calculation model has a limitation attributed to the assumptions made in the finite element analysis. First, using FEM simulation, the materials are all considered continuum bodies, and the interactions of the surface atoms during the zipping process are simplified as tied boundary conditions. Second, the anisotropy of the tungsten film is not considered, although crystalline solids such as tungsten have strong anisotropy at the grain scale depending on crystal strucutre. Therefore, more accurate analysis can be achieved if these simplifying assumptions are removed by introducing atomic level computations, such as density functional theory (DFT) or molecular dynamics (MD), for the calculation of coalescence behavior by interatomic interactions. Furthermore, for the stress calculation in the case of a hole-type structure such as deep via and plug, all three-dimensional zipping between the thin films growing on all sidewalls should be calculated, and a full 3D model will be needed.

3.5 Wetting effect of ruthenium film and mold bending

To prove the wetting effect on film stress experimentally, the mold bending was observed in a trench structure using ruthenium film, which is expected to generate the highest stress among refractory metals. Wetting is the effect based on interface characteristic between substrate and deposited material. Metal is the typical hydrophilic material with high surface energy and favor wetting on hydrophilic surface to form wider nuclei.

However, the metal shows dewetting like island growth because the tendency to reduce the surface of the metal itself is greater than the energy reduction by wetting. Therefore, a surface treatment was proposed to relieve the stress without an additional layer reducing the conductivity. The surface of the mold was treated to enhance hydrophilicity and hydrophobicity, and the shape of the ruthenium film growing on the substrate and the mold bending were observed.

As shown in Fig. 3.17 (a), (b), and (c), several trench molds were fabricated on Si wafer by with deep reactive ion etching (DRIE). Each trench is composed of two vertical molds, and spaced 5 mm apart from each molds to prevent interaction. Then, for surface modification as shown in Fig. 3.17 (d), UV treatment and self-assembled monolayer (SAM) material coating were performed to produce hydrophilic and hydrophobic trench molds, respectively. In the case of UV treatment, the Si molds were exposed to a UV lamp with a wavelength of 184.9 nm and 253.7 nm for 30 minutes in UVC-300 (Omniscience, Korea).

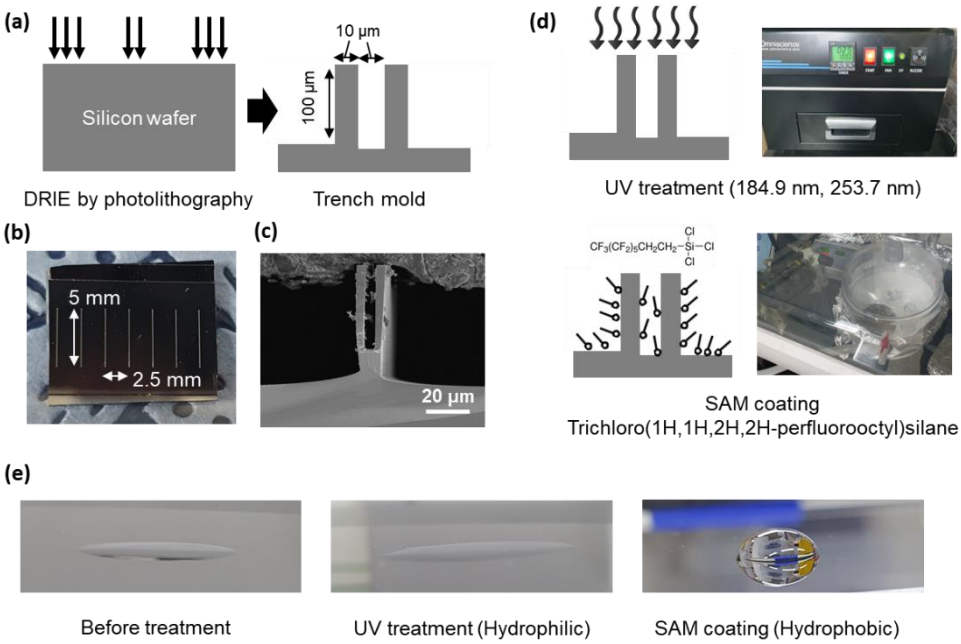

Figure 3.17 (a) Schematic of DRIE patterning and trench mold. (b) Picture of patterned Si wafer and (c) cross-sectional image by SEM of trench pattern etched by DRIE. (d) Schematic of surface treatment and equipment. (e) Wettability test of silicon wafer after surface treatment. High wetting occurs on hydrophilic silicon after UV treatment, and low wetting occurs on hydrophobic silicon after SAM coating.

In the case of SAM, trichloro (1H,1H,2H,2H-perfluorooctyl) silane material (Sigma Aldrich, Germany) was used, and hydrophobic surface was formed on the Si molds by vaporizing in vacuum chamber. A hydrophilic head with chlorine was located on the surface of the Si mold and a hydrophobic tail with fluorocarbon was exposed to the outer surface of molds.

After the mold fabrication, ruthenium was deposited inside the trench mold using DC sputtering. The ruthenium DC sputtering was conducted in room temperature, the sputtering gun power was 100 W, the inert gas (Ar) flow was 20 sccm, working pressure was 20 mTorr, and a deposition rate was 0.3 nm/s. The 5 μm thickness of ruthenium film was deposited inside, and the shape of the film and the mold was observed using an optical microscope (OM).

To observe the change in wettability of the Si wafer, the shapes of the water droplet on each surface of wafers were observed as shown in Fig. 3.17 (e). On the Si wafer without any treatment, water droplet spreads widely to the side due to intrinsic hydrophilicity of single crystal silicon. After UV treatment, water droplet spreads more widely than the untreated state difficult to distinguish the droplet boundary, and it is possible to form nuclei with high r/t_i value of ruthenium due to improved wettability. On the other hand, after SAM coating, the convex droplet was maintained due to repulsive force due to hydrophobicity. Similarly, in metals such as ruthenium, it is also possible to form nuclei with low r/t_i value due to repulsive force on interface.

Fig. 3.18 is the image of trench top surface before and after 5 μm ruthenium deposition to find wetting effect on mold bending of the hydrophilic mold and hydrophobic mold. In the case of the trench before deposition, both the molds were formed straight without mold bending after surface treatment. In the case of the ruthenium deposited on the hydrophilic mold, flat film was formed on both sides of the molds. Therefore, ruthenium nuclei were formed in a wide shape that did not induce stress, because good wetting occurred on hydrophilic surface. Thus no mold bending was observed in the hydrophilic mold exposed to UV.

However, in the hydrophobic mold, excessive agglomeration in ruthenium film occurred, and high dewetting shape was observed. As a result, mold bending, in which the edge of the mold was bent, was observed. This mold bending was observed despite the very thick mold with 10 μm thickness, thus a larger bending can appear in M1 level interconnects being developed as sub-10 nm thickness. Based on these results, the surface parameter of the mold surface is a key point for suppressing stress, and it is necessary to improve wetting by increasing the surface energy and hydrophilicity of the mold material.

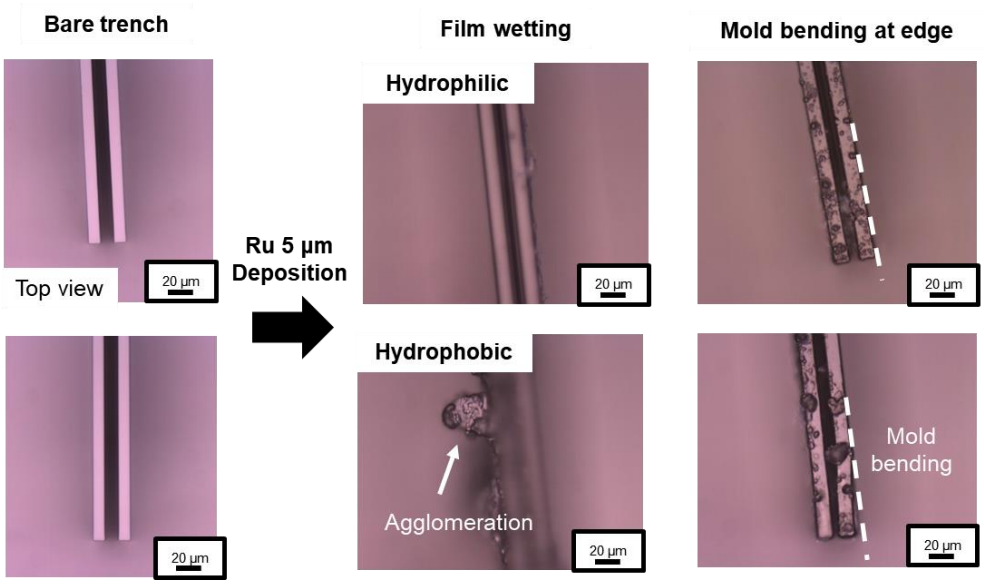

Figure 3.18 Image of ruthenium film and trench mold before and after 5 μm ruthenium deposition by OM. Film wetting on Si mold and mold bending of trench were observed. Severe agglomeration and mold bending occurs on hydrophobic surface coated by SAM.

3.6 Summary

As the pitch of the interconnects pattern decreases due to the shrinkage of the integration system, research on refractory metal such as tungsten is conducted, which has characteristics of good gap fill and barrier-less. However, tungsten exhibits higher stress than conventional interconnection metals when it is used as a gap filler by chemical vapor deposition. High deposition stress by zipping results in severe distortion of the thin vertical mold, which is designed to fabricate interconnects with fine pitch. Our study based on the shape optimization of tungsten nuclei through finite element simulation proposes elliptical nucleation with high width, which is intended to relax the zipping stress during growth on the trench mold. In the simulation, two sources of vertical mold distortion were investigated: Intergranular coalescence and interfilm coalescence. The results show that the tungsten film with low zipping stress induced by introducing an elliptical nuclei shape can be effectively suppress the distortion of the mold. For next-generation interconnect metals, such as Ru and Mo, which have similar zipping mechanisms to tungsten, high deposition stress will cause pattern distortion issues. Therefore, the stress analysis model proposed in this study can be extended to provide guidelines to predict and reduce deposition stress in fine patterns by metallization.

CHAPTER 4

Strain Analysis of Twisting Modes in Wearable Devices

(Published, *Advanced Electronic Materials*, 2020 [68])

4.1 Introduction

Along with the development of multi-platform devices such as IoT, the form factor of electronic products is diversifying. Especially, electronic devices are changing in a direction that is more closely to human surface, and electronic platforms is greatly increasing toward flexible electronics that achieve high portability, low weight, and mechanical robustness against mechanical impact. Those flexible electronics will be operated with accompanying repeated mechanical deformations, such as bending,

rolling, and twisting that can occur from human body motion. Wearable and attachable devices that are in close contact with physical activity are more frequently and severely exposed to these mechanical deformations [32]. As such mechanical deformations fatally result in mechanical stress on electronics devices, the mechanical reliability of flexible electronics during repeated mechanical motions has become a very important issue.

In particular, the interconnects in flexible devices need more robust to mechanical stress, compared with small active parts, such as the transistor or sensor. For example, during bending deformations, a small Si chip may escape high mechanical stress evolution, because Si has high strength, and the size of the Si chip is relatively small. However, interconnects distributed on a flexible substrate must be able to withstand mechanical deformation. The development of a highly reliable electrode and interconnect is a key to achieve long-term reliability of flexible electronics.

To improve the mechanical reliability of the interconnect, material and structural solution, such as metal nanowire, conductive gel, serpentine electrode, and nanohole electrode have been demonstrated. However, these materials are also suffered by reliability problems due to inevitable stress and strain during deformation.

Therefore, mechanical stress control is the key to achieve further reliable interconnection platform. For example, the stress evolution during simple bending deformation is firmly established: tensile and compressive stress are caused at the outside and inside of the bending shape, respectively [69-71]. The stress-free plane between the tensile region and compressive region in the bending shape is called the

neutral plane [72-74]. By placing flexible electronics on the neutral plane, the stress can be reduced, or by matching the materials property or thickness of substrate and cover layer, the stress can also be controlled [46], [75]. The stress-free zone concept by distributed stress is actively adopted for the design of highly reliable flexible electronics.

However, the real operation of flexible devices includes much more complex deformation, such as twisting. The stress-free zone concept cannot be applied for twisting deformation because stress distribution of twisting is still unclear under various conditions. In the case of twisting, various modes may occur due to the complexity of the three-dimensional deformation, which makes it difficult to predict the stress generated in the planar device.

As shown in Fig 4.1, various modes of twisting deformation were simplified as two cases of twisting, and the distribution of stress and strain was analyzed according to those two twisting cases for providing design rules for flexible device: fixed twisting, and free twisting. For fixed twisting, in which the sample length did not change during twisting motion, the patterns at the center area near the twisting axis showed high stability. In contrast, for free twisting, in which the sample length is shortened during twisting motion, the patterns at the edge area exhibited superior reliability.

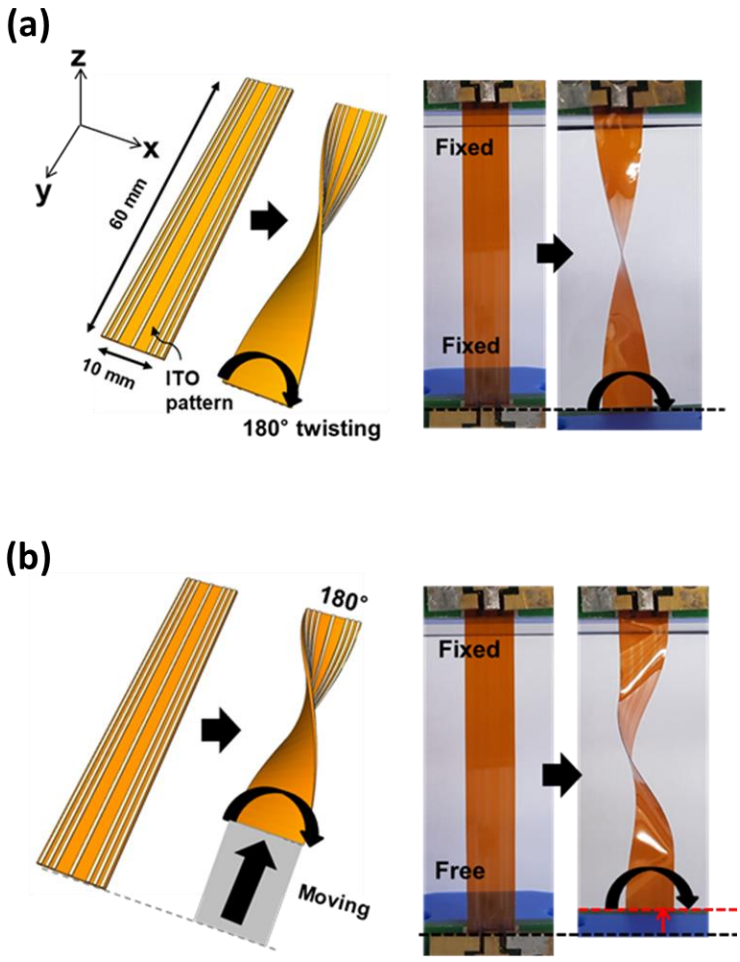

Figure 4.1 Schematics and images of the flexible electrode in twisting motion. (a) Fixed twisting, in which during twisting motion, the sample length is fixed. (b) Free twisting, in which during twisting motion, the sample length is shortened.

To observe changes in reliability due to stress on the surface, the fatigue behavior depending on materials and position were analyzed by observing the failure morphologies. The stress-free zone in twisting deformation was suggested by conducting FEM simulation. Twisting model attached to base also progressed to clarify the effect of the base where the device is located. Finally, the stress-free zone was also verified by conducting real twisting tests, such as the twisting motion of the human body. Based on our experimental and simulation results, stress-free zone exists in twisting deformation, and it depends on the twisting mode and the properties of the base materials where the device is attached. This study based on experimental reliability test and computational simulation will be very helpful for developing highly reliable future electronics that are twistable.

4.2 Experimental and simulation procedure

Indium tin oxide (ITO) with a thickness of 200 nm was deposited on a polyimide (PI) substrate (Dupont, Kapton) with a thickness of 125 μm by RF sputtering (13.56 MHz frequency) using Ar gas as sputtering gas. The composition of ITO was consisted of 90 wt%: 10 wt% of In_2O_3: SnO_2 and a deposition rate was 3.75 nm/min. Copper interconnects pattern with a thickness of 1 μm was deposited by thermal evaporation process with a deposition rate of 0.8 nm/s. Line patterns of 200 μm width and 60 mm length were formed through a shadow mask during the deposition process. Flexible electrode specimens were a rectangular shape with a width of 10 mm and a length of 60 mm for the twisting test. The line patterns were located at the center of the specimen (0 mm) and the positions of other patterns are (2.5, 3.5, and 4.5) mm from the center of the specimen. The centerline of pattern was adjusted to the rotation axis.

The twisting test was conducted by twisting system (CKSI, Korea). Two kinds of twisting motion were tested: fixed twisting, and free twisting. For the fixed twisting test, both metal grips of the sample were fixed at the ends to keep the distance between the sample grips constant as shown in Fig. 4.1 (a). For free twisting, one edge of the sample grip could be freely moved, so that during twisting motion, the sample length was shortened as shown in Fig. 4.1 (b). Twisted deformation was applied by counterclockwise direction from 0° to 180° with a twisting rate of 10°/min. Both ends of the specimen were held by conducting metal grips to measure the electrical resistance during twisting in real time. By placing metal contact at each

pattern separately, the electrical resistance of the pattern with different locations could be measured at the same time. The electrical resistance of the flexible electrode was measured by switching system and resistance measurement system (Keithley 2700). The electrical resistance of ITO patterns was measured every 5° of twisting deformation as the stress indicator of flexible substrate. For the fatigue test, copper line pattern were used, and repeated twisting deformations with a twist angle of ± 180° was applied on the flexible sample. The frequency was 0.5 Hz, and the maximum cycle was 15,000 cycles. For free twisting fatigue, the shortened sample should be recovered to the initial shape, so that a weight of 100 g was installed on removing the grip. After the twisting test, the samples were observed by FESEM (MYRA3 XMH, TESCAN).

To analyze the strain on the substrate surface, FEM simulation was calculated by commercial FEM software, ABAQUS (Dassault Systemes, France). The PI substrate model was designed on the same dimension with the experimental sample size. Each element was C3D8 element type in 3D stress condition, which was used for linear cubic element. The mechanical properties for elastic simulation, Young's modulus and Poisson's ratio of the PI substrate for calculation were in Table 4.1 [76-79]. For the fixed twisting simulation, both ends were placed on their initial positions, and one end was rotated by 180°. For free twisting simulation, one end was fixed at the initial position and rotated 180°, while the other end was moved toward the end of the rotation by as much as the 4 mm deformation of the actual sample. To analyze

the strain of the conductive pattern, the true strain of the surface where the pattern is located was calculated.

In addition, to analyze the twisting motion depending on the base where the sample was placed, the base model having 20 mm width, 90 mm length, and a thickness of 1 mm was designed to be relatively larger than the sample. Mechanical properties of the five materials, skin, PDMS, leather, PI, and Kevlar, were applied to the base in elastic condition. The Young's modulus of base materials in Table 4.1 [76–79]. The base was twisted 270° to induce 180° rotation of the sample, and both ends of the base were fixed for making fixed twisting motion.

	Elastic modulus (GPa)	Poisson's ratio
PI (substrate)	2.5	0.34
Skin	5×10^{-5}	0.49
PDMS	2×10^{-3}	0.49
Leather	0.1	0.49
Kevlar	70.5	0.36

Table. 4.1 The mechanical properties of substate and base materials [76-79].

4.3 Fixed/Free twisting test with *in-situ* resistance monitoring

To observe the difference in strain distribution according to the twisting mode, two kinds of twisting tests were conducted: fixed twisting test, and free twisting test. For fixed twisting test, the distance of both edges of sample was fixed, so the distance of both ends did not change during the twisting motion as shown in Fig. 4.1 (a). For free twisting test, which is suggested by the international standardization of flexible display and printed electronics [80], [81], one edge of the sample can be linearly moved according to twisting motion, so the distance of both ends can be shortened during twisting motion as shown in Fig. 4.1 (b).

Fig. 4.2 (a) shows the electrical resistance change of ITO patterns having different positions as the twisting angle during the fixed twisting test. Each experiment was conducted with more than three sample. The initial resistance of the ITO pattern with a position of x = 0, 2.5, 3.5, and 4.5 mm was 11.32, 15.66, 14.93, and 12.84 Ω, respectively. The electrical resistances of all lines did not change until 130°. However, the electrical resistance of the pattern at 4.5 mm started to increase first at the twisting deformation of 130° and increased up to 500 times. The ITO patterns at 3.5 and 2.5 mm also showed electrical resistance increase sequentially less than pattern at 4.5 mm. Only the ITO pattern positioned at the centerline kept its initial resistance after 180° twisting.

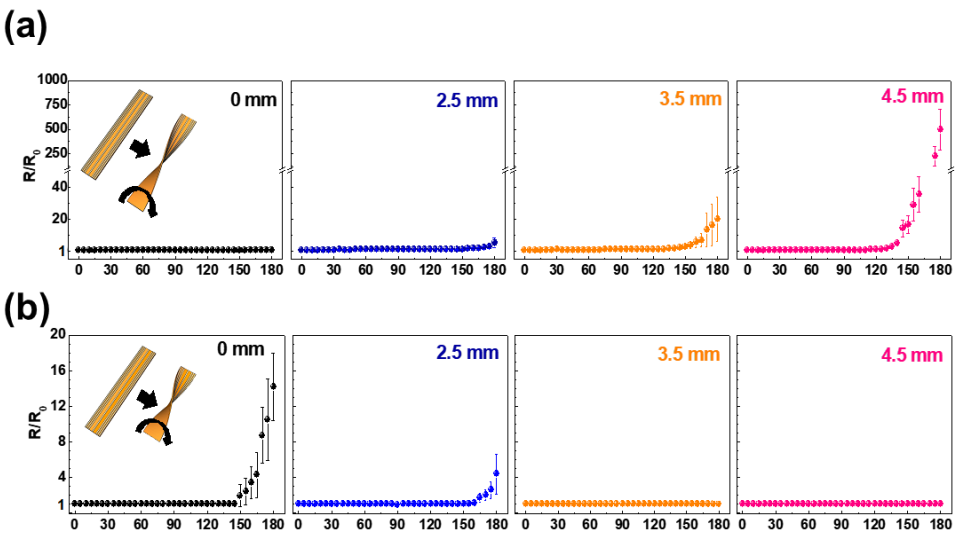

Figure 4.2 Electrical resistance change of ITO pattern depending on twist angle (a) in the fixed twisting test and (b) in the free twisting test.

Fig. 4.2 (b) is a graph showing the change in electrical resistance as a function of the twisting angle during free twisting, in which one end of the sample is free to move in the length direction. All patterns kept their initial electrical resistance up to 180° twisting. However, contrary to the results of fixed twisting, the pattern at the center where x is 0 mm showed significant electrical resistance up to 15 times after 180° twisting. Interestingly, the patterns at the edge area exhibited low resistance change.

To quantify the twisting stability, the failure angle (θ_f) was defined by the twisting angle at which the electrical resistance increases to 2 times. The failure angle was plotted as a function of the ITO pattern position during fixed and free twisting in Fig 4.3. For fixed twisting, the center ITO line showed superior stability, but the patterns at the edge area showed poor mechanical stability. However, for free twisting test, the centerline showed the lowest failure angle compared to the other lines and edge area showed high failure angle.

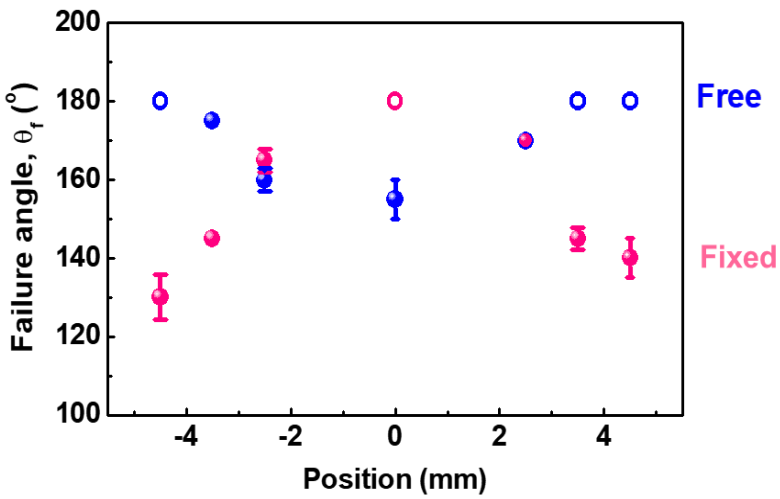

Figure 4.3 The failure angle of ITO pattern according to the position in the fixed and free twisting test. The failure angle is defined by the twist angle when the electrical resistance increases by two times.

To investigate the origin of electrical resistance, the surfaces of ITO patterns after two twisting tests were observed by FESEM. Fig. 4.4 and Fig 4.5 show FESEM images of ITO patterns positioned at 0, 2.5, 3.5, and 4.5 mm in the sample width direction (x direction) after fixed and free twisting test. The FE-SEM images were taken at 10 mm intervals on the y-axis. After fixed twisting test in Fig 4.4, numerous cracks were observed at the edge area which is indicated by red box, but no crack was observed in the center area which is indicated by green box. As a result, consistent with the experimental results, more cracks are observed on the surface of the line with increased resistance.

On the other hand, after free twisting test in Fig. 4.5, no crack was observed in the patterns at the edge area which is indicated by green box, but a great number of cracks were observed in the center pattern which is indicated by red box after the free twisting test. Unlike the general uniaxial tension or bending, the direction of cracks is different with the longitudinal position of the sample. This implies that the stress evolution during twisting motion strongly depends on the twisting mode.

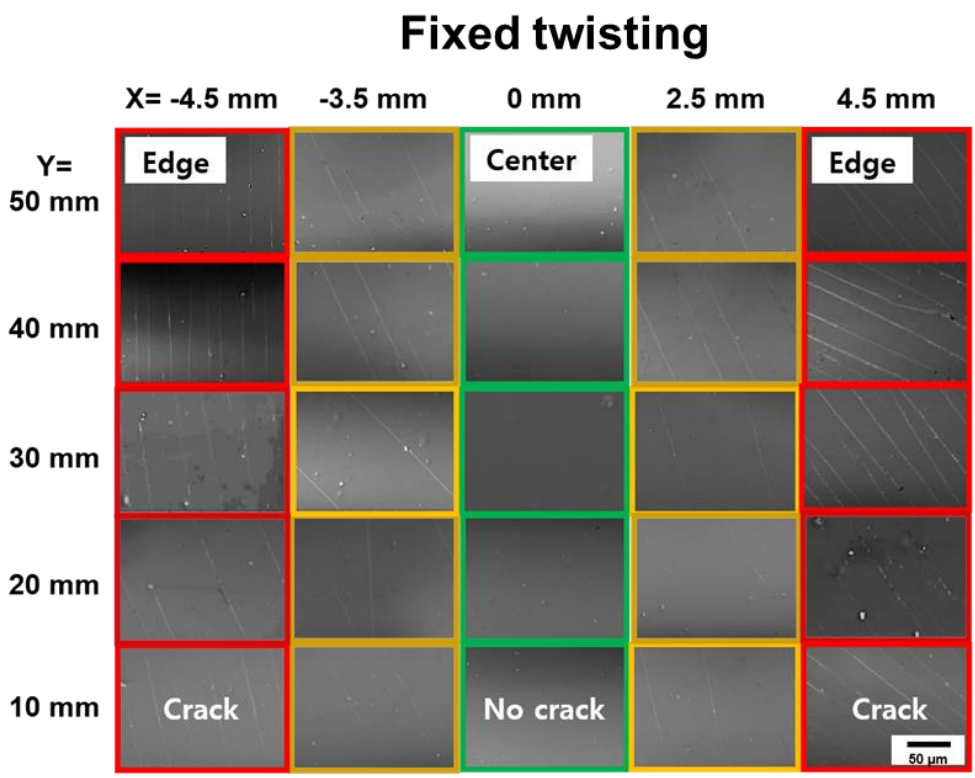

Figure 4.4 SEM images of ITO patterns at different positions after fixed twisting test. The position of x is a distance from rotation axis and y is the longitudinal position of ITO line from grip to grip.

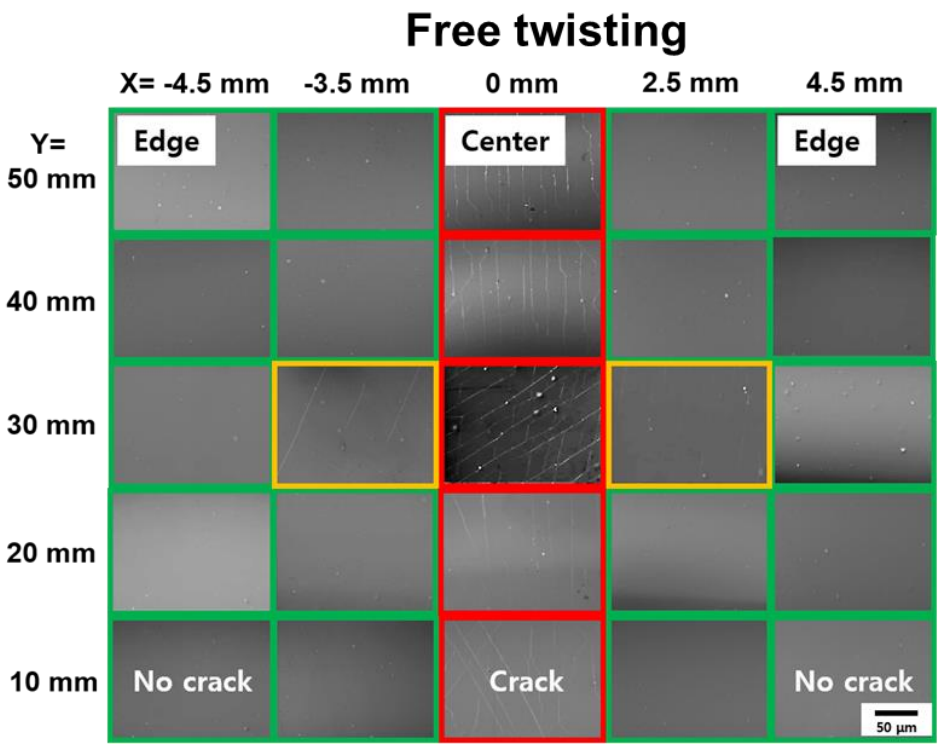

Figure 4.5 SEM images of ITO patterns at different positions after free twisting test.

In addition, a fatigue test due to repeated deformation was also conducted through a deformation test of a ductile metal thin film such as copper. Since the copper interconnect is a more ductile material compared to the brittle ITO electrode, the Cu patterns in all positions, including edge and center area, showed no electrical resistance change until 180° twisting deformation at 1st cycle unlike the ITO pattern. Thus, the twisting fatigue test that applied repeated twisting and unwinding motion in the sample was conducted. The initial resistances of the Cu patterns positioned at x = 0, 2.5, 3.5, and 4.5 mm are 9.24, 10.4, 9.87, and 11.02 Ω, respectively.

Fig. 4.6 (a) shows the electrical resistance change of Cu lines as a function of fixed twisting cycles. While the Cu pattern at the centerline kept its initial resistance until 15,000 cycles, the pattern at the edge line where x is 4.5 mm showed abrupt failure after just a few cycles, and the pattern at the 3.5 mm position showed electrical resistance increase by about 60 times after 15,000 cycles. Fig. 4.6 (b) shows the change in electrical resistance of the Cu pattern in the free twisting test. In the first cycle, the resistance of all patterns did not change, but in repeated fatigue test, the electrical resistance increased, especially in the centerline.

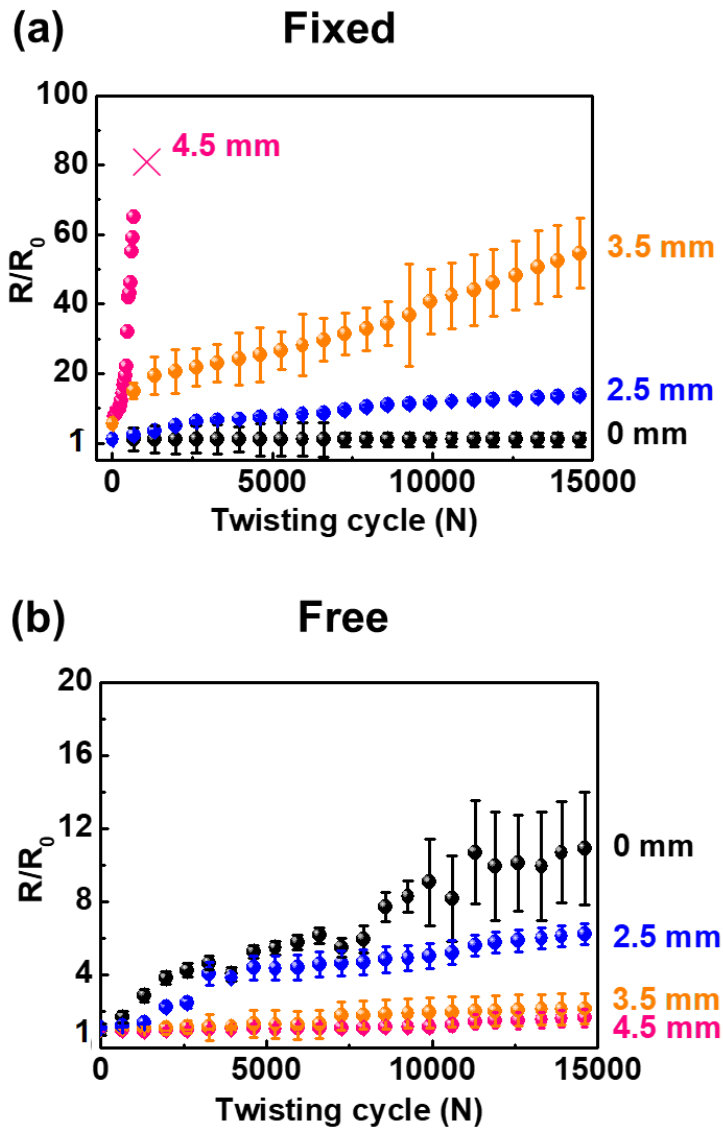

Figure 4.6 Electrical resistance change of Cu pattern in (a) the fixed twisting fatigue test and (b) the free twisting fatigue test.

The surface morphologies of the Cu pattern at different positions are shown in Fig. 4.7. In the fixed twisting test, no crack was detected in the centerline, but many cracks were observed in the pattern at the 4.5 mm position. On the other hand, after free twisting fatigue, numerous cracks were observed in the center pattern, but no crack was detected in the edge pattern, which is the opposite trend compared to the fixed twisting results.

During the twisting test, cracks were immediately formed in the ITO pattern, as shown in Fig. 4.4 and 4.5. However, in the Cu pattern, cracks were formed after certain cycles, as shown in Figs. 4.7. The origins of these cracks are different between oxide and metal, because ITO is inherently brittle material and copper is ductile material. In the oxide material such as ITO, large deformation beyond rupture strain causes immediate cracking, rather than plastic deformation. On the other hand, in case of copper, plastic deformation occurs and dislocation moves into slip plane during cyclic deformation, and fatigue damage such as extrusion and intrusion is generated on film surface.

In the fracture caused by twisting deformation on ITO, a noteworthy point is the surface morphology of cracks at the position where the stress is concentrated according to two twisting modes in Fig 4.8. In the case of cracks caused by fixed twisting deformation, the brittle cracking of ITO patterns shows that cracks occurred in a form in an open crack by tensile stress in Fig 4.8 (a). On the other hand, in the case of cracks caused by free twisting deformation, cracks appeared in a form in closed crack extruded due to compressive stress in Fig. 4.8 (b).

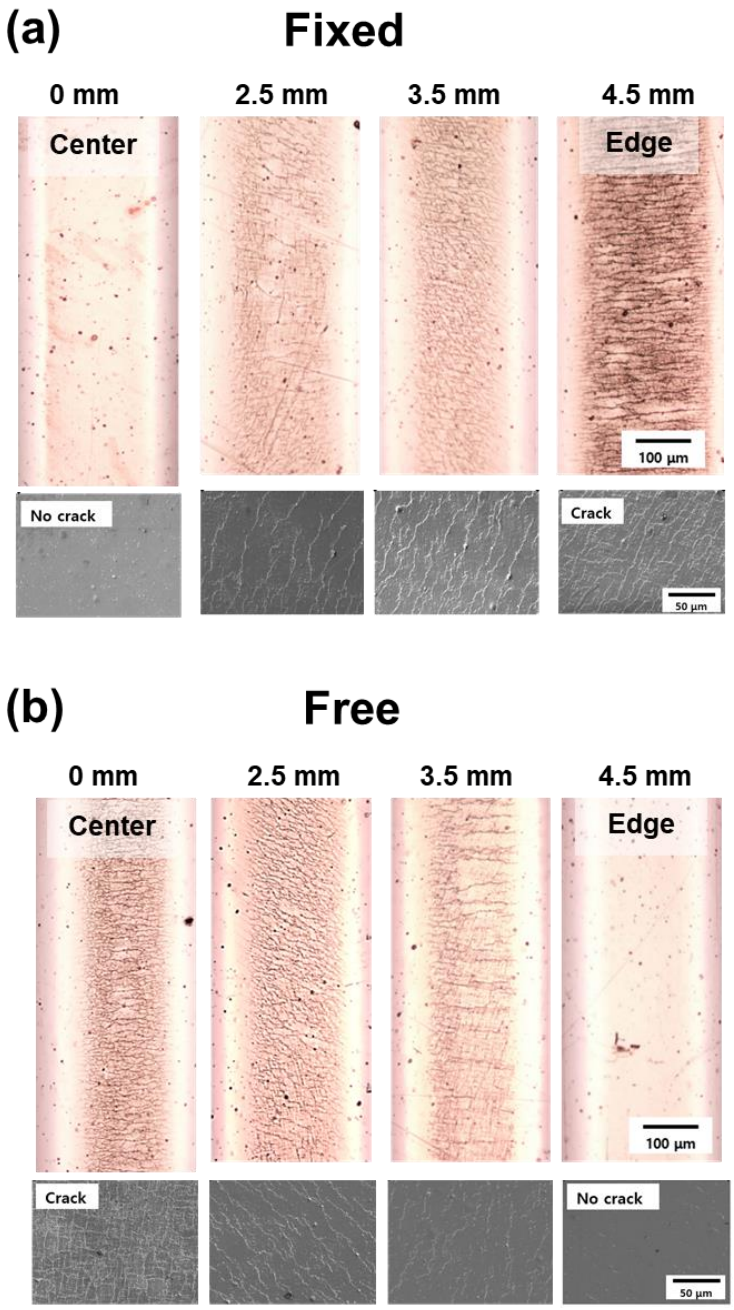

Figure 4.7 Optical and SEM images of Cu patterns at different positions after 15,000 cycles of (a) the fixed twisting test and (b) free twisting test.

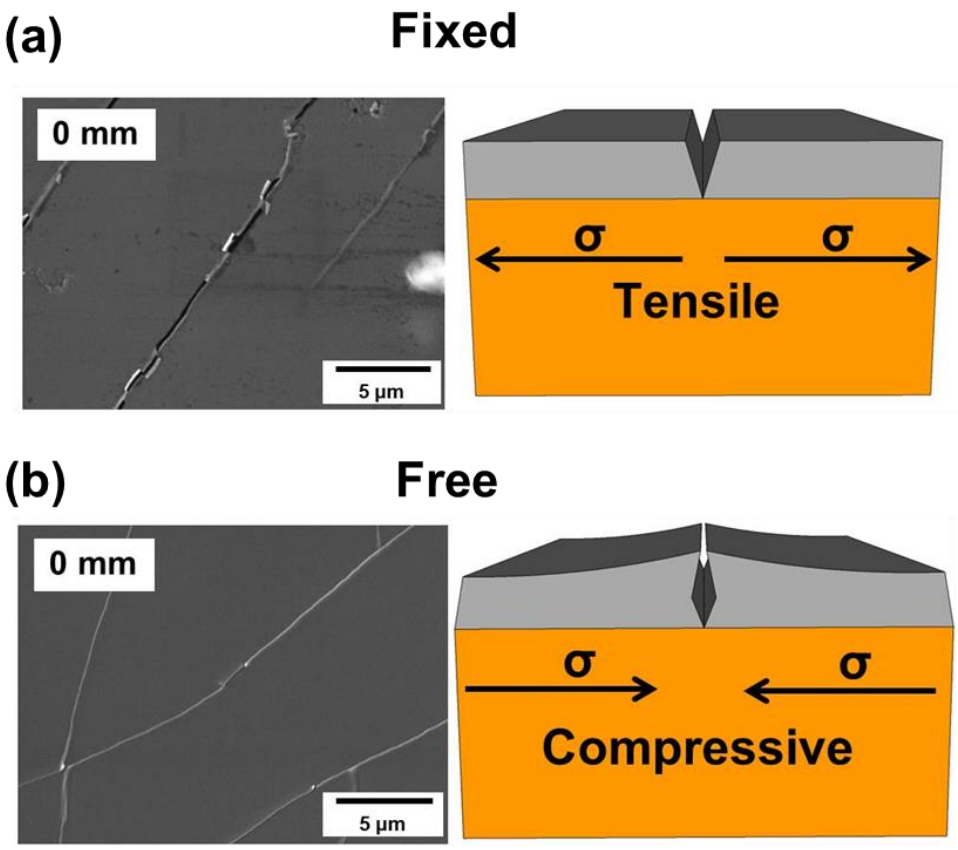

Figure 4.8 (a) Brittle fracture of ITO pattern in edge area caused by tensile stress evolution during fixed twisting. (b) Closed crack of ITO pattern in center area caused by compressive stress evolution during free twisting.

4.4 Strain analysis by FEM simulation

4.4.1 Fixed/Free twisting condition in free standing condition

Based on experimental results, the mechanical reliability of flexible electrodes significantly changes on the position of patterns and the twisting mode interestingly. In the fixed twisting test, patterns in the center area showed high stability; however, in the free twisting test, the patterns in the edge area showed high reliability in the experiments from Fig. 4.3 to Fig. 4.7. In order to elucidate the stress evolution in each twisting test, strain analysis by FEM was conducted. Fig. 4.9 shows the FEM model for fixed twisting and free twisting. To represent the free twisting, the change of sample length according to twisting angle was measured, and the length change in the y-direction was applied in the FEM model. In experiments, when the PI substrate with 10 mm width and 60 mm length was rotated 180°, the 4 mm distance reduction between both ends was occurred on free twisting test mode, and this reduction was applied in simulation model as a boundary condition. The simulation model mimics the twisting motion of the flexible electrode and visualizes the von Mises stress on the surface.

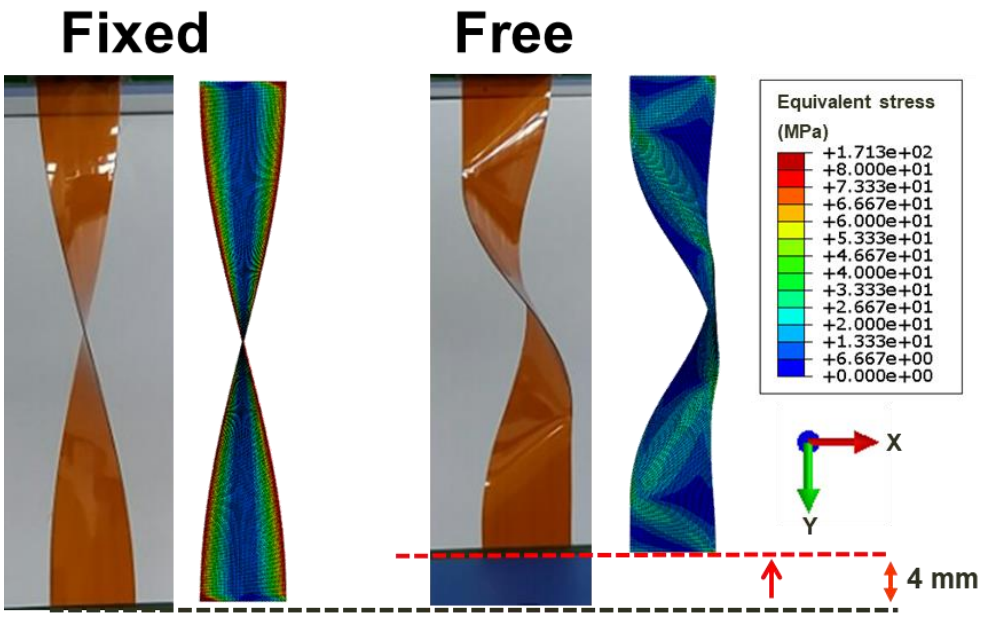

Figure 4.9 Real twisting deformation and FEM simulations with von Mises stress distribution of flexible electrode during fixed and free twisting motions.

In the case of the fixed twisting model, uniform stress occurs on the model surface along the y-axis, the longitudinal direction of the model, depending on the distance from the rotation axis at the center. On the other case of the free twisting model, the outer edge of the model was screwed inwardly and released the stretch, and the stress occurs across the surface of the model in a zigzag direction similar to buckling. In the case of free twisting, various stress distribution was observed depending on the y position. Buckling-like local folding shape appeared, and some smaller cracks were found on ITO surface at the positions on where 1) x is -3.5 mm, y is 30 mm and 2) x is 2.5 mm, y is 30 mm condition under free twisting in Fig. 4.5. This local folding in free twisting can be confirmed by the sample dimension such as length, width, and thickness. In general, more cracks were observed in the center axis under free twisting because the strain of the conductive pattern is governed by the strain on the substrate surface due to the thickness of the substrate is much thicker than the conductive pattern.

Fig. 4.10 shows the strain components across the x-axis direction on the central surface of longitudinal middle position of substrate. In the model with two boundary conditions, the surface on which the axis of rotation is located is defined as the where X position is 0 mm, and the 3D strain components were analyzed from 0 to 4.5 mm on both sides.

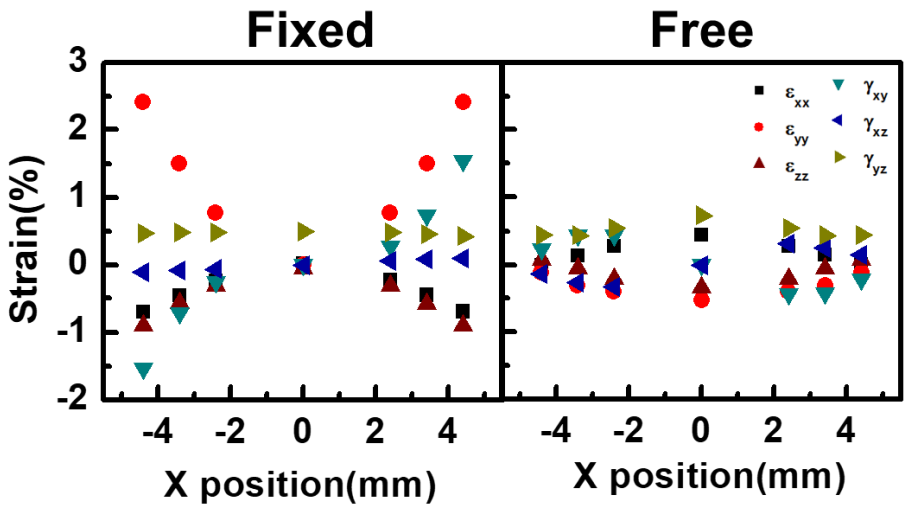

Figure 4.10 Strain component of FEM results of flexible electrode during fixed and free twisting motions.

In the case of the fixed distance of Fig. 4.10, the magnitude of the strain components increased with the distance from the rotation axis except for γ_{xy} and γ_{yz}, and in particular, the strain in the longitudinal direction which indicated by red circle increased to 2.5%. In the case of the free twisting, the magnitude of strain components decreased with distance from the axis of rotation except for γ_{xy} and γ_{xz}, the highest strain occurred on the axis of rotation, and all strain component showed less than 1%.

The most important factor affecting the mechanical reliability of the conductive pattern with narrow line shape is the normal strain occurring in the longitudinal direction through the line. When the mechanical load is applied to the material, the conduction path breaks, due to the mechanical crack perpendicular to the load direction. The longitudinal strain distribution on substrate, which was indicated by red circles, depended on the two boundary conditions of twisting, and the cause of the fracture and the position dependence of mechanical reliability occurred oppositely.

The normal strain ε_{yy} in Fig. 4.10 represents the strain in the longitudinal direction of the line pattern. In the case of fixed twisting mode, stretch occurred on the outer edge of the sheet due to both ends maintaining their distance. However, in the case of free twisting mode with a loose boundary condition, such as a soft surface, the strain of the outer edge was released, and compressive deformation occurred at the center, and buckling of substrate occurred to release compressive stress to out-of-plane, due to the decrease of the distance of both ends. Therefore, the longitudinal

strain, ε_{yy} component had a positive value for fixed twisting, and a negative sign for free twisting. In addition, the ε_{yy} distribution matched the experimental results, which showed that fixed twisting had higher strain on the edge, and free twisting had higher strain on the center.

In FEM simulation, in fixed twisting, tensile stress is detected in the edge of Fig. 4.10. This tensile stress is related to the elongation of sample in the y-direction, the longitudinal direction. However, in free twisting, compressive stress was observed, due to compression of the center area during the buckled shape deformation in free twisting. These stress analyses matches with the crack morphologies of ITO, as shown in Fig. 4.8. After fixed twisting, open cracks were observed in edge ITO patterns as shown in Fig. 4.8, which are normally induced by tensile stress; but after free twisting, extruded close cracks were observed in the center, which were caused by compressive stress. Based on the above experiments, longitudinal normal strain, ε_{yy} is a major factor for making mechanical failure. Similar to a typical bending, cracks occurred in the same direction, perpendicular to the bending direction. However, in this twisting experiment, the direction of crack was different according to x and y position, and the stress-free zone changes according to the mode.

To find representative value of multiaxial strain, an equivalent strain was calculated for integrating the components and quantifying the strain under complex deformation in Fig. 4.11. The equivalent strain was calculated by Eq. 19, von Mises strain, using the strain component value in Fig. 4.10 [47].

$$\varepsilon_{equivalent} = \frac{1}{\sqrt{2}(1+v)}\sqrt{(\varepsilon_{xx}-\varepsilon_{yy})^2+(\varepsilon_{yy}-\varepsilon_{zz})^2+(\varepsilon_{zz}-\varepsilon_{xx})^2+\frac{3}{2}({\varepsilon_{xy}}^2+{\varepsilon_{yz}}^2+{\varepsilon_{xz}}^2)}$$

(Eq. 19)

The equivalent strain of fixed twisting rose as the distance from the rotation axis increased; in the other case, the equivalent strain of free twisting reduced as the distance from the rotation axis increased. For example, the equivalent strains of the 2.5 mm position of fixed twisting and the 0 mm position of free twisting were 0.85% and 0.81%, respectively. The failure angle of ITO is similar to 160°, and the resistance of copper line increased ten times when the 15,000 times repeated deformation was applied. When the equivalent strain increased due to the distance from the rotation axis, the resistance changes also increased like experimental results in Fig. 4.2 and Fig. 4.6.

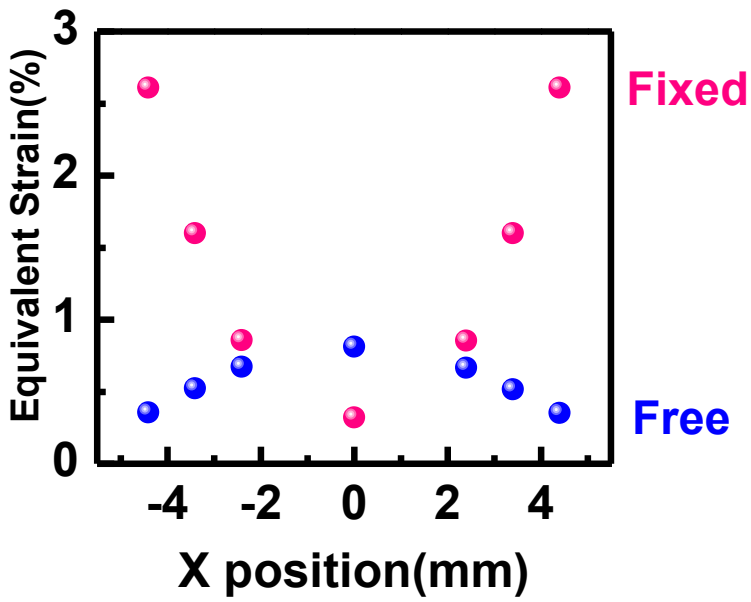

Figure 4.11 Equivalent strain of FEM results of flexible electrode during fixed and free twisting motions.

The quantified mechanical reliability can be predicted by the equivalent strain, which can be calculated by the numerical simulation tool, even in the case of complex deformation with various boundary conditions such as heterogeneous integration. The adhesion between metal layer and polymer substrate is also important factor for mechanical reliability. The interfacial adhesion can be strengthened by adding adhesion layer, surface treatment, or post treatment [82], [83]. It is expected that better adhesion between the substrate and the metal material can improve the fatigue lifetime of electronic device. However, the tendency of stress evolution and related fatigue lifetime would be still identical with the strain distribution.

4.4.2 Fixed/Free twisting condition on soft surface

As discussed above, the twisted shape of flexible substrate depends on twisting mode defined, so the twisting mode is an important factor to identify the stress distribution. To define whether twisting modes occur differently in actual twisting, the twisting cases were calculated how much affected by twisting of base material with various modulus, where the PI substrates is attached. When the samples are twisted tightly or attached onto stiff materials, such as Kevlar used in body armor, the stress evolution would be similar to the fixed twisting test, as discussed in Fig. 4.1. If the samples are twisted loosely or attached onto soft materials, the sample has some freedom to change its length and shape, so the results would be similar to that in free twisting. Since stress-free zone changes depending on the boundary conditions, mechanical properties of the base materials on which the devices are attached are important factors that affect the boundary conditions of the device.

Fig. 4.12 (a) shows schematic of FEM simulation model designed to identify the effect of base under twisting. The device of PI was placed to the base larger than the device, and the base was rotated by fixed twisting method. Fig. 4.12 (b) shows that the longitudinal strain generated on the device surface according to the five base materials which had mechanical properties of skin, polydimethylsiloxane (PDMS), leather, PI, and Kevlar. Young's modulus is lowest in skin and increases in order of PDMS, leather, PI, Kevlar. These skin, PDMS and leather have lower Young's modulus than PI, and Kevlar has higher Young's modulus than PI. In Fig. 4.12 (b), when the base became harder as the Young's modulus of base increases, the twisting

angle of the sample became larger, and the longitudinal strain of sample increased. Moreover, when the base material was soft, compressive strain was generated at the center of the rotation axis like free twisting.

Fig. 4.13 (a) and (b) show longitudinal strain and equivalent strain of the device attached to various base materials along the rotation axis, respectively. Both the higher longitudinal strain and equivalent strain generated on the surface of the PI device increased as the base became harder. Especially, longitudinal strain in Fig. 4.13 (a) shows different change in the center and the edge depending on mechanical relationship between the base material and device. When the base material was harder than or equal to the device, less than 0.1% was generated at the center of substrate, but large tensile strain of 2.5% occurred at the edge of substrate. The result shows the same trend as the result of fixed twisting simulation in Fig. 4.10 and 4.11.

However, as the Young's modulus of base decreased, the strain value of edge decreased, and compressive deformation occurred gradually at the center of substrate. In the case of the substrate on the softest base like skin, compressive strain at the center and the tensile deformation at the edge occurred with same value about 0.1%, and the value of equivalent strain was calculated as 0.1% in both the outer and center of substrate. The stress-free zone was found in the middle between the rotation axis and the edge. The overall strain increased as the base became harder, and the value of strain increased to 4.9% at the edge and 4.3% at the center on the hardest Kevlar base.

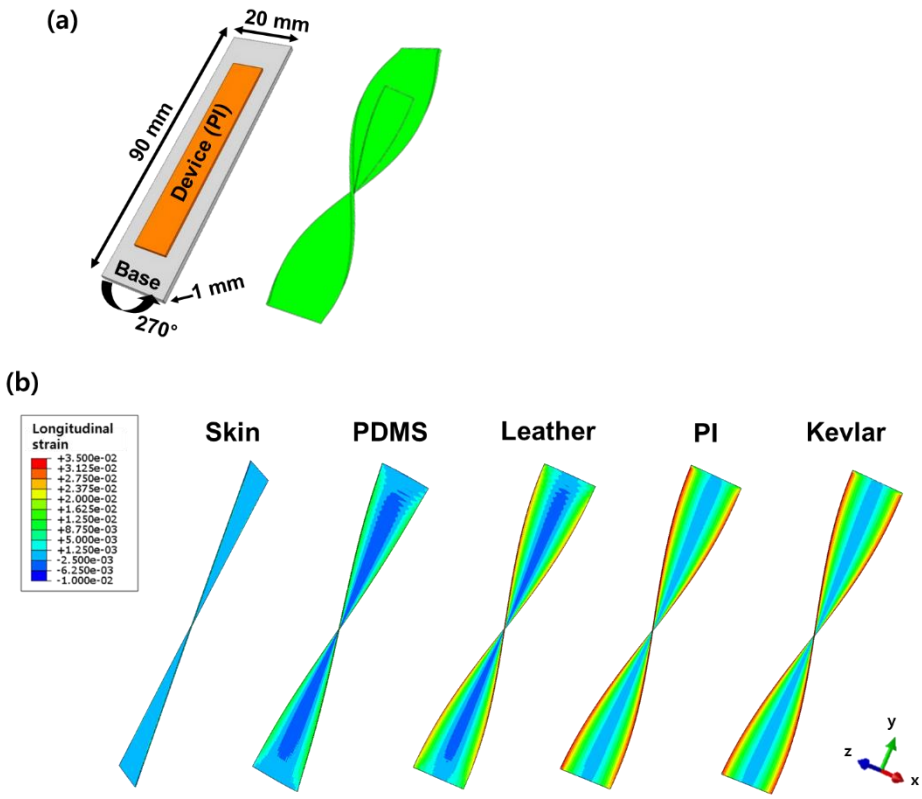

Figure 4.12 (a) Schematic of a model of flexible device on various base materials. (b) During twisting motion, longitudinal strain distributions of flexible device on different base materials

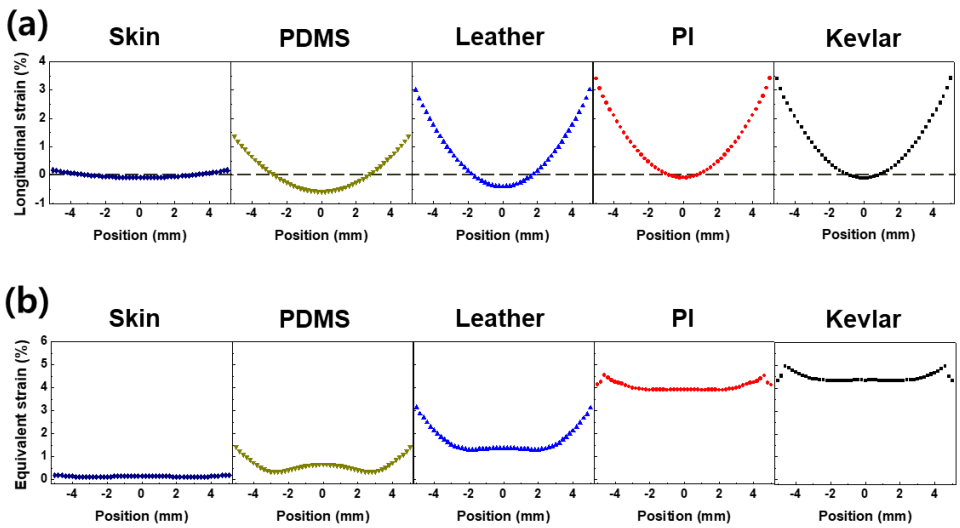

Figure 4.13 (a) Longitudinal strain and (b) equivalent strain of the flexible device attached to different base materials according to the position from twisting axis.

Fig. 4.14 (a) and (b) shows the twisting angle of substrate on base and a value of longitudinal strain where x is 0 mm as center and where x is 4.5 mm as edge depending on the Young's modulus ratio between the base and the device, respectively. In the case of the base having higher Young's modulus, the device on the base followed the deformation of the base, which was twisted with fixed boundary condition. Therefore, it showed higher strain at the edge and lower strain at the center as in the case of fixed twisting.

However, when the base was softer than the device, as the base became softer, the strain at the center increases, and the gap of the strain value between the center and the edge decreased. Even if the base material was deformed into a fixed twisting shape, if the device was harder than the base, the device deformed as free twisting in which both ends of the device moved freely in the longitudinal direction.

Stress of relatively rigid parts, such as PI substrate on skin, were offset by creating compressive behavior at the center due to changes in boundary conditions, and the strain in the longitudinal direction varied with the distance from the rotation axis. Therefore, the mechanical properties of the base where the device is placed affect stress-free zone and should be considered when designing the device arrangement. Defined stress-free zone provides a guide for placing the electrode to edge in case of softer base material and to center in case of harder base material.

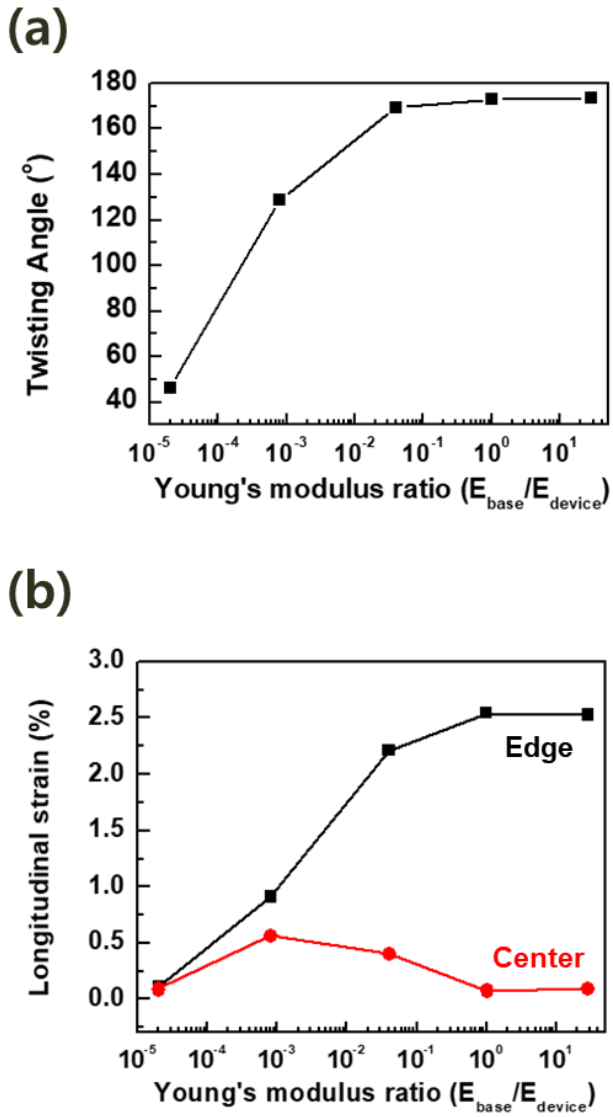

Figure 4.14 (a) Rotation angle and (b) longitudinal strain of the flexible device attached to different base materials according to the position from twisting axis of edge and center area of flexible device as a function of Young's modulus ratio.

4.5 Fixed/Free twisting condition in human body

Based on the results of experiments and simulation, the ITO pattern was used as indicator of strain to define the actual human body and to confirm the mechanical reliability by applying twisting motion. The ITO deposited sample attached on the protection coat with twisting motion in the shoulder and arms and sample twisted by hand and gripped tightly to keep the initial sample length as shown in Fig. 4.15 (a) and (b). Similar to the fixed twisting test, the ITO line patterns on the substrate edge were broken and the light emitting diode (LED) did not turn on when connected by the lines. On the other hand, the LED connected by the center patterns showed light turning on.

To test different twisting mode, the ITO deposited sample attached directly onto human skin and sample twisted loosely by hand as shown in Fig. 4.15 (c) and (d). In this case, the ITO patterns at the center of substrate were broken, but the patterns at the edge maintained conducting path and interconnecting and lighting LED well like the free twisting test. Therefore, even when twisting deformation occurs due to the same human motion, the twisting modes should be defined depending on the material properties of the attached surface and the boundary condition of the attached product. Considering these modes, a design that protects vulnerable elements based on the strain distribution is required for reliable future electronic devices.

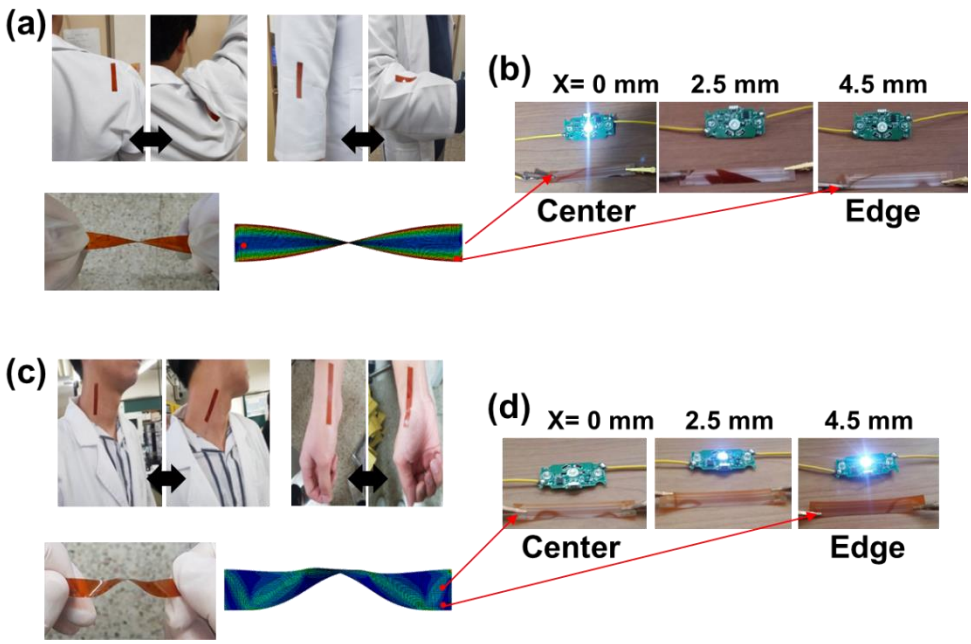

Figure 4.15 (a) ITO samples twisted tightly by attached onto protection coat and hand. (b) LED connected to ITO pattern after tight twisting motion. (c) ITO samples twisted loosely by attached directly onto human skin and hand. (d) LED connected to ITO pattern after loose twisting motion.

These FEM and experimental results on stress distribution can be usefully applied to anticipate the mechanical stress effect on the device property. Although all electronic elements cannot be placed in the stress-free zone, the fatigue lifetime of the electrode can be improved by considering the twisting mode. For example, the mobility of transistor near the through-Si-via (TSV), which connects the semiconductor devices vertically in the Si chip, is affected by thermal stress. The high stress region near the TSV is called the keep-away-zone, and during the chip design process, this area is avoided [84]. For flexible electronics, as higher mechanical stress will be directly applied on the electronics devices, the high stress region (keep-away-zone) and safe region (stress-free zone) need to be clearly defined. In the case of wearable electronics on a soft surface, the center region is keep-away-zone, so interconnects and elements should be placed as far from center as possible to place in stress-free zone.

4.6 Summary

In conclusion, the mechanical reliability of flexible ITO and Cu patterns in twisting deformation was investigated. The electrical resistances of the ITO and Cu patterns were monitored *in-situ* during fixed and free twisting, and the stress evolution was analyzed by FEM simulation. In fixed twisting, the patterns at the center exhibited low resistance change, and only few cracks were detected at the center area. Contrary, the patterns at the edge showed significant electrical resistance increase, because the tensile stress was evolved at the edge area and resulted in mechanical failure in the interconnect. On the other hand, in free twisting, the electrical resistance increased highly at the center area, but that in the edge area showed superior stability, because the stress at the edge area is relaxed by shortening and buckling. The stress-free zone for fixed twisting is the center, but for free twisting, it is the edge area. This tendency is also confirmed by applying the real twisting motion of the human body. This classification of twisting modes and stress-free zone can be the starting point of reliability study for complex deformation of future electronics.

CHAPTER 5

Conclusion and Future Work

5.1 Summary of results

With the development of electronic devices, the importance of interconnects, from the several nm scale to the visible macroscale, is increasing daily. As many elements are integrated in various forms, the complexity of the mechanical structure increases, and the margin for the corresponding deformation decreases. This thesis proposes a solution to the complex mechanical problem using the FEM with a material-based simplification.

In chapter 3, a study was conducted to analyze the stress of tungsten as a good gap filler and a barrierless interconnect metal for M1, which is a stress-dominant case. High deposition stress of tungsten was predicted by applying the surface traction. To

reduce the tungsten deposition stress, the shape of the nuclei can be controlled, which is an effective way to suppress the mechanical deformation caused by the formation of grain boundaries between free surfaces during the coalescence stage. Furthermore, film interactions, such as interfilm coalescence, were calculated in the case of the trench pattern. The defects in the depth and width of the periodic trench influenced mold bending in the early growth stage and the coalescence stage of films, respectively.

In chapter 4, the mechanical strain and fatigue of flexible electronics were analyzed under twisting deformation, which is a strain-dominant case. A stress-free zone transition was found to occur when the boundary conditions changed due to a soft surface rather than a rigid surface. Our study presented a new twisting mode, the free twisting mode, which showed the opposite stress-free zone to conventional twisting deformation, i.e., the fixed twisting mode. The free twisting mode was proven by the mechanical reliability of flexible ITO and copper patterns during twisting motion and the simulation results obtained by the FEM. Lastly, the stress-free zone was verified by conducting a real twisting test, such as the twisting motion of the human body.

In summary, most of the mechanical problems currently occurring in the field of interconnects are 'interconnected' problems of the stress from the nature of the material and the systematic deformation due to the accumulation of these stresses. Therefore, the two extremes of research, stress in metals and strain in flexible interconnects, can provide intuition of combined mechanical issues, and using the finite element method with appropriate simplification is useful for predicting

complex mechanical issues occurring in overall interconnection systems such as wiring and packaging.

5.2 Future work and suggested research

In the modeling of the barrierless metal examined above, that is, the tungsten case, many simplifications and assumptions were considered in the FEM simulation, such as the microstructural properties of materials. In the current fabrication process, atomic migration in refractory metals hardly occurs at the process temperature, but most of the energetic properties used in the analysis result from atomic properties such as the bonding energy. Therefore, it is necessary to analyze the microstructure of the thin film to increase the accuracy of the simulation. In addition, the interfilm coalescence occurring in the vertical structure acts as the main source of stress, which is greatly influenced by the mold dimensions and asymmetry. Therefore, the bending effect of structural factors in the trench mold structure must be investigated. Lastly, with the shrinkage of the dielectric thickness, the change in mechanical properties is dramatic in molds. Air gaps and porous materials for low-k dielectrics or polymeric dielectrics used in RDLs have been developed, which have a lower Young's modulus than Si molds. Therefore, since the mechanical failure of the mold due to the residual stress of the metal film increases, it is necessary to study the metal-dielectric interfaces that can lower the residual stress or reduce the stress effect by reducing the transfer of the metal stress to the mold.

References

[1] W. Arden *et al.*, More-than-Moore white paper. *ITRS* (2010).

[2] Ericsson mobility report. *Ericsson: Stockholm, Sweden* (2019).

[3] J. E. Mück, B. Ünal, H. Butt, A. K. Yetisen, Market and Patent Analyses of Wearables in Medicine. *Trends in Biotechnology*, 37, 563-566 (2019).

[4] Heterogeneous Integration Roadmap 2021 Edition. *IEEE EPS* (2021).

[5] The GSMA Guide to the Internet of Things. *GSMA* (2019).

[6] N. Soni, E. K. Sharma, N. Singh, A. Kapoor, Artificial Intelligence in Business: From Research and Innovation to Market Deployment. *Procedia Computer Science*, 167, 2200-2210, (2020)

[7] J. L. Hennessy, D. A. Patterson, *Computer architecture: a quantitative approach*. Elsevier (2017).

[8] M. Bohr, K. Mistry, Intel's revolutionary 22 nm transistor technology. *Intel* (2011).

[9] C. Auth *et al.*, A 10nm high performance and low-power CMOS technology featuring 3rd generation FinFET transistors, Self-Aligned Quad Patterning, contact over active gate and cobalt local interconnects. *2017 IEEE International Electron Devices Meeting (IEDM)*, 21-29 (2017).

[10] S. Narasimha *et al.*, A 7nm CMOS technology platform for mobile and high performance compute application. *2017 IEEE International Electron Devices Meeting (IEDM)*, 21-29 (2017).

[11] T. B. Hook, Power and technology scaling into the 5 nm node with stacked nanosheets. *Joule* 2, 1-4 (2018).

[12] L. Su, Delivering the future of high-performance computing. *2019 Semicon West* (2019).

[13] J. A. Rogers, T. Someya, Y. Huang, Materials and mechanics for stretchable electronics. *Science* 327, 1603-1607 (2010).

[14] D.-H. Kim *et al.*, Epidermal electronics. *Science* 333, 838-843 (2011).

[15] W. Bauer, M. Hämmerle, S. Schlund, C. Vocke, Transforming to a Hyper-connected Society and Economy – Towards an "Industry 4.0". *Procedia Manufacturing* 3, 417-424 (2015).

[16] More Moore - Logic Core Device Technology Roadmap. *International Roadmap for Devices and Systems (IRDS) 2021* (2021).

[17] B. Sell *et al.*, in *2022 IEEE Symposium on VLSI Technology and Circuits* (2022)

[18] A. Yu *et al.*, Fabrication of High Aspect Ratio TSV and Assembly With Fine-Pitch Low-Cost Solder Microbump for Si Interposer Technology With High-Density Interconnects. *IEEE Transactions on Components, Packaging and Manufacturing Technology* 1, 1336-1344 (2011).

[19] S. Zhang, X. Xu, T. Lin, P. He, Recent advances in nano-materials for packaging of electronic devices. *Journal of Materials Science: Materials in Electronics* 30, 13855-13868 (2019).

[20] T. Gupta, *Copper interconnect technology.* Springer Science & Business Media, (2010).

[21] A. Agrawal, A. Jaiswal, C. Lee, K. Roy, X-SRAM: Enabling In-Memory Boolean Computations in CMOS Static Random Access Memories. *IEEE Transactions on Circuits and Systems I: Regular Papers* 65, 4219-4232 (2018).

[22] S. Cheramy *et al.*, in *2021 International Symposium on VLSI Technology, Systems and Applications (VLSI-TSA)*. IEEE, (2021).

[23] W.-W. Shen, K.-N. Chen, Three-Dimensional Integrated Circuit (3D IC) Key Technology: Through-Silicon Via (TSV). *Nanoscale Research Letters* 12, 56 (2017).

[24] V. S. Rao *et al.*, Development of High Density Fan Out Wafer Level Package (HD FOWLP) with Multi-layer Fine Pitch RDL for Mobile Applications. *2016 IEEE 66th Electronic Components and Technology Conference (ECTC)*, 1522-1529 (2016).

[25] J.-C. Lee *et al.*, Operation Range-Optimized Silver Nanowire Through Junction Treatment. *Electronic Materials Letters* 16, 491-497 (2020).

[26] Y.-Y. Lee *et al.*, A Strain-Insensitive Stretchable Electronic Conductor: PEDOT:PSS/Acrylamide Organogels. *Advanced Materials* 28, 1636-1643 (2016).

[27] J. A. Fan *et al.*, Fractal design concepts for stretchable electronics. *Nature Communications* 5, 3266 (2014).

[28] A. Lamoureux, K. Lee, M. Shlian, S. R. Forrest, M. Shtein, Dynamic kirigami structures for integrated solar tracking. *Nature Communications* 6, 8092 (2015).

[29] A. Heryanto *et al.*, The effect of stress migration on electromigration in dual damascene copper interconnects. *Journal of Applied Physics* 109, 013716 (2011).

[30] J. Koike, M. Wada, M. Sanada, K. Maruyama, Effects of crystallographic texture on stress-migration resistance in copper thin films. *Applied Physics Letters* 81, 1017-1019 (2002).

[31] A. H. Abdelnaby *et al.*, Numerical simulation of silicon wafer warpage due to thin film residual stresses. *2013 IEEE Workshop on Microelectronics and Electron Devices (WMED)*, 9-12 (2013).

[32] A. Nathan *et al.*, Flexible Electronics: The Next Ubiquitous Platform. *Proceedings of the IEEE* 100, 1486-1517 (2012).

[33] J. N. Reddy, *Introduction to the finite element method*. McGraw-Hill Education, (2019).

[34] J. A. Thornton, High rate thick film growth. *Annual review of materials science* 7, 239-260 (1977).

[35] H. O. Pierson, *Handbook of chemical vapor deposition: principles, technology and applications*. William Andrew, (1999).

[36] M. Leskelä, M. Ritala, Atomic layer deposition (ALD): from precursors to thin film structures. *Thin solid films* 409, 138-146 (2002).

[37] C. Gabrielli, P. Moçotéguy, H. Perrot, D. Nieto-Sanz, A. Zdunek, A model for copper deposition in the damascene process. *Electrochimica Acta* 51, 1462-1472 (2006).

[38] K. Oura, V. Lifshits, A. Saranin, A. Zotov, M. Katayama, *Surface science: an introduction*. Springer Science & Business Media, (2013).

[39] S. C. Seel, MIT Thesis (2002).

[40] A. Saedi, M. J. Rost, Thermodynamics of deposition flux-dependent intrinsic film stress. *Nature Communications* 7, 10733 (2016).

[41] R. C. Cammarata, Surface and interface stress effects in thin films. *Progress in surface science* 46, 1-38 (1994).

[42] W. D. Nix, B. M. Clemens, Crystallite coalescence: A mechanism for intrinsic tensile stresses in thin films. *Journal of Materials Research* 14, 3467-3473 (1999).

[43] S. C. Seel, C. V. Thompson, S. J. Hearne, J. A. Floro, Tensile stress evolution during deposition of Volmer–Weber thin films. *Journal of Applied Physics* 88, 7079-7088 (2000).

[44] R. Cammarata, T. Trimble, D. J. Srolovitz, Surface stress model for intrinsic stresses in thin films. *Journal of Materials Research* 15, 2468-2474 (2000).

[45] C. Cheng-Hsin, G. Huajian, Stress singularities along a cycloid rough surface. *International Journal of Solids and Structures* 30, 2983-3012 (1993).

[46] W. Kim *et al.*, Controlled multiple neutral planes by low elastic modulus adhesive for flexible organic photovoltaics. *Nanotechnology* 28, 194002 (2017).

[47] J.-K. Yang, Y.-J. Lee, S.-M. Yi, B.-J. Kim, Y.-C. Joo, Effect of twisting fatigue on the electrical reliability of a metal interconnect on a flexible substrate. *Journal of Materials Research* 33, 138-148 (2018).

[48] J.-S. Lee, S. Kim, D. Han, M.-G. Lee, Y.-C. Joo, Stress Analysis of Tungsten Deposition in a 3D Trench Mold With Regard to Initial Nuclei Shape. *IEEE Access* 10, 100675-100681 (2022)

[49] H. Kikuchi *et al.*, Tungsten through-silicon via technology for three-dimensional LSIs. *Japanese Journal of Applied Physics* 47, 2801 (2008).

[50] J. Bakke *et al.*, in *2016 IEEE International Interconnect Technology Conference / Advanced Metallization Conference (IITC/AMC)*. (2016).

[51] K. Croes *et al.*, in *2018 IEEE International Electron Devices Meeting (IEDM)* (2018).

[52] H. Mehrer, *Diffusion in solids: fundamentals, methods, materials, diffusion-controlled processes*. Springer Science & Business Media, (2007).

[53] D. Triyoso *et al.*, in *2010 IEEE International Conference on Integrated Circuit Design and Technology* (2010).

[54] M.-G. Sung, Y. S. Kim, S.-K. Park, in *18th IEEE International Symposium on the Physical and Failure Analysis of Integrated Circuits (IPFA)* (2011).

[55] K. Kim, in *IEEE International Electron Devices Meeting, 2005. IEDM Technical Digest.* (2005).

[56] W. D. Nix, Mechanical properties of thin films. *Metallurgical transactions A* 20, 2217-2245 (1989).

[57] S. C. Seel, C. V. Thompson, Tensile stress generation during island coalescence for variable island-substrate contact angle. *Journal of applied physics* 93, 9038-9042 (2003).

[58] R. Abermann, R. Koch, The internal stress in thin silver, copper and gold films. *Thin Solid Films* 129, 71-78 (1985).

[59] A. L. Shull, F. Spaepen, Measurements of stress during vapor deposition of copper and silver thin films and multilayers. *Journal of Applied Physics* 80, 6243-6256 (1996).

[60] G. Leusink, T. Oosterlaken, G. Janssen, S. Radelaar, The evolution of growth stresses in chemical vapor deposited tungsten films studied by in situ wafer curvature measurements. *Journal of applied physics* 74, 3899-3910 (1993).

[61] M. Bauccio, *ASM metals reference book*. ASM international (1993).

[62] L. Gan, B. Ben-Nissan, A. Ben-David, Modelling and finite element analysis of ultra-microhardness indentation of thin films. *Thin Solid Films* 290, 362-366 (1996).

[63] E. Hodkin, M. Nicholas, D. Poole, The surface energies of solid molybdenum, niobium, tantalum and tungsten. *Journal of the Less Common Metals* 20, 93-103 (1970).

[64] F. Aqra, A. Ayyad, Surface energies of metals in both liquid and solid states. *Applied Surface Science* 257, 6372-6379 (2011).

[65] H. Zheng *et al.*, Grain boundary properties of elemental metals. *Acta Materialia* 186, 40-49 (2020).

[66] R. B. Ross, *Metallic materials specification handbook*. Springer Science & Business Media (2013).

[67] R. Abermann, R. Kramer, J. Mäser, Structure and internal stress in ultra-thin silver films deposited on MgF2 and SiO substrates. *Thin Solid Films* 52, 215-229 (1978).

[68] Y.-W. Kwon, J.-S. Lee, Y.-C. Joo, B.-J. Kim, In Twisting Motion, Stress-Free Zone of Wearable Electronics. *Advanced Electronic Materials* 6, 1901239 (2020).

[69] B.-J. Kim, J.-H. Lee, Y.-C. Joo, Effect of cyclic outer and inner bending on the fatigue behavior of a multi-layer metal film on a polymer substrate. *Japanese Journal of Applied Physics* 55, 06JF01 (2016).

[70] T.-W. Kim, J.-S. Lee, Y.-C. Kim, Y.-C. Joo, B.-J. Kim, Bending strain and bending fatigue lifetime of flexible metal electrodes on polymer substrates. *Materials* 12, 2490 (2019).

[71] T.-W. Kim *et al.*, Electrical Reliability of Flexible Silicon Package Integrated on Polymer Substrate During Repeated Bending Deformations. *Journal of Electronic Packaging* 144, 041017 (2022).

[72] X. Zhu, B. Zhang, J. Gao, G. Zhang, Evaluation of the crack-initiation strain of a Cu–Ni multilayer on a flexible substrate. *Scripta Materialia* 60, 178-181 (2009).

[73] Z. Suo, E. Ma, H. Gleskova, S. Wagner, Mechanics of rollable and foldable film-on-foil electronics. *Applied physics letters* 74, 1177-1179 (1999).

[74] S. I. Park *et al.*, Theoretical and experimental studies of bending of inorganic electronic materials on plastic substrates. *Advanced Functional Materials* 18, 2673-2684 (2008).

[75] Y.-L. Loo *et al.*, Soft, conformable electrical contacts for organic semiconductors: High-resolution plastic circuits by lamination. *Proceedings of the National Academy of Sciences* 99, 10252-10256 (2002).

[76] S. Diridollou *et al.*, In vivo model of the mechanical properties of the human skin under suction. *Skin Research and technology* 6, 214-221 (2000).

[77] I. Johnston, D. McCluskey, C. Tan, M. Tracey, Mechanical characterization of bulk Sylgard 184 for microfluidics and microengineering. *Journal of Micromechanics and Microengineering* 24, 035017 (2014).

[78] U. Wegst, M. Ashby, The mechanical efficiency of natural materials. *Philosophical Magazine* 84, 2167-2186 (2004).

[79] DuPont, Technical Guide for Kevlar Aramid Fiber.

[80] IEC 62899-202-5: Printed electronics - Part 202-5: Materials - Conductive ink - Mechanical bending test of a printed conductive layer on a substrate.

[81] IEC 62715-6-1: Flexible display devices - Part 6-1: Mechanical stress test methods.

[82] S.-Y. Lee *et al.*, Selective crack suppression during deformation in metal films on polymer substrates using electron beam irradiation. *Nature Communications* 10, 4454 (2019).

[83] S.-M. Yi, I.-S. Choi, B.-J. Kim, Y.-C. Joo, Reliability Issues and Solutions in Flexible Electronics Under Mechanical Fatigue. *Electronic Materials Letters* 14, 387-404 (2018).

[84] K. Athikulwongse, A. Chakraborty, J.-S. Yang, D. Z. Pan, S. K. Lim, in *2010 IEEE/ACM International Conference on Computer-Aided Design (ICCAD)* (2010).

요약(국문초록)

4 차 산업 혁명으로 인해 다양한 디지털 기기와 정보를 처리하는 다양한 소자들의 중요도가 커지고 발전함에 따라, 전자 소자를 연결하는 배선 물질에 대한 혁신적 성능의 개선과 기능의 다각화가 떠오르고 있다. 특히 최신 반도체의 집적도가 크게 증가하고 있으며, 이와 더불어 기계적 변형이 가능한 형태의 패키징 등의 기능의 다변화가 크게 일어나고 있다.

그러나 최근 배선의 발전과 더불어, 박막으로 이루어진 배선 재료에서 발생하는 기계적 응력과 변형의 중요성이 떠오르고 있다. 대표적인 금속 박막의 경우 증착하는 과정에서 발생하는 높은 잔류응력, 물성 차이가 존재하는 이종 재료 간의 계면 증가, 및 배선 시스템의 마진 감소 등으로 인해 다양한 기계적 문제들이 발생한다.

따라서 본 연구는 유한요소해석을 이용해 박막형 배선에서 발생하는 응력과 변형 문제를 예측하고 해결하였다. 응력과 변형이 복합적으로 발생하는 박막 배선의 기계적 문제를 해결하기 위해, 박막 성장 모델을 기반으로 한 텅스텐 박막의 응력 예측 모델과, 탄성 변형을 기반으로 한 유연 배선의 비틀림 변형 하 안전영역의 위치 연구를 진행했다.

텅스텐 박막의 응력 예측 모델의 경우, 금속 박막의 볼머-웨버 성장 모델을 기반으로 섬 형태로 형성된 금속 핵이 서로 병합하며 발생하는 인장 응력을 계산하였다. 높은 확산도로 인해 확산 방지막이 필요한 구리 배선을 대체하기 위한 금속으로, 낮은 이동도를 가지는 난융 금속을 배선으로 사용하고자 하는 연구가 진행되고 있으나 높은 잔류응력으로 인한 변형 문제를 발생하고 있다. 이러한 응력을 완화하기 위해 계면 처리를 통한 금속 핵의 수평 확장성을 개선한 형태를 제안하였으며, 이를 통한 응력의 완화를 계산했다.

나아가, 배선 형성을 위한 트렌치 형태의 유전체 내부에 금속을 증착하는 과정에서 응력으로 인해 발생하는 유전체 몰드의 변형 역시 예측하였다. 특히 유전체 몰드의 경우, 공정과정에서 다양한 비대칭성이 존재하게 되며, 깊이 비대칭성은 몰드의 휘는 현상에 영향을 미치고, 너비 비대칭성의 경우, 양 벽면의 금속 박막이 서로 붙은 현상에 영향을 미치는 것을 확인했다.

이와 반대로 유연 배선의 비틀림 변형의 경우, 외부의 기계적 변형으로 인해 발생하는 응력과 변형의 분포를 예측한 연구로, 웨어러블과 같은 기계적 변형이 발생하는 기판에 위치한 배선의 신뢰성을 변형 분포를 고려한 배치로 개선하였다.

기존에 많이 연구된 굽힘 변형의 경우, 내부에 중립축과 같은 응력이 존재하지 않는 안전영역이 존재하며 변형에 취약한 재료를 해당 위치에 배치함으로 높은 신뢰성을 유지할 수 있다. 그러나 이러한 굽힘 변형과 달리 인체의 회전 변형과 같은 비틀림 변형에 대해서는 이러한 안전영역에 대한 연구가 거의 진행되지 않았다.

따라서 전자 소자를 집적할 수 있는 판상형태의 비틀림 변형에 대한 연구를 통해 비틀림의 고정여부에 따라 크게 고정 비틀림, 자유 비틀림 2 가지 모드로 변형 모드가 변함을 확인하였으며, 각각의 모드에서 응력이 발생하지 않는 안전영역이 반대로 나타나는 것을 확인했다. 고정 비틀림의 경우, 기존 비틀림 변형과 같이 양 끝단이 단단하게 고정되어 있는 경우로, 회전축에서 멀어질수록 더 큰 변형이 발생하는 일반적인 비틀림 이론을 따라, 회전축에 안전영역이 위치하게 된다. 그러나 자유 비틀림의 경우, 양 끝단이 피부 등의 부드러운 재료들에 고정되어 있어, 좌굴 등의 두께 방향의 변형들이 발생하여 외곽의 변형이 제한되기 때문에, 오히려 회전축에서 멀어질수록 응력이 완화되는 반대되는 현상을 보였다. 이를 고려하여 배선을 배치할 경우 신뢰성이 크게 개선되는 것을 확인했다.

이와 같이 배선의 첨단에서는 박막의 응력이 패턴의 뒤틀림을 유발하고 있으며, 실제 사용하는 제품들의 영역에서는 이러한 뒤틀림이 누적되어 큰 변형으로 관찰된다. 따라서 이러한 응력과 변형이 모두 배선 시스템에 복합적으로 작용하고 있으므로, 박막 응력과 기계적 변형, 양 극단의 기계적 현상 연구를 통해, 복합적으로 발생하는 기계적 문제에 해석적 접근을 통한 가이드라인을 제시하고자 하였다.

표제어: 배선, 패키징, 응력, 변형, 유한요소해석, 유연 소자

학번: 2017-27024

CURRICULUM VITAE

Jong-Sung Lee

EDUCATION

2017 ~ **Seoul National University, South Korea** Seoul, Korea

Integrated course of M.S. and Ph.D.

Department of Materials Science and Engineering

Stress and Strain Analysis of Thin Film Interconnects in Future Electronic Devices Using Finite Element Method

Advisor: Young-Chang Joo, Professor

In-Suk Choi, Associate Professor

Co-Advisor: Myoung-Gyu Lee, Professor

2010 ~ 2017 **Seoul National University, South Korea** Seoul, Korea

B.S., Department of Materials Science and Engineering

RESEARCH EXPERIENCES

Numerical analysis of metal film stress by finite element method

- Stress analysis of refractory metal
- Simulation model based on growth mechanism
- Film interaction calculation in 3D structure

Mechanical analysis of interconnects on flexible substrate for wearable

- Thickness effect on bending deformation
- Simulation model for free twisting mode on soft surface
- Soft electronics for wearable and sensor

AWARDS AND HONORS

2020 ~ **Sponsorship Program**, Samsung Electronics Co., Ltd.

PROFESSIONAL ACTIVITIES

2012 ~ 2014 **Mandatory Military Service**

PUBLICATIONS

- **J.-S. Lee**, S. Kim, D. Han, M.-G. Lee*, and Y.-C. Joo*, Stress Analysis of Tungsten Deposition in a 3D Trench Mold With Regard to Initial Nuclei Shape. *IEEE Access*, **10**, 100675-100681, (2022)
- Y.-W. Kwon†, **J.-S. Lee†**, Y.-C. Joo*, and B.-J. Kim*, In Twisting Motion, Stress-Free Zone of Wearable Electronics. *Advanced Electronic Materials*, **6**(3), 1901239, (2020)
- T.-W. Kim†, **J.-S. Lee†**, Y.-C. Kim, Y.-C. Joo*, and B.-J. Kim*, Bending strain and bending fatigue lifetime of flexible metal electrodes on polymer substrates. *Materials*, **12**(15), 2490, (2019)
- T.-W. Kim, J.-M. Kim, H.-J. Yun, **J.-S. Lee**, J.-H. Lee, J.-Y. Song, Y.-C. Joo, W.-J. Lee*, and B.-J. Kim*, Electrical Reliability of Flexible Silicon Package Integrated on Polymer Substrate During Repeated Bending Deformations. *Journal of Electronic Packaging*, **144**(4), 041017, (2022)
- H. Yeon, H. Lee, Y. Kim, D. Lee, Y.-J. Lee, **J.-S. Lee**, J. Shin, C. Choi, J.-H. Kang, J. M. Suh., H. Kim, H. S. Kum, J. Lee, D. Kim, K. Ko, B. S. Ma, P. Lin, S. Han, S. Kim, S.-H. Bae, T.-S. Kim, M.-C. Park, Y.-C. Joo, E. Kim, J. Han*, and J. Kim*, Long-term reliable physical health monitoring by sweat pore–

inspired perforated electronic skins. *Science Advances*, **7**(27), eabg8459, (2021)

- J.-Y. Bae, E.-J. Gwak, G.-S. Hwang, H. W. Hwang, D.-J. Lee, **J.-S. Lee**, Y.-C. Joo, J.-Y. Sun, S. H. Jun*, M.-R. Ok*, J.-Y. Kim*, and S.-K. Kang*, Biodegradable metallic glass for stretchable transient electronics. *Advanced Science*, **8**(10), 2004029, (2021)
- S.-K. Lee, Y. W. Cho, **J.-S. Lee**, Y.-R. Jung, S.-H. Oh, J.-Y. Sun*, S. Kim*, and Y.-C. Joo*, Nanofiber Channel Organic Electrochemical Transistors for Low-Power Neuromorphic Computing and Wide-Bandwidth Sensing Platforms. *Advanced Science*, **8**(10), 2001544, (2021)
- J.-C. Lee, **J.-S. Lee**, P. Won, J. J. Park, S. H. Choi, S. H. Ko, B.-J. Kim, S.-Y. Lee*, and Y.-C. Joo*, Operation range-optimized silver nanowire through junction treatment. *Electronic Materials Letters*, **16**(5), 491-497, (2020)
- D.-J. Lee, **J.-S. Lee**, T.-W. Kim, S.-Y. Lee, Y.-B. Park, Y.-C. Joo, and B.-J. Kim*, Effect of the thermal annealing on the stretchability and fatigue failure of the copper film on the polymer substrate. *Journal of Electronic Materials*, **48**(7), 4582-4588, (2019)

PRESENTATIONS IN CONFERENCES

- "Deposition condition of low stress tungsten in the trench mold using finite element analysis", **J.-S. Lee**, S. Kim, D. Han, M.-G. Lee*, and Y.-C. Joo*, The 29th Korean Conference on Semiconductors (KCS 2022), Gangwon-do, Korea (Jan. 2022) (Poster)

- "Effect of cyclic Frequency on Bending Fatigue in Copper Film on Flexible Substrate" **J.-S. Lee**, Y.-J. Lee, B.-J. Kim*, and Y.-C. Joo*, the 19th International Symposium on Microelectronics and Packaging (ISMP 2021), Busan, Korea (Nov. 2021) (Oral)
- "Interconnects Design to Improve Bending Reliability of Flexible Device with Packaging Chip", **J.-S. Lee**, J. Seol, Y.-J. Lee, Y.-C. Joo*, and B.-J. Kim*, The 28th Korean Conference on Semiconductors (KCS 2021), Online, (Jan. 2021) (Poster)
- "Neutral axis of wearable twisting motion for reliable flexible electronics", **J.-S. Lee**, Y.-W. Kwon, B.-J. Kim*, and Y.-C. Joo*, The Korean Microelectronic and Packaging Society 2020 (KMEPS 2020), Online (Nov. 2020) (Poster)
- "Strain rate dependence on mechanical reliability of hybrid flexible electronics system", **J.-S. Lee**, Y.-J. Lee, B.-J. Kim, I.-S. Choi, and Y.-C. Joo*, NANO KOREA 2019, Gyeonggi-do, Korea (Jul. 2019) (Poster)
- "Strain rate dependence on mechanical reliability of thin Cu film on flexible substrate", **J.-S. Lee**, Y.-J. Lee, B.-J. Kim, and Y.-C. Joo*, NANO KOREA 2018, Gyeonggi-do, Korea (Jul. 2018) (Oral)
- "Geometric Design for a Highly Sensitive and Mechanically Robust Capacitivte Type Strain Sensor with Multimodal Signal Decoupling", **J.-S. Lee**, Y.-J. Lee, S.-M. Lim, I.-S. Choi, and Y.-C. Joo*, 2018 MRS Spring Meeting & Exhibit, Phoenix, USA (Apr. 2018) (Poster)

PATENT

- "Flexible device", Y.-C. Joo*, J.-C. Lee, **J.-S. Lee**, Korea Patent (10-2020-0083410)
- "Stretchable wiring board device, method of manufacturing the stretchable wiring board device, Electronic device including the stretchable wiring board device", I.-S. Choi*, M.-G. Lee*, **J.-S. Lee**, J. Kim, Korea Patent (10-2018-0172907)

R & D PROJECTS

- "PIM 2.5D Large-Scale Super-Performance Interposer and 3D Hybrid Bonding Platform for PIM Semiconductor integrating Processors and High-Bandwidth Memories", funded by the Ministry of Science and ICT, 2022. 9. ~
- "Center for SoFT meta-Human", funded by the National Research Foundation of Korea and the Ministry of Science and ICT, 2017. 3. ~ 2022. 8.
- "Stress analysis of 10nm-scale metal growth and mold bending", funded by Samsung Electronics Co., Ltd., 2020. 4. ~ 2021. 3.
- "Development of highly reliable flexible transparent electrodes by using oxidation-resistant metal/carbon hybrid nanofibers", funded by the Ministry of Trade, Industry and Energy, 2019. 1. ~ 2020. 5.
- "Research on mechanical reliability of interconnects and electrode materials for flexible displays", funded by Samsung Display Co., Ltd., 2019. 3. ~ 2020. 2.
- "Development of Interconnection System and Process for Flexible Three-Dimensional Heterogeneous Devices", funded by the Ministry of Trade, Industry and Energy, 2017. 3. ~ 2019. 12.

- “Development and standardization of reliability evaluation system for flexible and printed electronic devices under complex mechanical deformation”, funded by the Ministry of Trade, Industry and Energy, 2017. 3. ~ 2018. 5.